

The IceCube Neutrino Observatory

Contributions to ICRC 2017 Part VI: IceCube-Gen2, the Next Generation Neutrino Observatory

Contents

| | |
|---|-----------|
| 1 IceCube-Gen2: the next-generation neutrino observatory for the South Pole PoS (ICRC2017) 991 | 6 |
| 2 IceAct: Imaging Air Cherenkov Telescopes with SiPMs at the South Pole for IceCube-Gen2 — PoS (ICRC2017) 1055 | 14 |
| 3 Overview and performance of the D-Egg optical sensor for IceCube-Gen2 PoS (ICRC2017) 1051 | 22 |
| 4 Muon track reconstruction and veto performance with D-Egg sensor for IceCube-Gen2 — PoS (ICRC2017) 1038 | 30 |
| 5 In-ice self-veto techniques for IceCube-Gen2 — PoS (ICRC2017) 945 | 38 |
| 6 A camera system for IceCube-Gen2 — PoS (ICRC2017) 1040 | 46 |
| 7 The mDOM – A multi-PMT Digital Optical Module for the IceCube-Gen2 neutrino telescope — PoS (ICRC2017) 1047 | 54 |
| 8 The IceTop Scintillator Upgrade — PoS (ICRC2017) 401 | 62 |
| 9 Overview and Performance of the Wavelength-shifting Optical Module (WOM) PoS (ICRC2017) 1052 | 69 |
| 10 The Precision Optical CALibration Module for IceCube-Gen2: First Prototype — PoS (ICRC2017) 934 | 77 |

35th International Cosmic Ray Conference — ICRC2017
10–20 July, 2017
Bexco, Busan, Korea

IceCube-Gen2 Collaboration Member List

M. G. Aartsen², M. Ackermann⁵⁹, J. Adams¹⁶, J. A. Aguilar¹², M. Ahlers²⁰, M. Ahrens⁵⁰, I. Al Samarai²⁵, D. Altmann²⁴, K. Andeen³⁶, T. Anderson⁵⁶, I. Ansseau¹², G. Anton²⁴, C. Argüelles¹⁴, T. C. Arlen⁵⁶, J. Auffenberg¹, S. Axani¹⁴, H. Bagherpour¹⁶, X. Bai⁴⁷, A. Balagopal V.²⁸, J. P. Barron²³, I. Bartos⁴³, S. W. Barwick²⁷, V. Baum³⁴, R. Bay⁸, J. J. Beatty^{18,19}, J. Becker Tjus¹¹, K.-H. Becker⁵⁸, S. BenZvi⁴⁹, D. Berley¹⁷, E. Bernardini⁵⁹, D. Z. Besson²⁹, G. Binder^{9,8}, D. Bindig⁵⁸, E. Blaufuss¹⁷, S. Blot⁵⁹, C. Boehm⁵⁰, M. Bohmer³⁸, M. Börner²¹, F. Bos¹¹, D. Bose⁵², S. Böser³⁴, O. Botner⁵⁷, J. Bourbeau³³, F. Bradascio⁵⁹, J. Braun³³, L. Brayeur¹³, M. Brenzke¹, H.-P. Bretz⁵⁹, S. Bron²⁵, J. Brostean-Kaiser⁵⁹, A. Burgman⁵⁷, T. Carver²⁵, J. Casey³³, M. Casier¹³, E. Cheung¹⁷, D. Chirkin³³, A. Christov²⁵, K. Clark³⁰, L. Classen⁴⁰, S. Coenders³⁸, G. H. Collin¹⁴, J. M. Conrad¹⁴, D. F. Cowen^{56,55}, R. Cross⁴⁹, M. Day³³, J. P. A. M. de André²², C. De Clercq¹³, J. J. DeLaunay⁵⁶, H. Dembinski⁴¹, S. De Ridder²⁶, P. Desiati³³, K. D. de Vries¹³, G. de Wasseige¹³, M. de With¹⁰, T. DeYoung²², J. C. Díaz-Vélez³³, V. di Lorenzo³⁴, H. Dujmovic⁵², J. P. Dumm⁵⁰, M. Dunkman⁵⁶, M. A. DuVernois³³, B. Eberhardt³⁴, T. Ehrhardt³⁴, B. Eichmann¹¹, P. Eller⁵⁶, R. Engel²⁸, J. J. Evans³⁵, P. A. Evenson⁴¹, S. Fahey³³, A. R. Fazely⁷, J. Felde¹⁷, K. Filimonov⁸, C. Finley⁵⁰, S. Flis⁵⁰, A. Franckowiak⁵⁹, E. Friedman¹⁷, T. Fuchs²¹, T. K. Gaisser⁴¹, J. Gallagher³², A. Gartner³⁸, L. Gerhardt⁹, R. Gernhaeuser³⁸, K. Ghorbani³³, W. Giang²³, T. Glauch¹, T. Glüsenskamp²⁴, A. Goldschmidt⁹, J. G. Gonzalez⁴¹, D. Grant²³, Z. Griffith³³, C. Haack¹, A. Hallgren⁵⁷, F. Halzen³³, K. Hanson³³, J. Haugen³³, A. Haungs²⁸, D. Hebecker¹⁰, D. Heereman¹², K. Helbing⁵⁸, R. Hellauer¹⁷, F. Henningsen³⁸, S. Hickford⁵⁸, J. Hignight²², G. C. Hill², K. D. Hoffman¹⁷, B. Hoffmann²⁸, R. Hoffmann⁵⁸, B. Hokanson-Fasig³³, K. Holzappel³⁸, K. Hoshina^{33,53}, F. Huang⁵⁶, M. Huber³⁸, T. Huber²⁸, T. Huege²⁸, K. Hultqvist⁵⁰, M. Hünnefeld²¹, S. In⁵², A. Ishihara¹⁵, E. Jacobi⁵⁹, G. S. Japaridze⁵, M. Jeong⁵², K. Jero³³, B. J. P. Jones⁴, P. Kalaczynski¹, O. Kalekin²⁴, W. Kang⁵², D. Kang²⁸, A. Kappes⁴⁰, T. Karg⁵⁹, A. Karle³³, T. Katori³¹, U. Katz²⁴, M. Kauer³³, A. Keivani⁵⁶, J. L. Kelley³³, A. Kheirandish³³, J. Kim⁵², M. Kim¹⁵, T. Kintscher⁵⁹, J. Kiryluk⁵¹, T. Kittler²⁴, S. R. Klein^{9,8}, G. Kohnen³⁷, R. Koirala⁴¹, H. Kolanoski¹⁰, L. Köpke³⁴, C. Kopper²³, S. Kopper⁵⁴, J. P. Koschinsky¹, D. J. Koskinen²⁰, M. Kowalski^{10,59}, C. B. Krauss²³, K. Krings³⁸, M. Kroll¹¹, G. Krückl³⁴, J. Kunnen¹³, S. Kunwar⁵⁹, N. Kurahashi⁴⁶, T. Kuwabara¹⁵, A. Kyriacou², M. Labare²⁶, J. L. Lanfranchi⁵⁶, M. J. Larson²⁰, F. Lauber⁵⁸, D. Lennarz²², M. Lesiak-Bzdak⁵¹, A. Leszczyńska²⁸, M. Leuermann¹, Q. R. Liu³³, J. LoSecco⁴⁴, L. Lu¹⁵, J. Lünemann¹³, W. Luszczak³³, J. Madsen⁴⁸, G. Maggi¹³, K. B. M. Mahn²², S. Mancina³³, S. Mandalia³¹, S. Marka⁴³, Z. Marka⁴³, R. Maruyama⁴², K. Mase¹⁵, R. Maunu¹⁷, F. McNally³³, K. Meagher¹², M. Medici²⁰, M. Meier²¹, T. Menne²¹, G. Merino³³, T. Meures¹², S. Miarecki^{9,8}, J. Micallef²², G. Momenté³⁴, T. Montaruli²⁵, R. W. Moore²³, M. Moulai¹⁴, R. Nahnauer⁵⁹, P. Nakarmi⁵⁴, U. Naumann⁵⁸, G. Neer²², H. Niederhausen⁵¹, S. C. Nowicki²³, D. R. Nygren⁹, A. Obertacke Pollmann⁵⁸, M. Oehler²⁸, A. Olivas¹⁷, A. O’Murchadha¹², A. Palazzo³⁹, T. Palczewski^{9,8}, H. Pandya⁴¹, D. V. Pankova⁵⁶, L. Papp³⁸, P. Peiffer³⁴, J. A. Pepper⁵⁴, C. Pérez de los Heros⁵⁷, T. C. Petersen²⁰, D. Pieloth²¹, E. Pinat¹², J. L. Pinfold²³, M. Plum³⁶, P. B. Price⁸, G. T. Przybylski⁹, C. Raab¹², L. Rädel¹, M. Rameez²⁰, K. Rawlins³, I. C. Rea³⁸,

R. Reimann¹, B. Relethford⁴⁶, M. Relich¹⁵, M. Renschler²⁸, E. Resconi³⁸, W. Rhode²¹,
M. Richman⁴⁶, M. Riegel²⁸, S. Robertson², M. Rongen¹, C. Rott⁵², T. Ruhe²¹, D. Ryckbosch²⁶,
D. Rysewyk²², T. Sälzer¹, S. E. Sanchez Herrera²³, A. Sandrock²¹, J. Sandroos³⁴, P. Sandstrom³³,
S. Sarkar^{20,45}, S. Sarkar²³, K. Satalecka⁵⁹, H. Schieler²⁸, P. Schlunder²¹, T. Schmidt¹⁷,
A. Schneider³³, S. Schoenen¹, S. Schöneberg¹¹, F. G. Schröder²⁸, L. Schumacher¹, D. Seckel⁴¹,
S. Seunarine⁴⁸, M. H. Shaevitz⁴³, J. Soedingrekso²¹, D. Soldin⁵⁸, S. Söldner-Rembold³⁵,
M. Song¹⁷, G. M. Spiczak⁴⁸, C. Spiering⁵⁹, J. Stachurska⁵⁹, M. Stamatikos¹⁸, T. Stanev⁴¹,
A. Stasik⁵⁹, J. Stettner¹, A. Steuer³⁴, T. Stezelberger⁹, R. G. Stokstad⁹, A. Stöbl¹⁵,
N. L. Strotjohann⁵⁹, G. W. Sullivan¹⁷, M. Sutherland¹⁸, I. Taboada⁶, A. Taketa⁵³,
H. K. M. Tanaka⁵³, J. Tatar^{9,8}, F. Tenholt¹¹, S. Ter-Antonyan⁷, A. Terliuk⁵⁹, G. Tešić⁵⁶, S. Tilav⁴¹,
P. A. Toale⁵⁴, M. N. Tobin³³, S. Toscano¹³, D. Tosi³³, M. Tselengidou²⁴, C. F. Tung⁶, A. Turcati³⁸,
C. F. Turley⁵⁶, B. Ty³³, E. Unger⁵⁷, M. Usner⁵⁹, J. Vandenbroucke³³, W. Van Driessche²⁶,
N. van Eijndhoven¹³, S. Vanheule²⁶, J. van Santen⁵⁹, D. Veberic²⁸, M. Vehring¹, E. Vogel¹,
M. Vraeghe²⁶, C. Walck⁵⁰, A. Wallace², M. Wallraff¹, F. D. Wandler²³, N. Wandkowsky³³,
A. Waza¹, C. Weaver²³, A. Weindl²⁸, M. J. Weiss⁵⁶, C. Wendt³³, J. Werthebach²¹,
S. Westerhoff³³, B. J. Whelan², K. Wiebe³⁴, C. H. Wiebusch¹, L. Wille³³, D. R. Williams⁵⁴,
L. Wills⁴⁶, M. Wolf³³, J. Wood³³, T. R. Wood²³, E. Woolsey²³, K. Woschnagg⁸, S. Wren³⁵,
D. L. Xu³³, X. W. Xu⁷, Y. Xu⁵¹, J. P. Yanez²³, G. Yodh²⁷, S. Yoshida¹⁵, T. Yuan³³, M. Zoll⁵⁰

¹III. Physikalisches Institut, RWTH Aachen University, D-52056 Aachen, Germany

²Department of Physics, University of Adelaide, Adelaide, 5005, Australia

³Dept. of Physics and Astronomy, University of Alaska Anchorage, 3211 Providence Dr., Anchorage, AK 99508, USA

⁴Dept. of Physics, University of Texas at Arlington, 502 Yates St., Science Hall Rm 108, Box 19059, Arlington, TX 76019, USA

⁵CTSPS, Clark-Atlanta University, Atlanta, GA 30314, USA

⁶School of Physics and Center for Relativistic Astrophysics, Georgia Institute of Technology, Atlanta, GA 30332, USA

⁷Dept. of Physics, Southern University, Baton Rouge, LA 70813, USA

⁸Dept. of Physics, University of California, Berkeley, CA 94720, USA

⁹Lawrence Berkeley National Laboratory, Berkeley, CA 94720, USA

¹⁰Institut für Physik, Humboldt-Universität zu Berlin, D-12489 Berlin, Germany

¹¹Fakultät für Physik & Astronomie, Ruhr-Universität Bochum, D-44780 Bochum, Germany

¹²Université Libre de Bruxelles, Science Faculty CP230, B-1050 Brussels, Belgium

¹³Vrije Universiteit Brussel (VUB), Dienst ELEM, B-1050 Brussels, Belgium

¹⁴Dept. of Physics, Massachusetts Institute of Technology, Cambridge, MA 02139, USA

¹⁵Dept. of Physics and Institute for Global Prominent Research, Chiba University, Chiba 263-8522, Japan

¹⁶Dept. of Physics and Astronomy, University of Canterbury, Private Bag 4800, Christchurch, New Zealand

¹⁷Dept. of Physics, University of Maryland, College Park, MD 20742, USA

¹⁸Dept. of Physics and Center for Cosmology and Astro-Particle Physics, Ohio State University,

Columbus, OH 43210, USA

¹⁹Dept. of Astronomy, Ohio State University, Columbus, OH 43210, USA

²⁰Niels Bohr Institute, University of Copenhagen, DK-2100 Copenhagen, Denmark

²¹Dept. of Physics, TU Dortmund University, D-44221 Dortmund, Germany

²²Dept. of Physics and Astronomy, Michigan State University, East Lansing, MI 48824, USA

²³Dept. of Physics, University of Alberta, Edmonton, Alberta, Canada T6G 2E1

²⁴Erlangen Centre for Astroparticle Physics, Friedrich-Alexander-Universität Erlangen-Nürnberg, D-91058 Erlangen, Germany

²⁵Département de physique nucléaire et corpusculaire, Université de Genève, CH-1211 Genève, Switzerland

²⁶Dept. of Physics and Astronomy, University of Gent, B-9000 Gent, Belgium

²⁷Dept. of Physics and Astronomy, University of California, Irvine, CA 92697, USA

²⁸Institut für Kernphysik, Karlsruhe Institute of Technology, D-76021 Karlsruhe, Germany

²⁹Dept. of Physics and Astronomy, University of Kansas, Lawrence, KS 66045, USA

³⁰SNOLAB, 1039 Regional Road 24, Creighton Mine 9, Lively, ON, Canada P3Y 1N2

³¹School of Physics and Astronomy, Queen Mary University of London, London E1 4NS, United Kingdom

³²Dept. of Astronomy, University of Wisconsin, Madison, WI 53706, USA

³³Dept. of Physics and Wisconsin IceCube Particle Astrophysics Center, University of Wisconsin, Madison, WI 53706, USA

³⁴Institute of Physics, University of Mainz, Staudinger Weg 7, D-55099 Mainz, Germany

³⁵School of Physics and Astronomy, The University of Manchester, Oxford Road, Manchester, M13 9PL, United Kingdom

³⁶Department of Physics, Marquette University, Milwaukee, WI, 53201, USA

³⁷Université de Mons, 7000 Mons, Belgium

³⁸Physik-department, Technische Universität München, D-85748 Garching, Germany

³⁹Max-Planck-Institut für Physik (Werner Heisenberg Institut), Föhringer Ring 6, D-80805 München, Germany

⁴⁰Institut für Kernphysik, Westfälische Wilhelms-Universität Münster, D-48149 Münster, Germany

⁴¹Bartol Research Institute and Dept. of Physics and Astronomy, University of Delaware, Newark, DE 19716, USA

⁴²Dept. of Physics, Yale University, New Haven, CT 06520, USA

⁴³Columbia Astrophysics and Nevis Laboratories, Columbia University, New York, NY 10027, USA

⁴⁴Dept. of Physics, University of Notre Dame du Lac, 225 Nieuwland Science Hall, Notre Dame, IN 46556-5670, USA

⁴⁵Dept. of Physics, University of Oxford, 1 Keble Road, Oxford OX1 3NP, UK

⁴⁶Dept. of Physics, Drexel University, 3141 Chestnut Street, Philadelphia, PA 19104, USA

⁴⁷Physics Department, South Dakota School of Mines and Technology, Rapid City, SD 57701, USA

⁴⁸Dept. of Physics, University of Wisconsin, River Falls, WI 54022, USA

⁴⁹Dept. of Physics and Astronomy, University of Rochester, Rochester, NY 14627, USA

⁵⁰Oskar Klein Centre and Dept. of Physics, Stockholm University, SE-10691 Stockholm, Sweden

⁵¹Dept. of Physics and Astronomy, Stony Brook University, Stony Brook, NY 11794-3800, USA

⁵²Dept. of Physics, Sungkyunkwan University, Suwon 440-746, Korea

⁵³Earthquake Research Institute, University of Tokyo, Bunkyo, Tokyo 113-0032, Japan

⁵⁴Dept. of Physics and Astronomy, University of Alabama, Tuscaloosa, AL 35487, USA

⁵⁵Dept. of Astronomy and Astrophysics, Pennsylvania State University, University Park, PA 16802, USA

⁵⁶Dept. of Physics, Pennsylvania State University, University Park, PA 16802, USA

⁵⁷Dept. of Physics and Astronomy, Uppsala University, Box 516, S-75120 Uppsala, Sweden

⁵⁸Dept. of Physics, University of Wuppertal, D-42119 Wuppertal, Germany

⁵⁹DESY, D-15738 Zeuthen, Germany

Acknowledgment: The authors gratefully acknowledge the support from the following agencies and institutions: USA - U.S. National Science Foundation-Office of Polar Programs, U.S. National Science Foundation-Physics Division, University of Wisconsin Alumni Research Foundation, the Center for High Throughput Computing (CHTC) at the University of Wisconsin - Madison, the Open Science Grid (OSG) grid infrastructure and the Extreme Science and Engineering Discovery Environment (XSEDE); U.S. Department of Energy, and National Energy Research Scientific Computing Center; Particle Astrophysics research computing center at the University of Maryland; Institute for Cyber-Enabled Research at Michigan State University; Astroparticle Physics Computational Facility at Marquette University; Belgium - Funds for Scientific Research (FRS-FNRS and FWO), FWO Odysseus and Big Science programs, Belgian Federal Science Policy Office (Belspo); Germany - Bundesministerium für Bildung und Forschung (BMBF), Deutsche Forschungsgemeinschaft (DFG), Helmholtz Alliance for Astroparticle Physics (HAP), Initiative and Networking Fund of the Helmholtz Association; Deutsches Elektronen Synchrotron (DESY); Cluster of Excellence (PRISMA ? EXC 1098); High Performance Computing Cluster of the IT-Center of the RWTH Aachen; Sweden - Swedish Research Council, Swedish Polar Research Secretariat, Swedish National Infrastructure for Computing (SNIC), and Knut and Alice Wallenberg Foundation; Canada - Natural Sciences and Engineering Research Council of Canada, Calcul Québec, Compute Ontario, WestGrid and Compute Canada; Denmark - Villum Fonden, Danish National Research Foundation (DNRF); New Zealand - Marsden Fund, New Zealand; Australian Research Council; Japan - Japan Society for Promotion of Science (JSPS) and Institute for Global Prominent Research (IGPR) of Chiba University; Korea - National Research Foundation of Korea (NRF); Switzerland - Swiss National Science Foundation (SNSF).

IceCube-Gen2: the next-generation neutrino observatory for the South Pole

The IceCube-Gen2 Collaboration[†]

[†] http://icecube.wisc.edu/collaboration/authors/icrc17_gen2

E-mail: jvansanten@icecube.wisc.edu

The IceCube Neutrino Observatory is a cubic-kilometer Cherenkov telescope buried in the ice sheet at the South Pole that detects neutrinos of all flavors with energies from tens of GeV to several PeV. The instrument provided the first measurement of the flux of high-energy astrophysical neutrinos, opening a new window to the non-thermal universe. Here we present design studies for IceCube-Gen2, the next-generation neutrino observatory for the South Pole. IceCube-Gen2 will have an instrumented volume nearly 10 times greater than IceCube alone, substantially increasing sensitivity to high-energy neutrinos. On the surface, a large air shower detector will veto high-energy atmospheric muons and neutrinos from the southern hemisphere, enhancing the reach of astrophysical neutrino searches. In the ice, a number of new optical module designs currently being evaluated will allow for substantially increased photosensitive area per unit cost. We show how these different sensor designs affect the instrument's ability to resolve the sources of astrophysical neutrinos.

Corresponding author: J. van Santen*

DESY, Platanenallee 6, D-15738 Zeuthen, Germany

*35th International Cosmic Ray Conference — ICRC2017
10–20 July, 2017
Bexco, Busan, Korea*

*Speaker.

1. From IceCube to IceCube-Gen2

IceCube is a cubic-kilometer Cherenkov telescope buried in the ice sheet at the South Pole [1] that detects neutrinos of all flavors with energies from tens of GeV to several PeV. While the instrument provided the discovery of the flux of high-energy astrophysical neutrinos [2, 3, 4, 5], the sources of these neutrinos have remained out of reach [6]. Learning more about the sources and resolving their locations will require collecting significantly more neutrinos per year than are possible with IceCube alone. To that end, design studies are underway for IceCube-Gen2, a next-generation neutrino observatory for the South Pole.

IceCube-Gen2 will encompass the existing IceCube array [1], covering the TeV range, as well as an array of new, widely-spaced strings to increase sensitivity above ~ 10 TeV. Additional components would expand IceCube-Gen2 into a wide-band neutrino facility. A large surface array would lower the energy threshold for southern-sky neutrino searches by vetoing mildly-inclined air showers [8, 9]. A radio array would detect cosmogenic neutrinos above ~ 100 PeV [10]. A dense infill inside the existing DeepCore would extend atmospheric oscillation measurements and dark matter searches down to several GeV [11]. Here we focus on the sensitivity characterization of the high-energy array and the surface veto array.

The high-energy array will detect neutrinos primarily via two channels: tracks, produced by relativistic muons crossing the detector, and cascades, isolated energy depositions induced by charged-current ν_e , ν_τ , and neutral-current interactions of all neutrino flavors. Sensitivity to individual sources scales with the rate of track events, and thus with the projected area of the detector, while sensitivity to the energy spectrum and flavor composition of the high-energy diffuse flux scales with the rate of cascade events, and thus the instrumented volume. Several geometries are under consideration for the high-energy array, with instrumented volumes ranging from 6.2 to 9.5 km³. Each detector geometry strikes a different compromise between projected area and contained volume. For the studies described here we focus on the “sunflower” layout shown in Fig. 1.

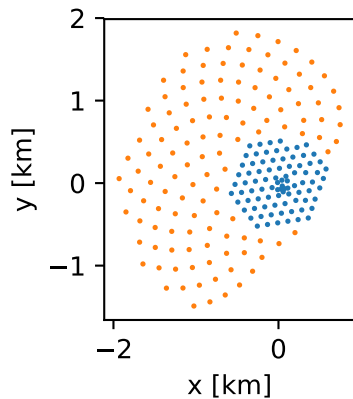


Figure 1: View of IceCube-Gen2 strings from above in the “sunflower” layout. The 120 new strings (shown as orange points) are spaced 240 m apart and instrumented with 80 optical modules over a vertical length of 1.25 km. The total instrumented volume is 7.9 km³, nearly 10 times larger than IceCube alone (blue points).

2. Sensitivity to astrophysical neutrinos

We estimate the sensitivity of each proposed detector configuration to various astrophysical neutrino production scenarios using a set of mock likelihood analyses modeled on previous IceCube results. In the following we present our method for obtaining neutrino event rates from basic detector performance quantities such as muon effective area and energy resolution. We then briefly discuss the likelihood technique. Finally, we use the technique to demonstrate the potential of the IceCube-Gen2 high-energy array to measure properties of the observed quasi-diffuse neutrino flux and discover steady point sources of neutrinos.

2.1 Event rate calculation

We have parameterized the performance of each of our proposed detector geometries to detect and reconstruct tracks and cascades. We then calculate event rates by folding these quantities with the probabilities for neutrinos of a particular flavor and energy to produce one of these two event signatures. This approach allows us to separate the performance of the detector from limitations imposed by the physics of neutrino interactions, e.g. absorption in the Earth.

For muon tracks, the detector performance is characterized by four quantities: muon effective area, surface veto coverage, energy resolution, and point spread function.

Muon effective area The left panel of Fig. 2 shows the muon effective area of the 240 m “sunflower” geometry. For PeV muons it is nearly identical to the instrumented area, but drops significantly below 10 TeV due to large string-to-string spacing.

Surface veto footprint and threshold The surface veto reduces the background from penetrating muons by identifying and rejecting high-energy air showers that reach ground level in or near it. We model its effect by splitting the projected area of the in-ice array in each zenith band into a portion that is covered by the surface veto footprint (75 km² by default) and one that is not. Within the coverage of the surface veto, the background from penetrating atmospheric muons is removed entirely above a fixed threshold energy (100 TeV by default), while outside it is unaffected. A 75 km² surface array would cover the entire 240 m sunflower array up to zenith angles of 45 degrees, and half of the array up to 70 degrees.

Muon energy resolution TeV muons predominantly lose energy stochastically, leading to significant spread in the muon energy observables associated with a single true muon energy. The muon energy resolution is a parameterization of the reconstructed energy distribution after the selection described above.

Point spread function The point spread function parameterizes the distribution of the angular distance between the true muon direction and the reconstructed direction as a function of zenith angle and muon energy. The right panel of Fig. 2 shows example median opening angle distributions.

The performance criteria for cascades are simpler. The muon effective area is replaced by an effective volume of ice inside which penetrating atmospheric muons can be cleanly separated from neutrino-induced cascades. In analogy to [3], we parameterize the effective volume for the

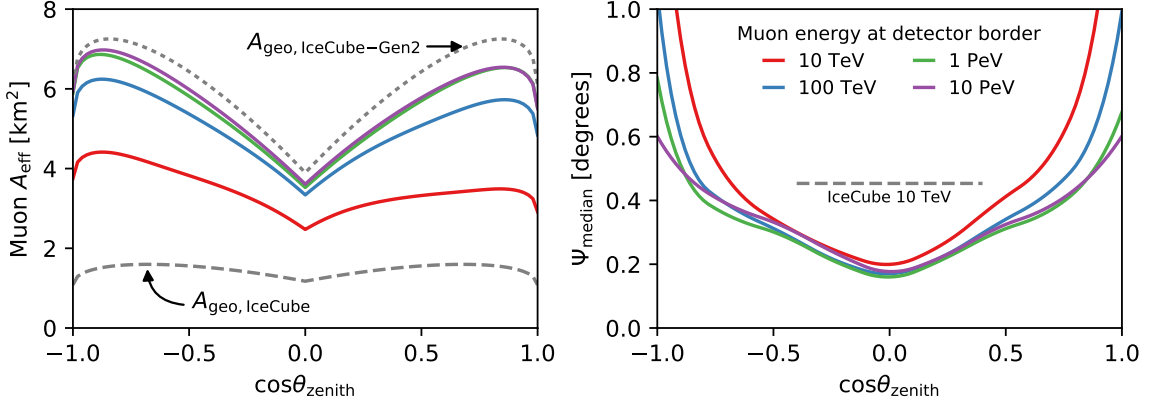


Figure 2: Muon detection and reconstruction performance of 240 m “sunflower” geometry. The left panel shows the average muon effective area after quality cuts as a function of zenith angle at 4 selected muon energies, evaluated at the border of the high-energy array. The geometric area of the array is shown for comparison. The right panel shows the median angular distance between the reconstructed and true muon direction. The typical angular error for IceCube is shown for comparison.

240 m “sunflower” geometry as 6.3 km^3 above 200 TeV deposited energy [12] and 0 below. A cascade deposits all of its energy over a short distance, making it simpler to infer its total energy. We parametrize the deposited energy resolution as $\sigma_{\log_{10}(E_{\text{obs}}/E_{\text{dep}})} = 0.04 \cdot [1 + (E_{\text{dep}}/1 \text{ PeV})^{-1/2}]$. The point spread function is omitted entirely. We do not take the surface veto into account for cascade events. For simplicity’s sake we also neglect the possibility that tracks would start inside the fiducial volume or that charged-current ν_{τ} interactions inside the fiducial volume could be positively identified.

2.2 Sensitivity and discovery potential

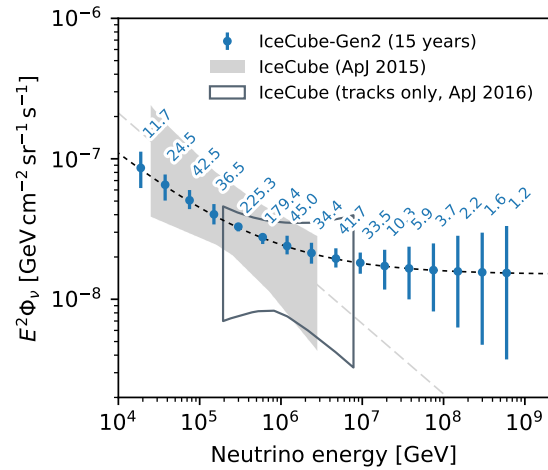
We use these predicted event rates to calculate parameter limits for various benchmark analyses, modeling the sensitivity and discovery potential of each analysis as a binned Poisson likelihood ratio test. We define the *sensitivity* as the median 90% confidence level (CL) upper limit on a parameter (e.g. the flux from a candidate neutrino source) that would be obtained in repeated experiments if the parameter were 0, and the *discovery potential* as the value of the parameter required to exclude 0 at a CL equivalent to 5σ [13]. In both cases, we calculate the median test statistic using an Asimov dataset [14] rather than an ensemble of pseudo-data realizations.

Here we present two broad categories of searches: quasi-diffuse analyses, which measure the energy spectrum and flavor composition of the superposition of all astrophysical neutrino sources, and point-source analyses, which search for neutrinos from individual sources or catalogs of similar sources. The quasi-diffuse analyses use both track and cascade events, while the point-source analyses use track events only.

2.3 Quasi-diffuse flux

IceCube has discovered a quasi-diffuse astrophysical neutrino flux both in the starting event (cascade-dominated) [3] and up-going muon channels [5], but its origins remain unknown. The observed flux level is compatible with the widely assumed hypothesis that these neutrinos are associated with the production sites of ultra-high-energy cosmic rays (UHECR) [15]. The limited

Figure 3: IceCube-Gen2 quasi-diffuse neutrino flux measurement after 15 years of operation. The dotted line shows a superposition of a soft ($E^{-2.5}$) and a hard (E^{-2}) component that is compatible with both the low-threshold, all-channel IceCube analysis [16] (filled grey band) and the high-threshold, muon-only analysis [5] (outlined band). The blue bars show the median range of fluxes allowed at 68% CL in each range of neutrino energies, along with the number of events attributable to each range. These would allow for a clear distinction between the soft spectrum observed at lower energies (grey dashed line) and a hard spectrum that continues to the energy range of the UHECR.



event rate in IceCube, however, prohibits strong statements about the behavior of the flux above a few PeV. To make a direct statement about the connection, we must measure the flux at higher energies.

To demonstrate the energy reach of the IceCube-Gen2 high-energy array, we construct a differential flux measurement similar to [3]. We use both the incoming track and cascade channels, and allow downgoing tracks that pass through the footprint of the surface veto. Furthermore, we assume a combined measurement using 15 years of IceCube data and 15 years of IceCube-Gen2, using muon effective areas and cascade effective volumes similar to [5] and [3] to predict the number of cascades and incoming tracks, respectively, in IceCube. As a background we assume only atmospheric neutrinos, using the fluxes of [17, 18], modified to account for the cosmic ray knee as in [5]. The signal hypothesis is a set of piecewise E^{-2} power law fluxes, where each segment is allowed to vary independently. The result of such an analysis is shown in Fig. 3. The error bars on each point show the median range of fluxes that would be allowed by the data in each energy range. The flux would remain distinguishable from 0 well into the hundreds of PeV, providing valuable overlap with radio detection, and cementing the connection between high-energy neutrinos and UHECR.

Another important aspect that can be explored with IceCube-Gen2 is the nature of the acceleration environments that produce high-energy neutrinos. If the neutrinos are produced via pion decay in the presence of strong magnetic fields, then synchrotron cooling of the pions and secondary muons will lead to breaks in the spectra of muon and electron neutrinos at the source, making the flavor ratio at Earth transition from roughly 1:1:1 to 1:1.8:1.8 over a decade in energy [19]. If the transition energy lies in the range of IceCube-Gen2, it will be observable as a break in the energy spectrum measured by IceCube-Gen2 that behaves differently in tracks and cascades.

Figure 4 shows an example of a search for flavor dependence in such a break in a case where the critical energy is 2 PeV, using the same detectors, exposures, and backgrounds as in the flux unfolding example above. Here, the model signal spectrum is divided into two components whose internal flavor compositions are allowed to vary independently. The assumed flux is $E^2\Phi_\nu = 10^{-8} \text{ GeV cm}^{-2} \text{ sr}^{-1} \text{ s}^{-1}$ per flavor for $E_\nu \lesssim 1 \text{ PeV}$, softening to E^{-4} for $E_\nu \gtrsim 10 \text{ PeV}$. The flavor composition measured above 1 PeV would exclude the expected 1:1:1 at Earth at 95% CL.

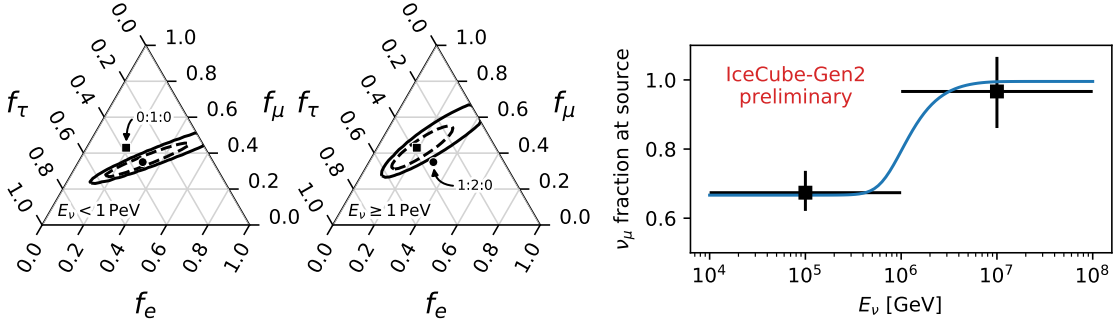


Figure 4: Measurement of a muon-damping break at 1 PeV with IceCube-Gen2. The left panels show the constraints on the flavor ratio at Earth below and above 1 PeV, respectively. The points show the expected ratios at Earth from muon-damped pion decay ($[v_e : v_\mu : v_\tau]_{\text{source}} = 0 : 1 : 0$) and complete pion decay (1:2:0). The dotted contours give the 68% CL allowed region, while the solid lines correspond to 90% CL. The error bars in the right panel show the 68% CL constraints on the muon-neutrino fraction at the source assuming standard oscillations over long baselines [20], while the line shows the injected flavor composition at the source.

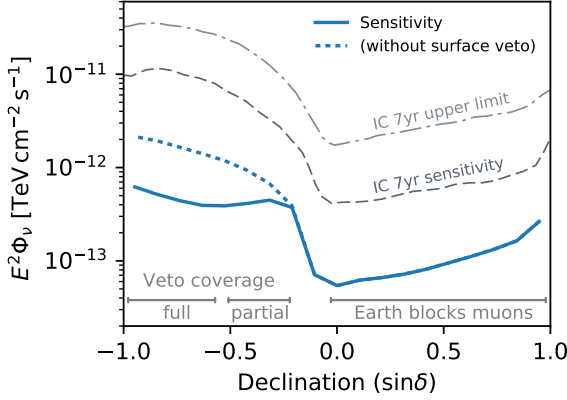


Figure 5: Integrated sensitivity for an E^{-2} flux from a single source after 15 years of IceCube operation followed by 15 years of IceCube-Gen2. The sensitivity and trials-corrected upper limit of the all-sky point source search with 7 years of IceCube data [6] are shown for comparison. The discovery potential is typically 2.5 times larger than the sensitivity. The surface veto improves both discovery potential and sensitivity by a factor $\gtrsim 3$ for $\sin \delta \lesssim -0.5$.

2.4 Point sources

While the quasi-diffuse astrophysical neutrino flux has been observed, its sources have remained too faint to detect. The significantly larger instrumented area of IceCube-Gen2 will, however, allow sensitivity to fluxes from individual sources that are fainter than current limits.

Figure 5 shows integrated sensitivities and discovery potentials to an E^{-2} flux from a single source, using only through-going track events. Neutrino absorption in the Earth reduces the sensitivity towards the North Pole. In the Southern sky, overall sensitivity is reduced due to the energy threshold imposed by the surface veto and the limited target mass for neutrino interactions between the surface and the detector. Like IceCube, IceCube-Gen2's best sensitivity is at the local horizon ($\delta = 0$), where the projected density of the instrumentation and the range of neutrino-induced muons is greatest.

3. Outlook: improved sensor designs

The performance estimates shown above were obtained with the PINGU DOM (PDOM) [21], an updated version of the IceCube DOM that uses the same 10-inch, high-quantum-efficiency PMT

as DeepCore. Newer sensor designs can potentially provide better sensitivity. Two new designs currently under development are the D-Egg [22, 23], with two 8-inch PMTs placed back-to-back in an ellipsoidal pressure vessel, and the mDOM [24], a smaller adaptation of the KM3NeT sensor with 24 3-inch PMTs arranged in a nearly-spherical pressure vessel. Aside from some ability to resolve the directions of photons, these differ from the PDOM primarily in the total amount and the orientation of their photon effective area, as shown in Fig. 6a. While the PDOM's single downward-facing PMT is most sensitive to upward-going photons ($\cos\eta \sim 1$), the D-Egg is symmetrically sensitive to upward- and downward-going photons with a total photon effective area 1.5 times greater than the PDOM, and the mDOM has nearly isotropic sensitivity with a total effective area 2.2 times greater than the PDOM. This could be increased to nearly 3 times by using super-bialkali (SBA) photocathode PMTs.

These larger sensors can improve performance either by a) increasing the total photon effective area per string, b) concentrating the same effective area in fewer modules per string, or c) allowing strings to be placed farther apart for increased neutrino effective area. Fig. 6b illustrates a minimal version of the potential gains from (a) using the point source discovery potential at $\delta = 0$. The improved point source sensitivity arises from an improvement in reconstruction efficiency and accuracy for muons with energies smaller than roughly 100 TeV with increased photon effective area per sensor. While the angular resolution for horizontal muons using only the arrival time of the first photon [25] does not appear to benefit directly from the ability of segmented sensors to resolve photon directions, we expect these sensors to improve angular resolution for cascade events as well as the rejection of penetrating atmospheric muons.

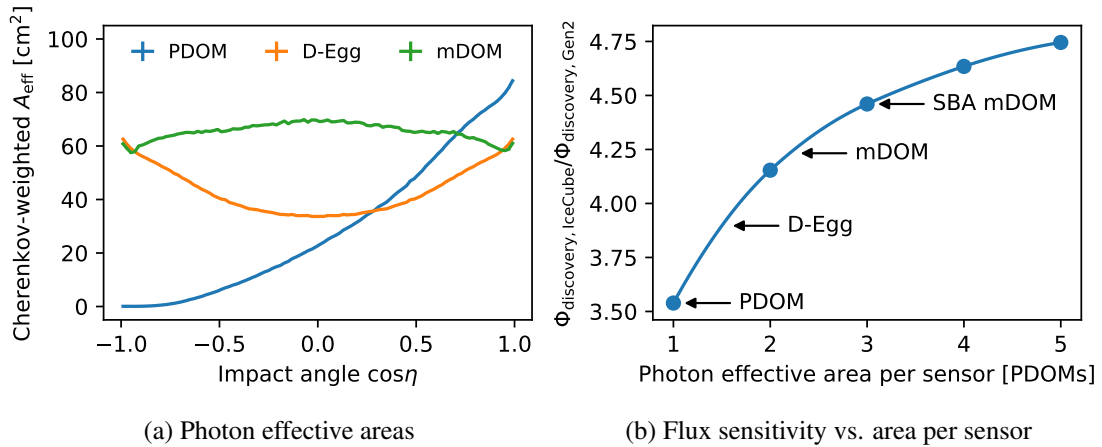


Figure 6: Sensitivity improvements from new sensor designs. (a) shows the effective area of the D-Egg and mDOM compared to the PDOM; the total area of the D-Egg is 1.5 times larger than the PDOM, while the mDOM is 2.2 times larger. (b) shows how larger sensors would improve the ability to discover a point source at $\delta = 0$. A sunflower array with 120 strings spaced 240 m apart with 80 PDOMs each would be able to discover sources 3.5 times fainter than IceCube, while increasing the effective area of each sensor by 3 times (for example, by replacing each PDOM with an mDOM with SBA-photocathode PMTs) would increase this factor to 4.5.

4. Summary

IceCube-Gen2 will be a wide-band facility that detects neutrinos from several GeV to hundreds of PeV. Here we have presented sensitivity studies using two of its components, the high-energy in-ice array and the surface veto array. Together these can enable measurements of the astrophysical neutrino flux at the level of $E^2\Phi_\nu = 10^{-8} \text{ GeV cm}^{-2} \text{ sr}^{-1} \text{ s}^{-1}$ per flavor up to hundreds of PeV, measurements of the flavor composition of the astrophysical neutrinos in the PeV range, and detection of steady point sources that are 3.5 to 4.5 times fainter than those detectable with IceCube alone.

References

- [1] **IceCube** Collaboration, M. G. Aartsen et al., *JINST* **12** (2017), 03 P03012.
- [2] **IceCube** Collaboration, M. G. Aartsen et al., *Science* **342** (2013) 1242856.
- [3] **IceCube** Collaboration, M. G. Aartsen et al., *Phys. Rev. Lett.* **113** (2014) 101101.
- [4] **IceCube** Collaboration, M. G. Aartsen et al., *Phys. Rev. Lett.* **115** (2015), 8 081102.
- [5] **IceCube** Collaboration, M. G. Aartsen et al., *Astrophys. J.* **833** (2016), 1 3.
- [6] **IceCube** Collaboration, M. G. Aartsen et al., *Astrophys. J.* **835** (2017), 2 151.
- [7] **IceCube** Collaboration, M. G. Aartsen et al., [arXiv:1412.5106](https://arxiv.org/abs/1412.5106).
- [8] **IceCube** Collaboration, [PoS \(ICRC2017\) 967](https://pos.icrc2017.org/967) (these proceedings).
- [9] **IceCube-Gen2** Collaboration, [PoS \(ICRC2017\) 1055](https://pos.icrc2017.org/1055) (these proceedings).
- [10] **ARA** Collaboration, P. Allison et al., *Astropart. Phys.* **70** (2015) 62–80.
- [11] **IceCube** Collaboration, M. G. Aartsen et al., *J. Phys.* **G44** (2017), 5 054006.
- [12] **IceCube-Gen2** Collaboration, [PoS \(ICRC2017\) 945](https://pos.icrc2017.org/945) (these proceedings).
- [13] G. C. Hill and K. Rawlins, *Astropart. Phys.* **19** (2003) 393–402.
- [14] G. Cowan, K. Cranmer, E. Gross, and O. Vitells, *Eur. Phys. J.* **C71** (2011) 1554.
- [15] E. Waxman and J. N. Bahcall, *Phys. Rev.* **D59** (1999) 023002.
- [16] **IceCube** Collaboration, M. G. Aartsen et al., *Astrophys. J.* **809** (2015), 1 98.
- [17] M. Honda, T. Kajita, K. Kasahara, S. Midorikawa, and T. Sanuki, *Phys. Rev.* **D75** (2007) 043006.
- [18] R. Enberg, M. H. Reno, and I. Sarcevic, *Phys. Rev.* **D78** (2008) 043005.
- [19] T. Kashti and E. Waxman, *Phys. Rev. Lett.* **95** (2005) 181101.
- [20] M. C. Gonzalez-Garcia, M. Maltoni, and T. Schwetz, *JHEP* **11** (2014) 052.
- [21] **IceCube PINGU** Collaboration, P. Sandstrom, *AIP Conf. Proc.* **1630** (2014) 180–183.
- [22] **IceCube-Gen2** Collaboration, [PoS \(ICRC2017\) 1051](https://pos.icrc2017.org/1051) (these proceedings).
- [23] **IceCube-Gen2** Collaboration, [PoS \(ICRC2017\) 1038](https://pos.icrc2017.org/1038) (these proceedings).
- [24] **IceCube-Gen2** Collaboration, [PoS \(ICRC2017\) 1047](https://pos.icrc2017.org/1047) (these proceedings).
- [25] **AMANDA** Collaboration, J. Ahrens et al., *Nucl. Instrum. Meth.* **A524** (2004) 169–194.

IceAct: Imaging Air Cherenkov Telescopes with SiPMs at the South Pole for IceCube-Gen2

The IceCube-Gen2 Collaboration[†]

[†] http://icecube.wisc.edu/collaboration/authors/icrc17_gen2

E-mail: jauffenb@icecube.wisc.edu

IceCube-Gen2 is planned to extend the IceCube Neutrino Observatory at the geographic South Pole. For neutrino astronomy, a large sample of well-reconstructed astrophysical neutrinos with very low background is essential. The main background for this signal consists of muons and neutrinos, which are produced in cosmic-ray air showers in the Earth's atmosphere. The coincident detection of these air showers by the surface detector IceTop has already proven the concept of vetoing atmospheric neutrinos and muons in a limited field of view centered around the South Pole. This motivates a large extension of IceTop to detect cosmic rays more efficiently over a large field of view. As part of these extension plans, small imaging air Cherenkov telescopes based on SiPM cameras and optimized for harsh environments, referred to as IceAct are considered. Compared to IceTop stations, these telescopes may be an efficient way to lower the detection threshold for air showers at the cost of a lower duty cycle. In addition small ACTs in combination with IceTop and IceCube can improve the capabilities to measure the composition of the CR spectrum starting at 2 PeV. We will present the progress and future plans of the IceAct project including first coincident data of an IceAct prototype with IceCube.

Corresponding author: Jan Auffenberg^{*1}

¹ *RWTH Aachen University*

*35th International Cosmic Ray Conference — ICRC2017
10–20 July, 2017
Bexco, Busan, Korea*

*Speaker.

1. Introduction

IceCube [1] has measured an astrophysical neutrino flux with very high significance but no evidence for a point source has been found [2, 3] so far. In the region above 100 TeV primary neutrino energy the measured diffuse flux is significantly above the background of cosmic-ray induced neutrinos and muons. One of the main tasks of an extended IceCube detector, *IceCube-Gen2*, will be the detection and high-quality reconstruction of a sufficient number of astrophysical neutrino events for astronomical observations and the measurement of the corresponding neutrino spectrum with high precision (see also [4, 5]).

The main backgrounds for extraterrestrial neutrino detection are

cosmic-ray induced particles. One way to suppress these backgrounds in IceCube is to look for particles that traversed the whole Earth, leaving only neutrinos - astrophysical and atmospheric. In the southern sky, the cosmic-ray induced muon background is dominant because high-energy muons (>400 GeV) are not absorbed within at least 1.5 km overburden of ice above the detector. However, cosmic-ray induced air showers can be detected with dedicated air shower arrays at the surface [6]. Such a surface detector can be used to veto the cosmic-ray muons reaching the deep in-ice detector. To some extent, such a veto detector is able to select and suppress even the atmospheric neutrino background as they are also accompanied by air showers on the surface. In fact, IceTop is already used today in several analyses to suppress the atmospheric background and increase the sensitivity of IceCube for astrophysical neutrinos in the southern sky [7, 8]. The properties of IceTop as a veto motivate further studies of a specialized detector to very efficiently detect cosmic-ray muons already at the surface. This offers the possibility to select neutrinos that interacted anywhere in the entire ice sheet above the IceCube in-ice detector as astrophysical neutrino candidates. Of special interest are neutrinos from directions of possible neutrino sources that are motivated by high energy gamma ray detections. One example is the Galactic center of the milky way, located 29° above the horizon at the South Pole. The possible impact of a surface veto detector to astrophysical neutrino measurements with IceCube is discussed in [4].

Detector extensions to veto cosmic-ray induced signals on the surface have to be very efficient in different ways:

- A low energy threshold and high detection efficiency of a surface veto is strongly related to

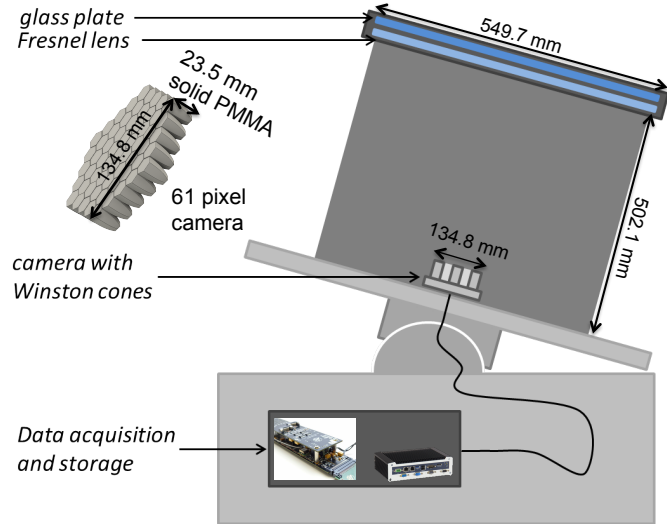


Figure 1: Drawing of the IceAct telescope prototype with a 61 pixel camera. A similar IceAct demonstrator equipped with a 7 pixel camera was deployed at the South Pole on the roof of the counting house of the IceCube neutrino observatory.

the detectable neutrino flux.

- A large duty cycle is needed for a surface veto detector to detect as many astrophysical events as possible.
- The number of detectable astrophysical events increases linearly with the azimuthal coverage of a surface array. With increasing declination the length of the active Volume (ice) increases. Thus a neutrino will more likely interact with increasing declination and produce a signal in the in-ice detector. In the vertical case, only the ice directly above the detector (about a factor of 2.5) is gained, while e.g. in the direction of the Galactic Center (declination $\theta = 61^\circ$) the active volume is already about six times larger.
- The detection system has to be easy to deploy and operate.

The most obvious option for a surface veto are particle detectors which measure the Cherenkov- or scintillation light produced in an enclosed active volume [9]. First simulations based on shower parameterizations underline the importance of large detection volumes and sensitivity to the electromagnetic and the muonic component of the air shower [10]. Uncertainties from intrinsic fluctuations in the air-shower front at the surface in this case are of primary importance in determining the veto efficiency and its energy dependence.

In the following, an array of small imaging air Cherenkov telescopes is discussed as an alternative detection method which uses the atmosphere as the active volume. First we discuss an estimated air Cherenkov telescope array and the technical properties of imaging air Cherenkov telescopes needed for a surface veto detector. After that, a 61 pixel IceAct prototype telescope that has been built for the South Pole is described. In addition, we show first data that was taken with a 7 pixel IACT demonstrator at the South Pole in coincidence with IceCube.

2. Criteria for an air Cherenkov veto array at the South Pole

In the following we will briefly discuss the motivation and required properties of possible IceAct arrays that could be operated at the South

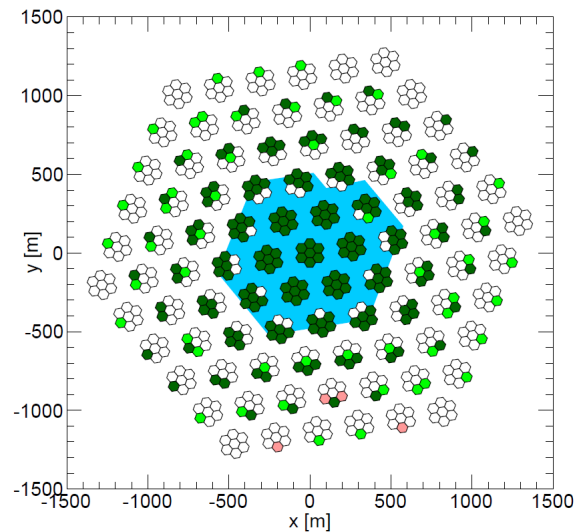


Figure 2: Add on Array for IceTop. The blue region indicates the footprint of IceTop. Each 7 connected hexagons build one station of 7 telescopes. Each telescope looks in a different direction of the sky, opening in total a field of view of 18° . The colors of the different telescopes (hexagons) indicate the importance of the telescope. Deep green telescopes shield >50 optical modules of from IceCube deep in the ice from cosmic ray signals (see the right Figure 2). The light green telescopes cover between 10 and 50 optical modules. The red telescopes cover less than 10 telescopes. The white telescopes are not needed.

Pole as a surface veto for cosmic-ray air showers to detect astrophysical neutrinos. A surface detector on top of IceCube to veto air shower induced signals in the in-ice detector offers the possibility to improve the astrophysical neutrino search of IceCube in various ways. One example is the detection of well reconstructed high energy muon neutrinos [4]. Such neutrinos interacting in the ice above the instrumented volume of the deep array could be included with a calculated probability of being of astrophysical origin.

In different analyses IceCube has measured a diffuse astrophysical flux with a spectral index of $E^{-2.1}$ to $E^{-2.8}$ harder than the inclusive flux of atmospheric leptons. Thus, a veto detector needs to work increasingly more efficient the lower the energy threshold for astrophysical neutrino detection is set. Particle detector arrays on the ground suffer from a limited active detector volume. At energies where the particle density on the ground is too low, the veto efficiency will drop. As each telescope pixel of IACT's is monitoring the entire atmosphere in its field of view and the Cherenkov light emission is much more homogeneous compared to the distribution of the charged particles, the energy threshold of the IACTs is not constrained by the sparsity of the detectors. It is mainly dependent on the detection efficiency for photons, the photon background, and the photons reaching the telescope at the first place. Conventional IACTs are much too expensive to cover a large field of view. The only requirement for IACTs for the veto case is the detection of photons from certain directions within the directional uncertainty of IceCube and with a moderate probability to trigger on background photons. As a result the field of view of our pixels can be relative large above 1° and the overall size of the telescope can be well below 1 m^2 . This drops the cost of a single telescope to well below \$ 10 000 [11] including a DAQ that is based on Target7 [12] modules.

2.1 IceAct Telescope application

First simulation studies of IceAct arrays to veto cosmic ray induced background for IceCube were reported [13]. They assume the photon detection efficiency of single telescopes is comparable to those of the IceAct prototype [11]. With a 4 PE detection threshold on a night sky background taken from La Palma (accurate measurements for the South Pole need to be implemented in the future) and CORSIKA [14] simulations under South Pole conditions we find in the order of 200-300 telescopes to be sufficient to cover the most vertical 18° above the IceCube in-ice detector completely (see Figure 2). Such an array of telescopes has a stable threshold at about 50 TeV cosmic ray primary energy, well below that of IceTop (in the order of 300 TeV). Given that IceTop as a veto detector results in about 0.1 neutrinos/year [15] such a telescope array with a comparable field of view would be able to identify astrophysical with a neutrino/year rate dependent on the spectral index of the flux and the duty cycle of the array. Our example array covers a larger part of the IceCube in-ice detector compared to IceTop, which increases the expected number of astrophysical neutrinos further.

Another array of telescopes that is efficiently detecting cosmic ray induced background from the direction of the Galactic Center is also of particular interest as the Galactic Center is a prominent candidate for a neutrino point source motivated by the high energy gamma detection of Hess [16]. With the geographic South Pole as the frame of reference the Galactic Center rotates around IceCube with a declination of 29° above the horizon. Vetoing cosmic-ray background from this region would require rings of telescopes deployed around IceCube. This type of array geometry is also under consideration and will be explored and require also several hundred telescopes.

Finally, we note that an IceAct array of the type shown in Figure 2 would add a powerful signal component for cosmic-ray physics with IceCube. IceActs measure the air Cherenkov light emission of the electromagnetic component along the shower axis. This information is complementary to the high energy muon detection of the IceCube detector in the ice and the particle detection by IceTop on the ground [17].

3. Development of the IceAct prototype telescope

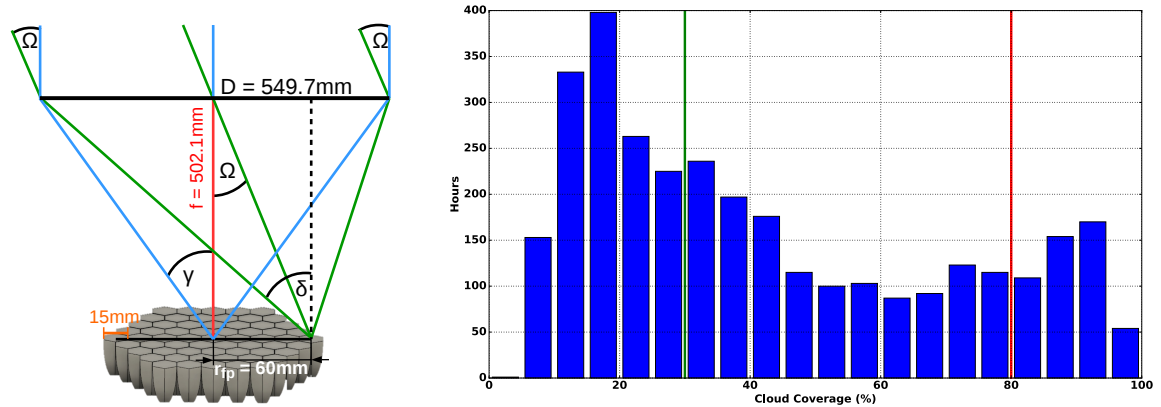


Figure 3: Left: The acceptance angle that is required for the central Winston cone and a Winston cone on the side of the camera. γ is 28.7° , δ is 33.7° . Right: Duty cycle of SIPM based IACTs determined from observations with a simple 175° sky camera. The plot shows the number of hours in which a certain amount of cloud coverage was found. Analyses estimate that in about 25% of the time darkness with no clouds is found in each given direction, with large uncertainties.

Efficiently running an air Cherenkov telescope at the South Pole requires special treatment of the mechanics and electronics to account for the extreme environmental properties, including low temperatures and drifting snow. Further design considerations follow from the planned use as a veto for air showers. Figure 1 shows a schematic of the current IceAct telescope design. In the following we describe the optical properties of the telescope along the signal path for incoming light. First, incoming light passes a 97% UV-transparent glass plate that protects the entire following system from small snow crystals, dust and very cold temperatures. This is followed by a Fresnel lens with a 12° field of view and a diameter of 549.7 mm (ORAFOL Fresnel Optics GmbH 510 mm SC 943 lens). A carbon cylinder sets the distance of the lens to the SiPM camera to 514 mm and ensures a shielding from scattered background light and snow. 61 specially designed PMMA Winston-Cones are sitting in the front of the camera. They have a hexagonal entrance window and a quadratic output window focusing the light on 6x6mm SensL-J SiPMs (see Figure 3 on the left). The first telescope at the South Pole had round aluminum cones and only the central 7 pixels equipped. Each single pixel of this camera has a detection efficiency of $14 \pm 3\%$ in the region of $\pm\Delta$ at 380nm wavelength including the detection efficiency of the SensL-C 6x6 mm SiPM and including the

limited fill factor. Figure 3 motivates the reason for the chosen acceptance angle. Here $\Delta = 33.7^\circ$ is the maximum angle in which light needs to be collected with the cones.

3.1 61 Pixel Camera of the IceAct Prototype Telescope

The central part of the IceAct prototype telescope is the 61 pixel SIPM camera. The radius r_{fp} of the focal plane is 60 mm, where the entrance window of the Winston cones is located in the focal plane of the Fresnel lens at 350 nm wavelength (502.1 mm). The left Figure 3 summarizes these numbers. The overall light detection efficiency from the direction of $0^\circ - \delta$ is simulated to be in the order of 32% at 380 nm wavelength including the detection efficiency of the SensL-C 6x6 mm SIPM and the limited fill factor.

Including the lens and the front glass the overall light detection efficiency of the telescope in its FOV is about 15% for Cerenkov light on the ground from 300-400 nm. Wavelength and direction dependent measurements are ongoing. Measurements of the environmental properties at the South Pole for the operation of IACTs and the successful operation of IceAct prototypes at the South Pole are important to determine the potential of an extended IceAct array. One very important parameter to calculate the potential of a large IceAct array is the expected duty cycle for operation. To investigate the duty cycle of IceActs at the South Pole careful measurements of the condition of the atmosphere are necessary. A first step in this direction is the analysis of pictures that were taken with a simple 175° sky camera that was installed at the South Pole from 2014-2016. During one dark period from 2015-2016 the taken data were analyzed for cloud coverage in the sky by monitoring the appearance and absence of stars. Monitoring 150 stars gives a first estimate on the overall duty cycle achievable at the South Pole. Analysis shows that for 25 % of the time per year the sky in each given direction is dark and clear. Because of the large uncertainties (in both directions) of this measurement all our estimates assume that the field of view of a given telescope is dark and free of clouds or bright auroras 20 % of the time. This star disappearance measurement is in agreement with LIDAR-data analyses from the South Pole [18]. A professional camera for night sky observations was installed at the South Pole in 2016. The data will be used to confirm the results of this measurement.

3.2 Coincident Data of the IceAct Demonstrator Telescope at the South Pole

Together with the wooden stand an IceAct demonstrator was deployed on the roof of the IceCube counting house (ICL) in 2016 to start elaborating the capabilities of IceAct to calibrate the cosmic ray flux detected by IceCube. The telescope has seven pixels for an 4° field of view and can look from 45° above zenith to vertical. It was operating from May 12th 2015 till August 20th 2016. Almost one month of stable data was taken in physics mode in coincidence with IceCube and IceTop. The IceAct demonstrator was autonomously triggering whenever two pixels saw a signal above threshold. In the case of a trigger in IceCube at the same time, IceCube records an IceAct trigger time stamp. In addition an independent time marker was recorded by IceAct. We also sent trigger signals to IceCube forced by two independently working 60 MHz clocks and recorded corresponding time markers within IceAct. In case of an independent IceCube trigger the flags that are sent to IceCube are recorded. This information was used to do a time calibration between IceCube and the IceAct demonstrator. We are now able to analyze air shower events that were recorded with all three subsystems IceAct, IceTop, and IceCube. Figure 4 shows one example

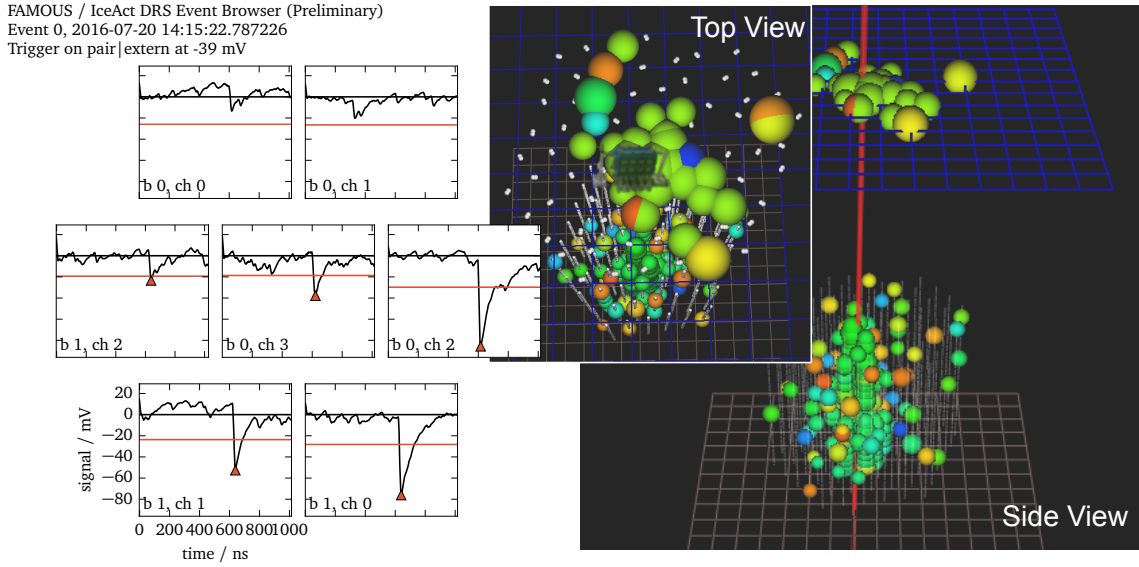


Figure 4: Example event of a coincidence of all three detector components IceTop, IceCube and IceAct. On the left one can see 5 SIPM pixels of the telescope with a clear signal above threshold. On the right is an event view of the IceTop and the IceCube light detection pattern. The color represents timing, the size of the bubble the light amount detected by the optical sensors. The time interval bins in the color code were expanded to $7 \mu\text{s}$ so that all hits in green are associated with the same event. The building (ICL) in the top view marks the position of the telescope.

event of triple coincidence. Displayed are the amount of light in IceTop on top of light signals in the deep IceCube detector. The color indicates the time of the light detection. The graphs show the corresponding SIPM pulses of the SIPM pixels from the IceAct Demonstrator. The event hit the surface close to the IceCube counting house (ICL), the location of the telescope. The ICL building is also visualized in the plot. Future goals of data analyses are to determine the energy threshold and detection efficiency as a function of the distance to the shower axis. Here the reconstruction of the air showers from IceTop and IceCube will be very helpful. This ongoing study will underline the capability to run an array of IACTs at the South Pole.

4. Summary and Outlook

We have described the idea of a large IceAct array to veto cosmic rays for astrophysical neutrino detection with IceCube in the southern sky. First simulations of arrays suggest that 200-300 efficiently working IceActs could be sufficient for a veto detector enhancing IceTop or covering the Galactic Center.

IceActs are small and robust telescopes that cost below 10 k\$. Being cost efficient they are a very good candidate technology to be deployed and operated in large numbers for veto detectors. A veto detector of the size of IceTop with an energy threshold one order of magnitude lower than the IceTop veto results in an additional detectable astrophysical neutrino rate of the order of one event per year dependent on the spectrum of the flux. Note that the presented IceAct array configuration

with a covered FOV of $0^\circ - 18^\circ$ declination is even larger than IceTop resulting in an additional increase of the detectable astrophysical neutrino flux.

A first IceAct demonstrator is successfully being deployed at the South Pole and is stably measuring in coincidence with IceCube and IceTop cosmic ray air shower signals.

The next IceAct prototype will be deployed in 2017 and have a 61 pixel camera to cover 0.03 sr of the sky for cosmic ray detection and to explore duty cycle and detection efficiency of this telescope technology in situ.

References

- [1] **IceCube** Collaboration, M. G. Aartsen et al., *JINST*, **12** (2017), P03012.
- [2] **IceCube** Collaboration, *PoS (ICRC2017)* 981 (these proceedings).
- [3] **IceCube** Collaboration, *PoS (ICRC2017)* 997 (these proceedings).
- [4] **IceCube** Collaboration, *PoS (ICRC2015)* 1156 (2016), <http://arXiv:1510.05228>.
- [5] **IceCube** Collaboration, *PoS (ICRC2017)* 991 (these proceedings).
- [6] **IceCube** Collaboration, R. Abbasi et al., *Nucl. Inst. Meth. A*, **700** (2013) 188-220.
- [7] **IceCube** Collaboration, *PoS (ICRC2015)* 1064 (2016), <https://arxiv.org/abs/1510.05223>.
- [8] **IceCube** Collaboration, M. G. Aartsen et al., *ApJ* **835** (2017) no.2, 151
- [9] **IceCube-Gen2 Collaboration**, *PoS (ICRC2017)* 1040 (these proceedings).
- [10] **IceCube** Collaboration, *PoS (ICRC2015)* 1070 (2016), <https://arXiv:1508.06296>.
- [11] J. Auffenberg et al., *PoS (ICRC2015)* 1047 (2016), <https://arxiv:1511.01680>.
- [12] The CTA consortium, *PoS (ICRC2015)* 932 (2016), <https://arXiv:1508.06296>.
- [13] D. Lennarz et al., *AIP CP* 1792, 060007 (2017), doi: 10.1063/1.4968990.
- [14] D. Heck, G. Schatz, T. Thouw, J. Knapp, J. N. Capdevielle, *Tech. Rep.* **6019**, FZKA (1998).
- [15] **IceCube** Collaboration, *PoS (ICRC2015)* 1086 (2016), <https://arXiv:1508.06296>.
- [16] **HESS** Collaboration, *Nature* **531** 476 (2016), <http://arXiv:1603.07730v1>.
- [17] **IceCube** Collaboration, *PoS (ICRC2017)* 319 (these proceedings).
- [18] S. Benzvi et. al., *PoS (ICRC2015)* 568 (2016), C15-07-30 Proceedings.

Overview and performance of the D-Egg optical sensor for IceCube-Gen2

The IceCube-Gen2 Collaboration[†], S. Shimizu¹

[†] http://icecube.wisc.edu/collaboration/authors/icrc17_gen2

¹Nippon Marine Enterprise, Yokosuka, Kanagawa 238-0004, Japan

E-mail: aya@hepburn.s.chiba-u.ac.jp

IceCube-Gen2, a future upgrade of the IceCube Neutrino Observatory, is designed to enhance our ability to detect neutrinos above 10 TeV via a significant increase in instrumented volume compared to IceCube. We expect an increased astrophysical neutrino detection rate of up to an order of magnitude with IceCube-Gen2, using a combination of more instrumentation, larger string spacing, and enhanced optical sensor performance. A new optical sensor module, the Dual optical sensor in an Ellipsoid Glass for Gen2 (called "D-Egg"), which houses two 8" HQE photomultiplier tubes (PMTs) in a UV-transparent pressure-resistant glass with an optical coupling elastomer, significantly improves photon detection efficiency in all directions. Its elongated mechanical shape is optimized for cost-effective instrumentation of optical modules and high photon transmittance to PMTs. Furthermore, it is optimized to endure high pressures, as the ice re-freezing period during detector deployment requires the module to withstand pressures up to 70 MPa. Additionally, D-Egg's readout system takes advantage of advances in embedded computing power, enabling simpler, more efficient event triggering and seamless event recording compared to IceCube. Herein, we report on the design and properties of D-Egg's components. A series of laboratory measurements and detailed comparisons with the simulated design indicate that D-Egg provides a technological solution for IceCube-Gen2.

Corresponding Author: A. Ishihara^{*,2}, A. Stoessl² and S. Yoshida²

²Dept. of Physics and Institute for Global Prominent Research, Chiba University, Chiba 263-8522, Japan

35th International Cosmic Ray Conference -ICRC2017-
10-20 July, 2017
Bexco, Busan, Korea

*Speaker.

1. Overview of D-Egg

The IceCube Digital Optical Module (DOM) is a successful, highly reliable optical sensor unit, which has been running for more than 10 years with an extremely small ($\leq 0.5\%$) post-deployment failure rate. The IceCube deep ice array consists of 5160 DOMs and has enabled the observation of rare high-energy neutrino events that consist of TeV–PeV cosmic neutrino fluxes over the the background of atmospheric muons and neutrinos. The next generation experiment, IceCube-Gen2, enhances the system’s effective detection volume, with string separation distances increased by a factor of two and a number of strings comparable to the current IceCube detector; Gen2 also uses the ice 90 m above and 170 m below the IceCube detector. This design presents the significant challenge of achieving improved performance with fewer strings in a given area. The D-Egg optical sensor module was developed to overcome this difficult challenge.

An overview of the D-Egg’s design is presented in Fig. 1. Two 8” Hamamatsu R5912-100 HQE photomultiplier tubes (PMTs) are enclosed in an elongated UV-transparent pressure-resistant housing that is 305 mm in diameter, in contrast with the current DOM, which consists of a single downward-facing 10” Hamamatsu R7081-02 PMT in a spherical housing. The 10% reduction in diameter compared to the IceCube DOM reduces the fuel needed for drilling to a depth of 2620 m by 20%. The shape and material of the D-Egg’s pressure vessel have been carefully designed to optimize Cherenkov photon detection as well as mechanical strength, which is required for stabilization against the maximum pressure of 70 MPa during the hole refreezing period. Minimization of noise expected from the glass material is also investigated. The detection of short-wavelength (UV) photons is important for Cherenkov detectors because the Cherenkov radiation has $1/\lambda$ dependence. The PMTs are optically coupled to the housing glass with a silicone elastomer that also holds the upward- and downward-facing PMTs. The PMT base, called the high-voltage (HV) board, consists of the HV module and PMT signal pulse-shaping circuits and is attached to each

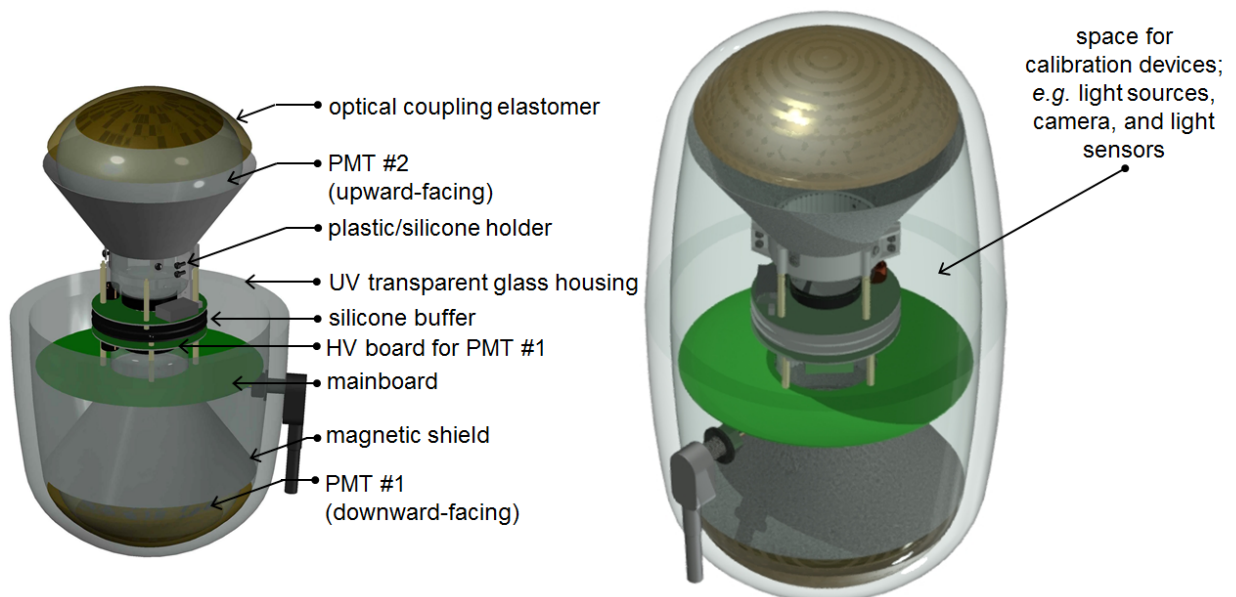


Figure 1: Structural overview of the D-Egg.

PMT. The readout, control, and communication circuits are on the mainboard. The mainboard is placed at the neck of the downward-facing PMT with an internal structure covering the PMT neck, though the mainboard position is adjustable. A silicone buffer structure to connect the lower and upper PMTs is sandwiched between the HV boards. An open space near the upward-facing PMT can be used to install additional calibration devices such as the calibrated light sources [1] or the ice camera [2].

The D-Egg has been developed for increasing effective photocathode area with an upward-facing PMT that also gives an additional directional sensitivity [3], while keeping as much as possible of the successful IceCube DOM design. Other innovative optical sensors are also under investigation for the Gen2 detector, such as the PDOM [4], the MDOM [5] and the WOM [6].

2. Housing

We have determined the optimal glass thickness for photon detection and mechanical strength to be 10 mm for the top and bottom of the glass sphere, where the PMT is sensitive, and 20 mm for the side of the housing, to enhance mechanical strength. A series of pressure tests up to 70 MPa have been performed on the prototype D-Egg glass housing with and without the enclosed PMTs in the high-pressure tank at JAMSTEC¹ in Yokosuka, Japan. We measured the mechanical displacement of the glass under high pressure using three strain gauges (Kyowa KFG Series²) attached to the inside of the housing glass. The experimental results were compared with those from a simulation, as presented in the bottom panel of Fig. 2. The calculated strain ϵ , displacement per unit length, and measured strain show reasonable agreement, except that the measured strain was smaller than the simulated strain by a factor of two near the top of the housing. While this is conservative, we expect the difference to be due to a slight misalignment of the strain gauge, rather than to an inaccuracy in the calculation.

Optical transparency is a key feature of the D-Egg glass. The new glass material was developed by Okamoto Glass³ for high UV light transmittance and low radioactive noise. There is a strong correlation between light transmittance for wavelengths shorter than 400 nm and the Fe content of the glass. Table 1 shows this correlation and indicates that an Fe₂O₃ content of no more than 0.006% by weight is required to achieve the target UV light detection efficiency ($\geq 70\%$ at 320 nm). While the glass batch (the raw materials mixture for glass melting) itself was optimized for low Fe content, when we measured the Fe₂O₃ content after glass construction with an X-ray fluorescence spectrometer (XRF), we found that the Fe₂O₃ content differed for glass samples with different construction methods. We observed an enhancement of Fe content from the batch containing samples indicated as H-3-G1 and H-3-G4 in Table 1. Further study identified that the process involving the use of "cullet", which is broken glass from previous glass production, led to Fe contamination from the older glass and the processes involved in cleaning and storing the cullet. An updated production scheme achieved transmittance of 75% at 10 mm after reflection correction, which is a significant improvement over the IceCube glass, as seen in Fig. 3.

¹Japan Agency for Marine-Earth Science and Technology; <http://www.jamstec.go.jp/e>

²http://www.kyowa-ei.com/eng/product/category/strain_gages/kfg

³<http://www.okamoto-glass.co.jp/eng/>

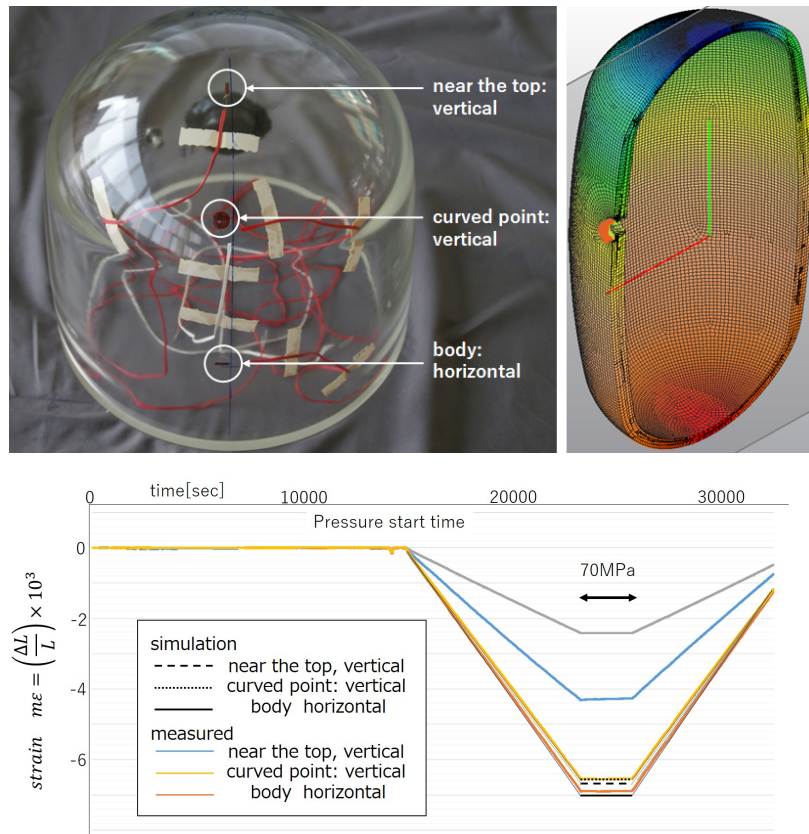


Figure 2: The setup (top, left), vertical displacement simulation (top, right) and strain gauge measurement results (bottom) of glass under 70 MPa pressure.

The PMTs are held and optically coupled by a silicone elastomer to the glass housing. The thickness of the optical coupling elastomer is 5 mm, which is a factor of two reduction compared to that of the IceCube DOM, enabled by matching the glass curvature with the cathode surface curvature of the PMT. In addition to the light transmittance of the elastomer, its hardness is also important, since it must provide good mechanical support for the PMTs while also being soft enough to firmly adhere to the glass. Therefore, two silicone materials were developed for the D-Egg by Shinetsu Silicone⁴ for the best UV transmittance and optimized hardness, as shown in the right panel of Fig. 3 and in Table 2. Both materials exceed a transmittance of 90% at 300 nm, indicating that only a small effect is expected from UV absorption in the elastomer. The IceCube gel referenced in the figure is RTV6136-D1 (General Electric), and later, a similar formulation from Quantum Silicones that has a much softer texture.

The majority of dark noise in the IceCube DOM originates from its glass housing [7]. Cherenkov light from the radioactive decay of K_{40} significantly contributes to the Poissonian noise component as well as to noise from scintillation in the glass. The IceCube glass sphere contains a K_2O concentration of $\approx 0.03\%$ by weight, which roughly corresponds to 100 Bq of beta decays per sphere. With a similar K_2O concentration, the effective noise per PMT can be reduced, because the amount

⁴<http://www.shinetsusilicones.com>

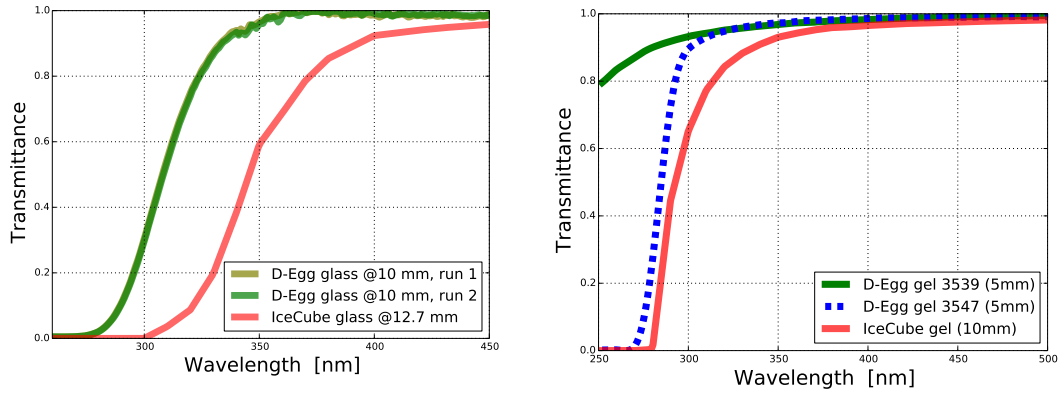


Figure 3: Optical transmittance of the D-Egg housing glass (left) and optical coupling silicone elastomer (right). The glass transmittance was observed as being up to 75% at 320 nm and 40% at 300 nm, a significant improvement over the current IceCube glass.

| Sample (thickness) | Fe ₂ O ₃ by weight [%] | Transmittance at 320 nm [%] |
|-----------------------|---|--------------------------------|
| H-3-G1 (10 mm) | 0.0095 | 61.7 |
| H-3-G4 (10 mm) | 0.0155 | 39.1 |
| DEgg-1705 (10 mm) | 0.0061 | 74.4 |
| IceCube (12.7 mm) | unknown | 10 |

Table 1: The Fe content and transmittance of glass.

| Sample | Hardness | Transmittance at 300 nm [%] | Refractive index |
|--|--------------------------|--------------------------------|------------------|
| X-32-3547 (5 mm) phenylmethyl silicone | Asker C 18 | 91.7 | 1.43 |
| X-32-3539 (5 mm) methyl silicone | Penetration 35 | 95.5 | 1.4 |
| IceCube gel (10 mm) | Penetration \approx 40 | \approx 65 | |

Table 2: The hardness and transmittance of silicone elastomer.

of glass facing each PMT is reduced for the D-Egg, which has thinner glass. However, further reduction is desirable for two-PMT designs to maintain a low power consumption and data rate. In the glass candidate sample H-3-G1, potassium content in the form of K₂O was artificially substituted to reduce the melting temperature and speed up the glass melting process. The newly developed D-Egg glass, DEgg-1705, replaces K₂O with Na₂O to reduce radioactive noise from K₄₀. The K₂O fraction by weight of the DEgg-1705 was measured as $0.0135 \pm 0.0023\%$ via XRF, which corresponds to a reduction greater than a factor of two compared to the IceCube glass. XRF also found no scintillation candidate materials, such as a cerium-containing compound. The batch of DEgg-1705 glass was also investigated by using a germanium semiconductor gamma-ray spectrometer (GSGS) for possible contamination by gamma-ray-emitting radioactive material. The GSGS observed a rate of gamma rays from K₄₀ which correspond to 0.74 ± 0.09 Bq/kg. While the near-PMT surface thickness is reduced, the glass material is enhanced on the side of the sphere. A more precise estimate of the dark rate of PMTs due to radioactive material in the glass and from the other effect will require improved and detailed GEANT4 simulation and lab measurement.

| Sample | K ₂ O by weight [%] | Radioactivity [Bq/kg] | Linear expansion coefficient | Refractive index |
|--------------------|-----------------------------------|--------------------------|---------------------------------|------------------|
| H-3-G1 | 0.73 | 166.4 | 54.23×10^{-7} | 1.49 |
| DEgg-1705 | 0.0135 ± 0.0023 | 0.74 ± 0.09 | 53.98×10^{-7} | |
| IceCube (ref. [7]) | ≈ 0.03 | ≈ 10 | unknown | |

Table 3: The potassium content, gamma-ray emitting radioactivity, expansion coefficient, and refractive index of different glass samples.

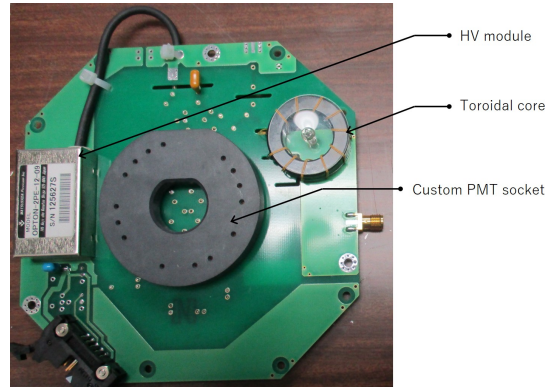


Figure 4: PMT socket with HV board.

3. HV module

We developed an HV board for the D-Egg with a divider circuit for the PMT and pulse-shaping and signal-coupling circuits from the cathode-grounded PMT signal using the Matsusada OPTON-2PE-12-09 HV module. The stability and characteristics of ripple in the level of 2 mV_{pp} of the HV module were found to be satisfactory. Signal coupling from the PMT DC voltage is achieved using a transformer circuit, as in the IceCube DOM, with a TDK H5C2T31x8x19 toroidal core. A prototype HV base is shown in Fig. 4. The custom PMT space-saving socket enables us to install the HV board to the PMT easily, though in the final design the part may be replaced by direct soldering for cost efficiency.

4. Magnetic shield

The performance of the PMT is influenced by a local magnetic field such as that of the Earth. The impact of this effect can be reduced by shielding the PMT with high-permeability materials. There are two options for magnetic shielding for the D-Egg module. One consists of a cage made with mu-metal wires around the photocathode surface PMT, designed similarly to that of the IceCube DOM. The other is made with FineMet™ foil, which can be wrapped in a conical shape around the PMT neck, similar to that of the Daya Bay experiment optical sensor [8], as shown in the left panels of Fig.5. The performance of each shield was examined by applying a homogeneous magnetic field to a direction perpendicular to the central axis of the PMT. A bare PMT was illuminated by 380 nm laser picosecond pulser (Hamamatsu)⁵. The detection efficiency μ (which

⁵<https://www.hamamatsu.com/jp/en/product/category/1001/5003/M10306-27/index.html>

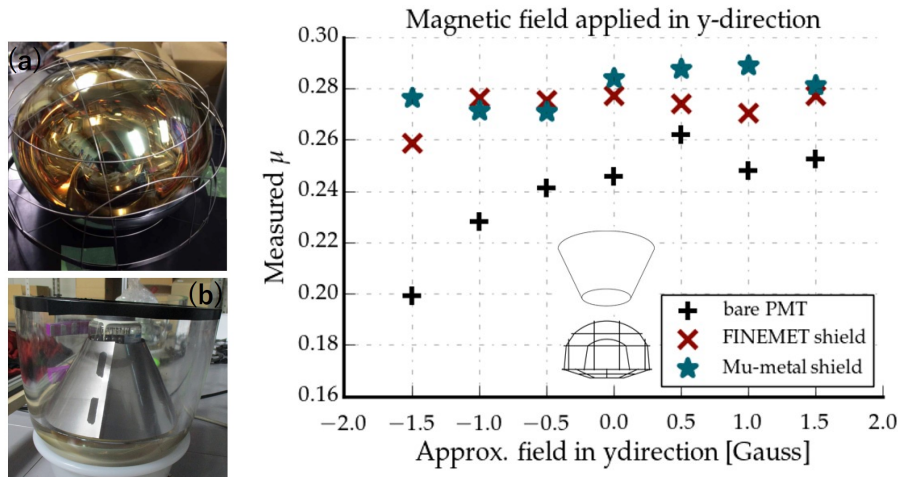


Figure 5: Magnetic shields. Left: (top) mu-metal cage, (bottom) FineMet cone. Right: The light detection efficiency parameter μ as function of the applied magnetic field.

is proportional to the collection efficiency, quantum efficiency, and light intensity) was measured as a function of the applied magnetic field, as shown in the right panel in Fig. 5. Due to its cost effectiveness and ease of integration, the conical shield is currently considered the default option, although low-temperature performance tests must still be performed.

5. Data Acquisition and control System

The readout and communication between surface control units and deep ice optical modules are on a circuit board called the mainboard. The mainboard design is similar to that of the PDOM [4], except for the additional digitizer for the signal from the second PMT. The system architecture of the D-Egg is shown in Fig. 6. The requirements for deep-ice neutrino detection are a power consumption of ≤ 4 W per module, wide dynamic range from 0.1 of a single photo-electron (PE) signal to more than a thousand PEs, ns-level timing accuracy for PMT pulses, and data transmission rates of greater than 1 Mbps. Furthermore, once an optical module is installed in the South Pole glacial ice, it cannot be replaced. Therefore, long-term reliability is one of our highest design priorities. In this contribution, the default design is shown, though the system is still being optimized. The cathode-grounded PMT current signal on the DC high voltage for each PMT is read out through a separate analog front-end that shapes the signal. The shaped signal is digitized by an ADS4149, 14-bit, 250-MSPS ADC with 265 mW of total power for each PMT. Digital processing is performed in a field-programmable gate array (FPGA). A single FPGA (Cyclone V 5CEFA7F23C7N) takes the continuously digitized waveforms from two digitizers and applies flexible triggering, such as a voltage threshold or local coincidence between the signal from two PMTs. The mainboard also contains the HV control system with 8-bit digital-to-analog converter (DAC) and communication hardware to interface to the communication card on the surface counting house, including timing calibration and power management.

6. Summary

All necessary components of the D-Egg IceCube-Gen2 optical module have been designed,

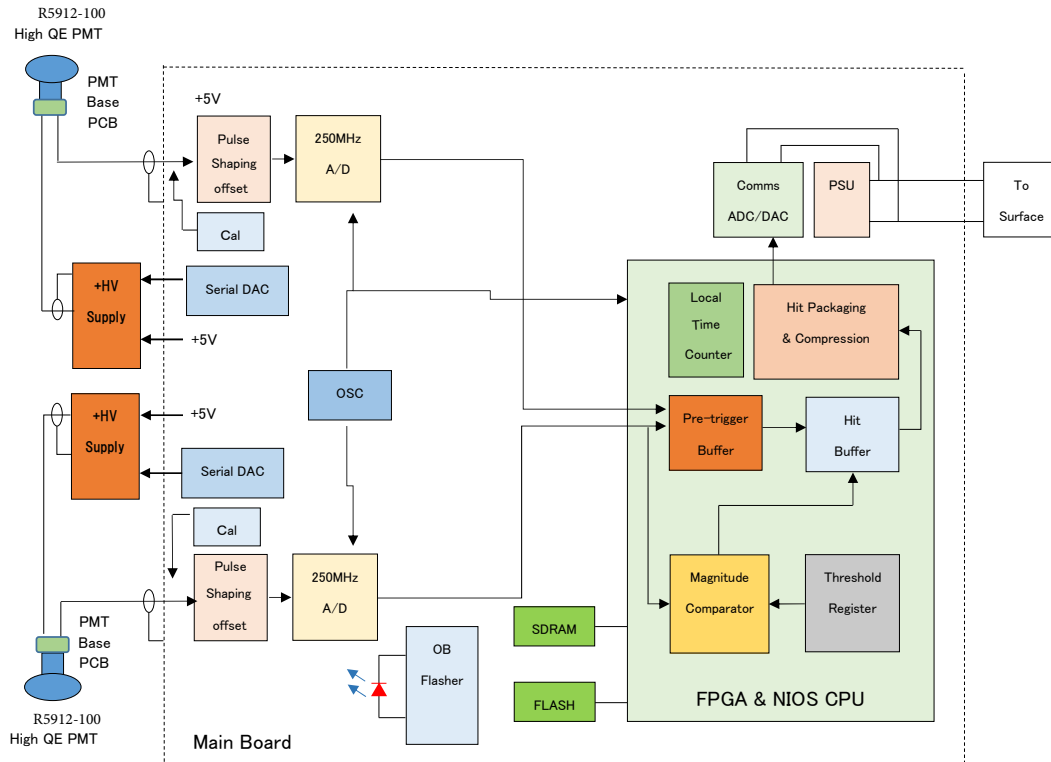


Figure 6: Mainboard block diagram. This low power consumption mainboard is responsible for readout and digitization of PMT signals, communication with surface control units, monitoring and calibration. Two digitizers, one for each PMT, continuously digitize waveform signals from PMTs, to be processed in an on-board FPGA.

and the second batch of prototype modules is being produced. D-Egg's elongated shape and upward-facing PMTs are new to IceCube, and its cost-effective construction of a deep-ice array of optical sensors establishes good angular resolution for all directions currently being studied [3]. While maintaining the successful design architecture of the IceCube DOM, D-Egg has successfully improved upon several of its major components.

References

- [1] IceCube-Gen2 Collaboration, [PoS \(ICRC2017\) 934](#) (these proceedings).
- [2] IceCube-Gen2 Collaboration, [PoS \(ICRC2017\) 1040](#) (these proceedings).
- [3] IceCube-Gen2 Collaboration, [PoS \(ICRC2017\) 1038](#) (these proceedings).
- [4] IceCube-Gen2 Collaboration, [PoS \(ICRC2015\) 1148](#) (2015); P. Sandstrom and IceCube-PINGU Collaboration, *AIP Conference Proceedings* 1630, 180 (2014) (<http://doi.org/10.1063/1.4902801>).
- [5] IceCube-Gen2 Collaboration, [PoS \(ICRC2017\) 1047](#) (these proceedings).
- [6] IceCube-Gen2 Collaboration, [PoS \(ICRC2017\) 1052](#) (these proceedings).
- [7] IceCube Collaboration, M. G. Aartsen et al., *JINST* **12** (2017) P03012.
- [8] P. DeVore *et al.*, *Nucl. Instr. and Meth. A* **737** (2014) 222.

Muon track reconstruction and veto performance with D-Egg sensor for IceCube-Gen2

The IceCube Gen2 Collaboration

http://icecube.wisc.edu/collaboration/authors/icrc17_gen2

E-mail: achim.stoessl@icecube.wisc.edu

The planned extension of IceCube, IceCube-Gen2, a cubic-kilometer sized neutrino observatory, aims at increasing the rate of observed astrophysical neutrinos by up to a factor of 10. The discovery of a high energy neutrino point source is one of its primary science goals. Improving the sensitivity of the individual modules is a necessity to achieve the desired design goal of IceCube-Gen2. A way of improving their sensitivity is the increase of photocathode area. The proposed module called the D-Egg will utilize two 8" Hamamatsu R5912-100 photomultiplier tubes (PMTs), with one facing upwards and one downwards. These PMTs have an increased quantum efficiency and their sensitivity is comparable to the 10" PMT used by IceCube. This essentially leads to an increase in sensitivity by almost a factor of 2 with a full 4π solid angle acceptance. A simulation study is presented that indicates improvement in angular resolution using current muon reconstruction techniques due to the new sensor design. Since the proposed module is equipped with an upward facing PMT, further emphasis will be set on the development of new reconstruction techniques that exploit this geometry, as well as an improvement of veto probability for incoming muon tracks, which is crucial for neutrino astronomy in the Southern sky.

Corresponding author: A. Stoessl^{*1}

¹*International Center for Hadron Astrophysics, Graduate School of Science, Chiba University 1-33, Yayoi-cho, Inage-ku, Chiba-shi, Chiba, 263-8522 Japan*

*35th International Cosmic Ray Conference — ICRC2017
10–20 July, 2017
Bexco, Busan, Korea*

*Speaker.

1. IceCube Gen2

The IceCube neutrino observatory at the geographic South Pole is a cubic kilometer array of photosensors which is able to detect the faint Cherenkov light produced by secondaries from interactions of neutrinos with the glacial ice [1]. So far, the experiment has yielded a plethora of science results, among them the discovery of a neutrino flux most likely of extraterrestrial origin [2]. After 6 years of data-taking, with the completed detector, a precise measurement of the extraterrestrial neutrino flux is still limited by statistics. To overcome the statistical limitations and to improve the effective area for neutrino events in the energy regime beyond 10 PeV as well as the point source sensitivity, an extension of the IceCube array has been proposed [3]. The proposed geometry for IceCube-Gen2 considered in this work is shown in Figure 1. The geometry shows a larger extension in the x-y plane than in depth. It is optimized for the reconstruction of horizontal muon tracks, since these have the highest contribution to the point-source sensitivity [4].

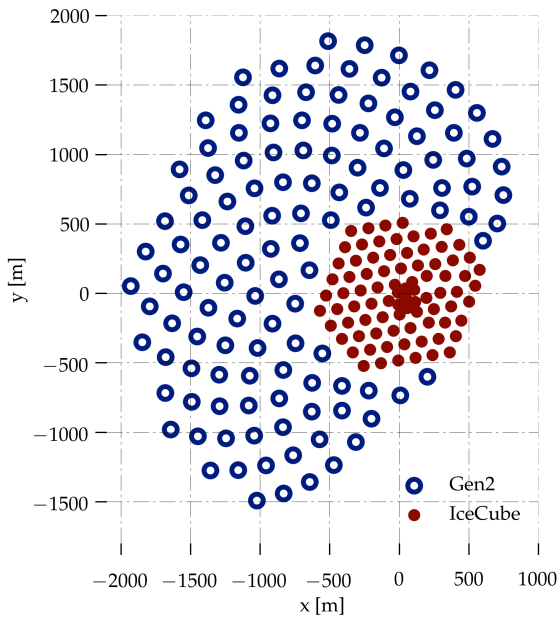


Figure 1: A proposed geometry for IceCube-Gen2 which is used for this study. In addition to the 86 strings of IceCube, which can be seen as the hexagonal shape marked with the red dots, 120 new strings with each 80 sensors are arranged in a complex grid geometry to optimize the veto power for incoming muon tracks. The average distance between the new strings is about 240 m with a vertical spacing between individual sensors of 17 m. The extension of IceCube to larger positive x-values is prohibited due to the runway of the South Pole Station.

2. The D-Egg sensor for Gen2

Several different sensor designs for IceCube-Gen2 are under investigation. However relevant for this study are the following two proposed designs:

- ▶ The PDOM [5], which is basically the same design as the IceCube optical sensor [6], however with a PMT with a higher quantum efficiency. It features a single 10" PMT which is facing downwards and a improved readout.
- ▶ The D-Egg [7], which follows the design of the PDOM, however includes another PMT facing upwards. The PMTs are 8", so the total diameter of the D-Egg is slightly smaller than the PDOM and it has about 1.48 more photocathode area than the PDOM for a Cherenkov weighted spectrum.

Due to high drill costs at the South Pole, it is desirable to deploy sensors with a large photocathode area to keep the cost for the average cm^2 photocathode as low as possible. The high drill costs can be reduced by drilling holes with a smaller diameter. As the diameter of the D-Egg is 10% smaller than the diameter of the PDOM, about 20% of the fuel cost can be saved during deployment. A graphic of the D-Egg with its dimensions is shown in Figure 2. The two Hamamatsu R5912-100 high quantum efficiency PMTs are enclosed in a highly transparent glass housing, which is optimized for transparency in the near ultraviolet. The high voltage for the PMTs is generated on two boards, and the final design will feature a board for readout electronics as well. In this proceeding, we investigate the performance of the D-Egg using several existing reconstruction methods developed for IceCube and compare the results against the benchmark PDOM performance.

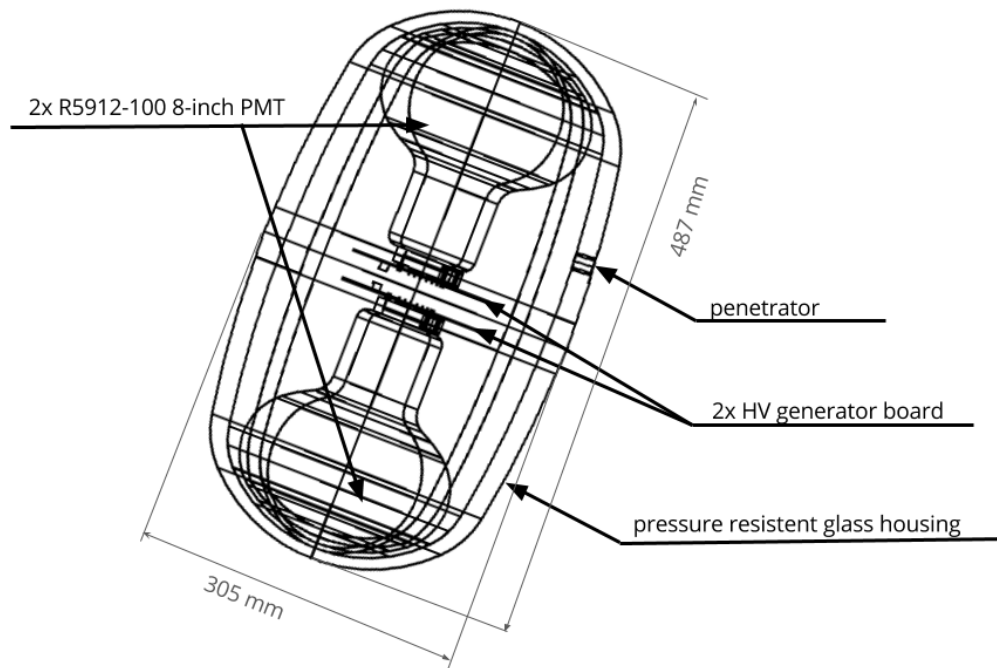


Figure 2: A schematic of the D-Egg design. It features two 8" PMTs enclosed in a highly transparent glass housing. Its diameter is 10% smaller than that of the current IceCube optical module.

3. Simulation

We simulated muons from an $E^{-1.4}$ power-law spectrum in the energy range of 10 TeV to 10 PeV with a full 4π angular distribution. The muons were injected at a cylindrical surface enclosing the detector and then propagated through the ice. The light emerging by stochastic energy losses of the muons as well as the smooth Cherenkov light were simulated and the photon propagation is handled by the direct propagation code developed for IceCube. The simulation features a bulk ice model which means that the ice is homogenous throughout the detector. As the direct propagation of photons is computationally consumptive, the detector simulation for D-Egg and PDOM are sharing the same photon simulation as input, which means that the photons have been simulated once and then the simulation branches into the different types of detector simulation. To further

increase the simulation efficiency, several simplifications were made. The effects of glass and gel and the module geometry are not simulated individually. Instead the photons are weighted with the angular sensitivity of the module as well as the wavelength dependent quantum efficiency. The efficiency of the photocathode is assumed to be constant over the whole area. To further increase the efficiency of the simulation, the size of the modules is scaled up and the number of propagated photons is decreased accordingly.

The noise introduced by the PMT and the glass housing is simulated in the same way for D-Egg and PDOM, however with absolute values scaled by the photocathode area. Further simplifications are made in the PMT and sensor simulation. The PMT simulation is done as for the PMT used in IceCube, as they are very similar in their behavior. The benefit of this is that the same simulation chain can be used for D-Egg as well as for the IceCube DOM and PDOM. As the readout electronics for the D-Egg is not yet finalized, we assume a perfect readout with an infinitesimal small binning in time. The IceCube array, as part of IceCube-Gen2 has been simulated to our best knowledge.

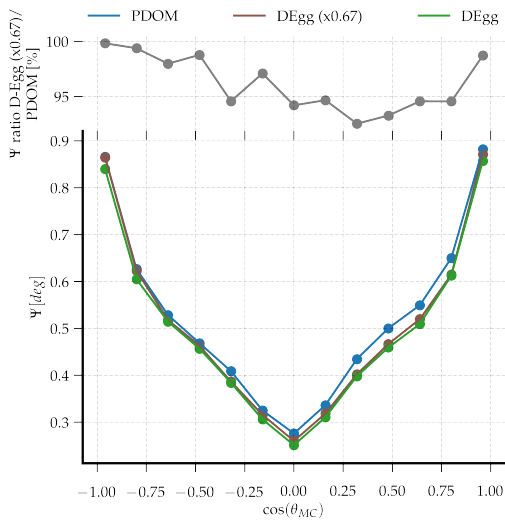


Figure 3: The results of the SPEFit reconstruction for both sensors, D-Egg and PDOM binned in the cosine of the simulated muon direction. The D-Egg effective area is scaled down by a factor of 0.67 to match the PDOM effective area. Muons with a cosine of -1 are entering the detector from below, those with 1 from above respectively.

4. Muon reconstruction

The simulated dataset was reconstructed with a set of algorithms. In this study we focus on the reconstruction algorithms SPEFIT and SPLINE-RECO [8]. The algorithms operate on the reconstructed pulses, each using a different method. While SPEFIT uses a simple analytical ice-model and a likelihood with one term per optical module, where only the first registered pulse is considered, SPLINE-RECO is capable of constructing a likelihood with a probability density function (pdf) obtained from tabulated values, and thus is able to also include more complicated models for the glacial ice. To compare the accuracy of the reconstruction results, we looked at the distributions of the opening angle Ψ between the simulated and reconstructed track. The median of this distribution is used as a figure of merit. No quality cuts have been applied, yet we restrict ourself to tracks which traverse the instrumented volume.

We aim to investigate the impact of the increased photocathode area and segmentation on the reconstruction independently. As such, we work with different types of D-Egg simulation:

- ▶ Simulation of the D-Egg “as is” as described in section 3.
- ▶ The same as above, however the effective photocathode area is scaled down by a factor of 0.67 to match the photocathode area of the PDOM
- ▶ Simulation of the D-Egg where either the upward or downward facing PMT is disabled.

All types of simulations share the same simulated photons, but then branch in different detector simulations. First, the behavior of the two individual PMTs is studied. As the simulation has up-down symmetry, we expect the same performance for the datasets with only pulses in the upper or lower PMT. The results for the SPEFIT reconstructions is shown in Figure 3. All reconstructions perform best for more horizontal events due to the fact that the Gen2 geometry is elongated more in the x and y dimension than in the z dimension. This means that horizontal tracks cross a larger instrumented volume. Also as the string spacing is 240 m, vertical tracks have a lower light yield if they enter the detector in between strings. For upward-going muons, if only the lower PMT of D-Egg is used as reconstruction input, it can be seen that the performance is slightly better than for the upper PMT only, and vice versa for downward going muons. The SPEFIT reconstruction yields a higher accuracy for the D-Egg sensor, which we quantify to be about 5% in the horizontal and downward region due to the segmentation of the D-Egg only as we here compare to the scaled-down version. We attribute this to the fact that SPEFIT uses only the first pulse recorded by each PMT, and the doubling of PMT thus increases the number of pulses available to the reconstruction, especially for the downward region.

The performance SPLINE-RECO of the reconstruction is shown in Figure 4. The D-Egg exhibits up to 15% higher accuracy in reconstruction especially in the horizontal region, which is important to point source searches [4]. The reconstruction in the downward going region yields more accurate results with D-Egg as well. Comparing the results as a function of the true muon energy E_{MC} as it is shown in the right panel of Figure 4, the SPLINE-RECO reconstruction gains for D-Egg due to the higher photoelectron (PE) yield. However it seems that most of the gain results from the larger photocathode area of D-Egg.

5. Likelihood improvements for segmented sensors

Figure 4 shows that the increase in reconstruction performance for the D-Egg seems to be attributed mostly to its larger total photocathode area. Thus, we investigate the details of the SPLINE-RECO reconstruction. Developed for IceCube, the here used likelihood is not optimized for segmented sensors, and thus it does not exploit their full potential. The likelihood is given by [8]:

$$L = \prod_{j=1}^{N_{DOM}} N \cdot p_j(t_j) \cdot (1 - P_j(t_1))^{N-1} \quad (1)$$

In the above equation, N stands for the number of hits on a certain optical module, p_j and P_j are the time residual pdf and cumulative density function for the hit DOM and t_j is the time of the first hit of the given DOM. Contours of this likelihood function can be seen in Figure 5. This simplified example illustrates the likelihood space for a single module, placed in the middle of the individual figures. A muon track crosses the plane of the figure orthogonal in 120 m distance. In

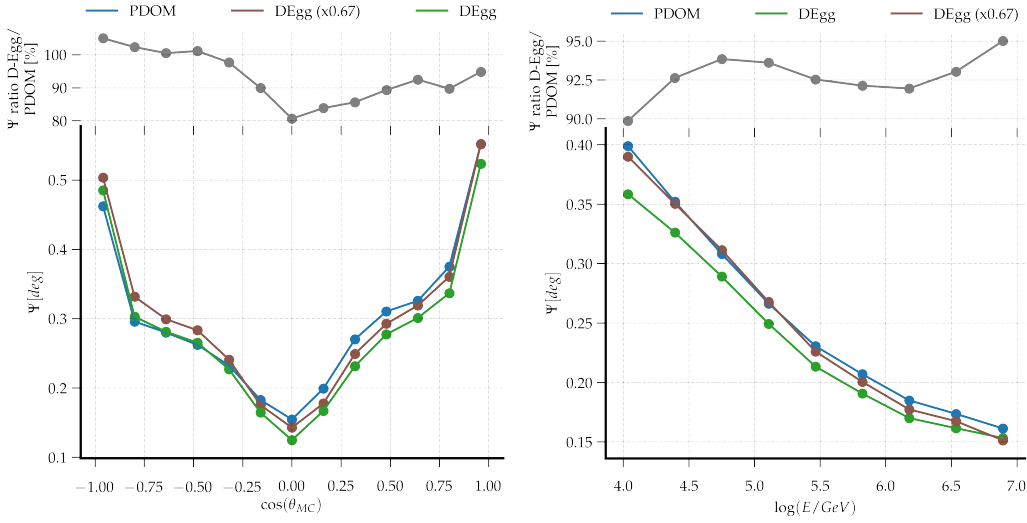


Figure 4: The results of the reconstruction SPLINE-RECO, binned in the cosine of the simulated muon direction on the left and binned in the logarithm of the muon energy on the right. Muons with a cosine of -1 are entering the detector from below, those with 1 from above respectively.

this example, the sensor detects 20 photo electrons with arrival times given by the time residual pdf. The 1σ contour for the likelihood developed for the IceCube DOM is shown with the two circles with the red color. As it can be seen, the direction of the individual PMT imposes only very small constraints on the red likelihood contour. As a reason, we suspect the importance of the late photo electrons in the arrival time distribution. In the current approach, the likelihood is constructed by the use of the timing of the first photo electron and the number of total hits, but does not account for the timing of later photo electrons. Extending equation 1 to include the arrival times of all photo electrons can improve the likelihood. This new likelihood is illustrated in the example in Figure 5 with the blue contours. It allows for a more precise determination of the track position, which in total will most likely lead to a better angular resolution of the overall reconstruction algorithm. The IceCube-Gen2 collaboration is currently working on a reconstruction implementing this approach.

6. Veto performance

An effective method to select an all flavor neutrino sample with high purity and full sky acceptance is the implementation of a veto: Using the outer strings and top and bottom layer of optical modules, incoming muon tracks can be tagged and removed from such a sample. The method has been proven successful and lead to the discovery of the extraterrestrial neutrino flux [2]. The method has been applied and studied for IceCube-Gen2 [9]. In the context of this proceedings we are investigating the impact of D-Egg on the efficiency of the veto algorithm. An important parameter of the current algorithm is the veto threshold, which is the charge required in the veto region to trigger the veto, which is currently set to 3 PEs. Since the D-Egg has an upward facing PMT, we expect a higher performance for downward going cosmic ray muon tracks. Due to the D-Eggs larger photo cathode, we also expect a higher probability to detect charge in the veto region

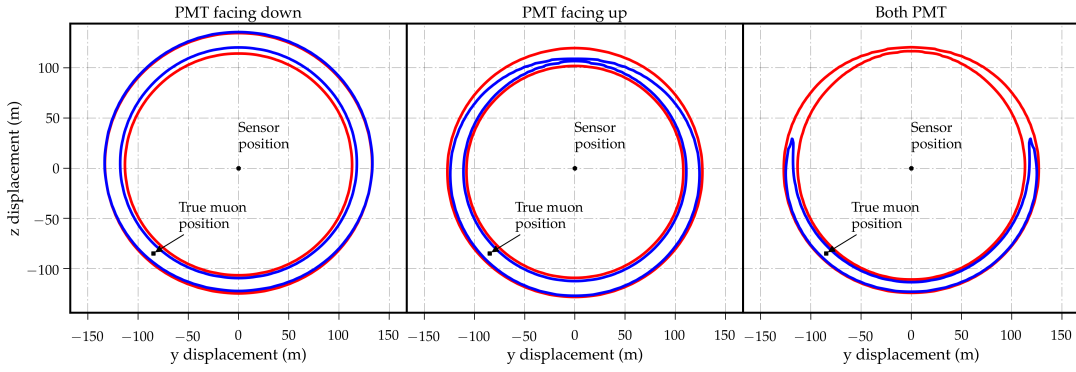


Figure 5: Likelihood contours of two different likelihoods for a single D-Egg sensor in case of a muon traversing the plane in orthogonal direction. The red contour results from the likelihood used in SPLINE-RECO, the blue contour is a proposed likelihood considering the timing of the late pulses in the arrival time distribution. On the left, the contours are shown for the lower PMT only. The contours are based on an Asimov sample. The middle plot shows the situation for the upper PMT and on the right the combined contours of both PMTs are shown.

at all. This is illustrated in Figure 6: The distribution of collected charge for the upper 2 layers of modules of the IceCube-Gen2 geometry results in a higher probability to veto incoming muons. Further impact of the use of D-Eggs in the veto region is currently under investigation.

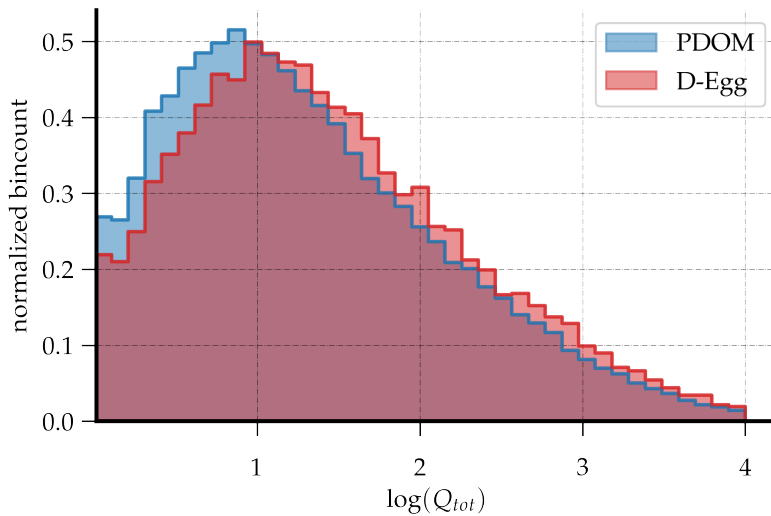


Figure 6: The collected charge in the upper layer of the IceCube-Gen2 array. The collected charge is shown for the uppermost 2 layers of optical modules.

7. Summary

For the first time, we present a study of muon track angular resolutions with current reconstruction techniques used by IceCube for the proposed extension IceCube-Gen2. We compare a new sensor design, the D-Egg, to an improved sensor based on the current IceCube design (PDOM). The angular resolution for common reconstruction algorithms in IceCube were studied for both sensors with a full-sky muon simulation and we find an improvement of the angular resolution of

D-Egg of about 20% compared to PDOM. The major part of the improvement can be attributed to the larger photo cathode area of D-Egg. Investigating the fact that segmentation of the sensors seems to have only a small impact on the reconstruction result, we find that there are no existing reconstruction methods that fully take advantage of the module segmentation. Efforts are ongoing to develop a reconstruction that more accurately incorporates late photon timing information, and thus exploits all of the information provided by the D-Egg module. Besides the improvement in angular resolution, we show that the veto performance for the current implementation of the IceCube veto can be improved by using D-Eggs as well. We studied the deposited charge in the upper layer of the IceCube-Gen2 array and find a significant increase in the low charge region around the 3 PE threshold. In conclusion, we find that we are on a good track to improve the current IceCube reconstruction and veto techniques to exploit the full potential of new approaches in sensor design for IceCube-Gen2 and encourage further, more detailed studies to follow.

References

- [1] **IceCube** Collaboration, Aartsen et al., *JINST* **12** (2017), P03012
- [2] **IceCube** Collaboration, M.G. Aartsen et. al., *SCI* **342(6161)** (2006) P1242856.
- [3] **IceCube** Collaboration, M. G. Aartsen et al., *astro-ph/1412.5106* (2014).
- [4] **IceCube-Gen2** Collaboration, [PoS \(ICRC2017\) 991](#) (these proceedings).
- [5] **IceCube-PINGU** Collaboration, P. Sandstrom, *AIP* **1630(1)** (2014) P180-183.
- [6] K. Hanson and O. Tarasova, *NIM* **567(1)** (2006) P214-217
- [7] **IceCube-Gen2** Collaboration, [PoS \(ICRC2017\) 1051](#) (these proceedings).
- [8] **AMANDA** Collaboration, J. Ahrens et al., *NIMA***524** (2004) P169-194.
- [9] **IceCube-Gen2** Collaboration, [PoS \(ICRC2017\) 945](#) (these proceedings).

In-ice self-veto techniques for IceCube-Gen2

The IceCube-Gen2 Collaboration[†]

[†] http://icecube.wisc.edu/collaboration/authors/icrc17_gen2

E-mail: jan.lunemann@vub.ac.be

The discovery of astrophysical high-energy neutrinos with IceCube opened the window to neutrino astronomy. With the IceCube-Gen2 high-energy array, an extension that will surround the existing IceCube deep ice detector, the detection rate of cosmic neutrinos will be increased by about an order of magnitude.

The main background of neutrino telescopes such as IceCube consists of muons that are produced by cosmic-ray particles in the atmosphere. A successful method to distinguish neutrinos from this background selects only events that start inside the detector. This can be accomplished by defining a veto layer in the outer region of the detector and considering the amount and timing of Cherenkov light detected in this region.

For the IceCube-Gen2 high-energy array the definition of the veto has to be optimized and new techniques will be introduced, as the geometry will be different and the distances between the optical modules will be larger than in IceCube. In this contribution we present the results of a data-driven analysis that uses real IceCube data to estimate the expected veto energy threshold. In addition, a new veto technique has been developed with the aim of lowering the energy threshold of the current veto procedure. A study of the veto efficiency for different detector geometries of IceCube-Gen2 will be presented as well.

Corresponding authors: P. Coppin¹, S. Toscano¹ **Speaker:** J. Lünemann^{*1}

¹ *Vrije Universiteit Brussel*

*35th International Cosmic Ray Conference - ICRC2017-
10-20 July, 2017
Bexco, Busan, Korea*

*Speaker.

2 1. Introduction

3 The IceCube neutrino telescope is the first detector that successfully identified a flux of high-
4 energetic astrophysical neutrinos. However, the statistics are limited, and it has not yet been possible
5 to identify the sources of these neutrinos. To obtain more astrophysical neutrinos, a major
6 upgrade, IceCube-Gen2, is in planning, that will increase the detection volume by an order of
7 magnitude [1]. The main background for neutrino telescopes are muons produced by cosmic ray
8 showers in the atmosphere. An effective method for the reduction of this background is the application
9 of a veto against incoming tracks. This can be done by the installation of surface veto
10 hardware like air shower arrays or air cherenkov telescopes. Another approach that does not depend
11 on additional hardware for an alternative detection technique is the application of self-veto
12 algorithms, which has been successfully done for IceCube. Transferring these filters to a detector
13 that is less densely instrumented and bigger, will influence the performance of the veto. Therefore,
14 the algorithms have to be adapted to the expanded geometry. In addition, new developments can
15 increase the veto power.

16 2. IceCube-Gen2

17 IceCube is a cubic-kilometer neutrino detector installed in the ice at the geographic South Pole
18 [2] between depths of 1450 m and 2450 m, completed in 2010. The reconstruction of neutrino direction,
19 energy and flavor relies on the optical detection of Cherenkov radiation emitted by charged
20 particles produced in the interactions of neutrinos in the surrounding ice or the nearby bedrock.
21 A large number of results obtained using the IceCube detector (e.g.[3, 4, 5, 6]) have proven the
22 scientific value of a Cherenkov neutrino telescope in the Antarctic ice sheet. However, the energy
23 range and the event rate is limited by IceCube's current configuration and volume. To obtain a
24 higher rate of events, an upgrade to the existing detector is in its planning phase (see Figure 1).
25 One part of this upgrade is the extension of the current in-ice geometry by adding strings around
26 the existing detector. The volume of this high-energy extension will be a factor of ten higher than
27 the current detector, so the rate of high-energy neutrino events will increase by an order of magnitude.
28 The goal is to obtain a much larger sample of events in order to investigate the sources of the
29 high-energy neutrinos observed by the IceCube detector.

30 In the current planning, 120 new strings will be added around the existing configuration (IC86).
31 Three layouts are under consideration, called sunflower, edge-weighted and banana geometry (see
32 Figure 2). For the edge-weighted geometry, the string spacing is 240 meters for the inner strings and
33 125 meters for the outer strings. For the banana geometry, strings are separated by 235 meters. For
34 the sunflower geometry, three different string spacings (200, 240 and 300 meters) are considered.

35 In contrast to IC86, the proposed geometries are not arranged in a hexagonal grid. Instead,
36 a spiral geometry was chosen. This will improve the directional reconstruction of tracks, as no
37 azimuthal directions will be preferred by certain planes in the grid. The most important difference
38 between the current IceCube configuration and Gen2 is the increased string spacing, ranging from
39 200 to 300 meter, which decreases the total amount of light that will be received in each event. This
40 will influence not only the resolution on reconstructed energy and direction, but also the efficiency
41 of filters to select events which start inside the detector. The new strings are planned to carry 80

42 DOMs each, 20 more than the existing strings. Six of the additional DOMs will be placed above
 43 and 14 below the region covered by IC86.

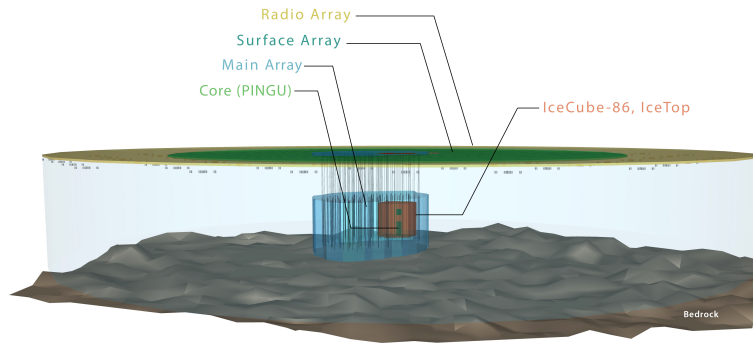


Figure 1: Schematic view of IceCube-Gen2. The detector includes the main array and densely instrumented core, as well as a large surface array and an array of radio detectors.

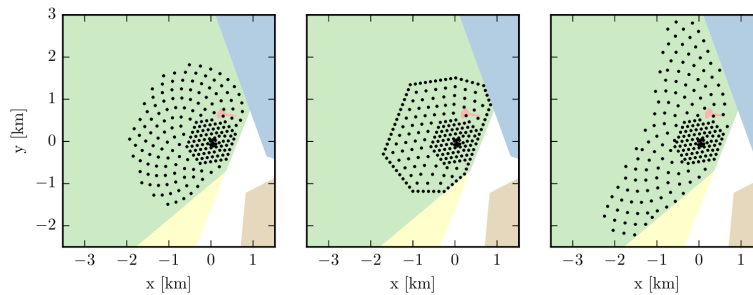


Figure 2: Different layouts for the high-energy in-ice extension. Left: sunflower geometry, center: edge-weighted geometry, right: banana geometry

44 3. The HESE filter

45 The trigger rate of IceCube is about 2.5 kHz. Of these events, only few per year can be
 46 identified as astrophysical neutrinos. The observation of a cosmic neutrino flux requires effective
 47 filters that select most of the signal events while removing a large fraction of the background. In
 48 IceCube this has been achieved in the High-Energy Starting Event (HESE) analysis [3]. The HESE
 49 filter was designed to identify high-energy events with an interaction vertex inside the detector
 50 volume. This way only neutrinos will be selected, as incoming muons will emit light while entering
 51 the detector. If the first light of an event is recorded at the edge of the detector, the filter rejects this
 52 event, producing a neutrino sample of high purity.

53 For the HESE filter a certain part of the detector is defined as a veto region. Figure 3 shows the
 54 IceCube detector with the veto region indicated by a grey band. A layer of 90 meters at the top of
 55 the detector is included to classify down-going atmospheric muons. To identify muons entering the
 56 side of the detector, the strings at the edge of the detector are also included. At the depth of 2000 m
 57 - 2100 m, the scattering and absorption lengths of light are significantly decreased due to a dust
 58 layer in the ice [7]. As muons could enter the detector undetected here, the DOMs in the bottom of

59 this region are also included in the veto layer. Additionally, DOMs in the bottom 10 meters of the
60 detector are included.

61 The following procedure is applied to identify starting events. The earliest possible time win-
62 dows of $3\mu\text{s}$ is selected that includes at least 250 photo electrons (pe). If during this time window,
63 the number of hits N inside the veto layer is larger than three, or the total charge Q of these hits
64 exceeds 3 pe, the event is tagged as an incoming track. As low-energy background muons can pass
65 the veto layer while depositing less than three hits, an overall charge threshold $Q_{tot} > 6000$ pe is
66 applied. Low-energy muons passing very close to one of the DOMs can deposit a very high charge
67 and thus surpass the threshold. To avoid these balloon events from falsely entering the selection,
68 DOMs are excluded from the calculation of the total charge if they contribute more than 50% of
69 the total charge.

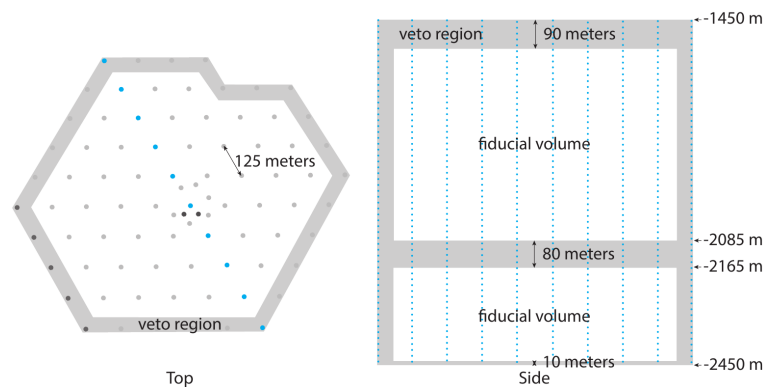


Figure 3: Top and side view of the IceCube detector. The veto region for the HESE veto is indicated as a gray area.

70 4. Performance of the HESE veto for Gen2

71 The HESE filter was designed and optimized for the dimensions and layout of IceCube. How
72 the filter performs for a different geometry is a question that has to be addressed. One approach
73 would be to use full simulations of the proposed detector layouts. However, the simulation of
74 enough statistics for each geometry is computationally expensive. Another disadvantage is that
75 systematic uncertainties will be included in the simulation.

76 Instead, a data-driven approach has been investigated in order to evaluate the passing rate for
77 a detector with a string spacing of Gen2. To do that, one year of data taken by IC86 was processed
78 as described in the following. First, IceCube strings are removed from the geometry in order to
79 mimic the wider string spacing (250m) of Gen2. The geometry before and after the removal of the
80 strings is shown in Figure 4.

81 Data from 2011 were used for this analysis. Before any string removal, the veto is applied for
82 the full detector in order to select the events. Only events crossing the veto region are included, so
83 that the sample consists of entering tracks only. After this, strings are removed from the geometry
84 according to the new geometry and the veto is applied the same way as for the full detector.

85 Figure 5 displays the passing number as a function of the total charge deposited in IC86,
86 which is a variable highly correlated to the energy. The blue points represent all the entering tracks

87 in the sample and the green squares show the passing events in the sparse (250 m) detector. For
 88 comparison, the rate of passing events for the full detector are shown as red triangles. This was
 89 calculated by defining a second veto layer at the edge of the fiducial volume and counting the
 90 incoming events that are not rejected by the second veto. The dashed lines are the exponential fit
 91 to the data.

92 This study implies that applying the veto in the current configuration to a detector with in-
 93 creased string spacing will lead to an energy threshold (20000 pe) that is a factor of 3 higher
 94 compared to the corresponding threshold for IceCube (6000 pe).

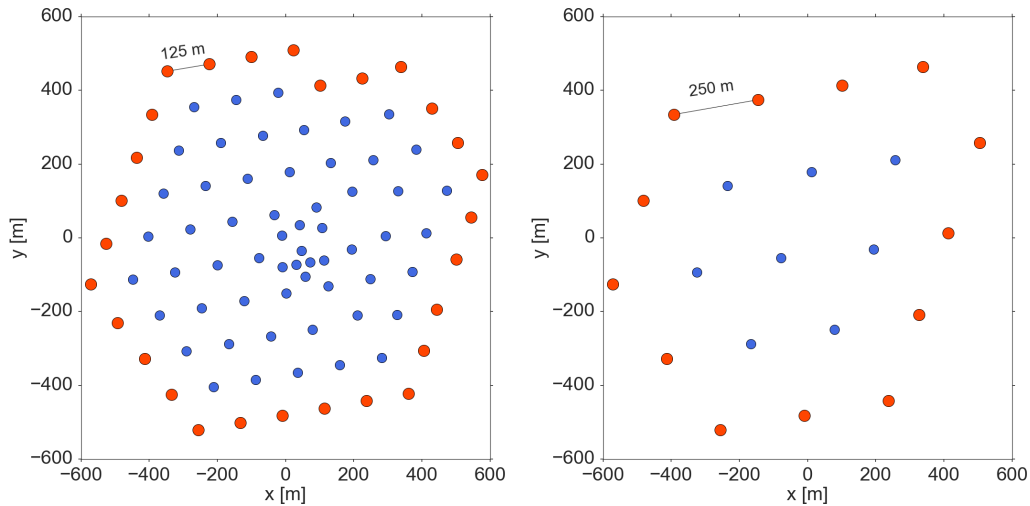


Figure 4: Left: top view of the IceCube detector. Strings that are completely used as veto are marked as red dots. Right: Top view of IceCube, after removal of strings from data to resemble a detector of increased string spacing.

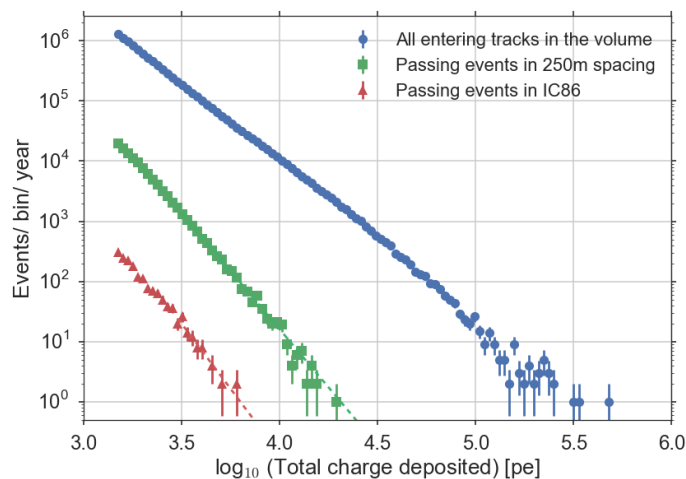


Figure 5: Number of background events passing the HESE filter before and after the removal of strings.

95 5. Development of new Veto

96 While a detector with a sparser grid can be evaluated using recorded data from IceCube, it
 97 is not possible to determine the effects of the increased size of Gen2 in this way. To investigate
 98 the efficiency of an in-ice self-veto for IceCube-Gen2, two sets of simulated data were generated.
 99 The background simulation made use of a parametrization of the in-ice muon flux, which was
 100 determined by simulating air showers and propagating the muons through the ice. The particle
 101 properties (energy, direction, position) were sampled from the predefined probability distributions,
 102 and then weighted to correspond to the primary cosmic-ray energy spectrum [8].

103 For the signal flux of atmospheric neutrinos, cascades were simulated uniformly throughout
 104 the detector volume. This provides a good approximation for neutrino induced interactions and
 105 is consistent with the position of the observed HESE events [3]. The simulated signal data set is
 106 weighted to the astrophysical neutrino flux, determined by IceCube:

$$E^2 \phi(E) = 1.5 \cdot 10^{-8} (E/100\text{TeV})^{-0.3} \text{GeV cm}^{-2} \text{s}^{-1} \text{sr}^{-1} \quad (5.1)$$

107 Figure 6 shows the energy distribution of the expected background and signal events. The
 108 ratio of the signal rate over the background rate shows how much the background has to be reduced
 109 to reach the level of the signal rate. At energies of 30 TeV and 100 TeV, the passing fraction of
 110 background should be smaller than 0.007% and 0.3%, respectively.

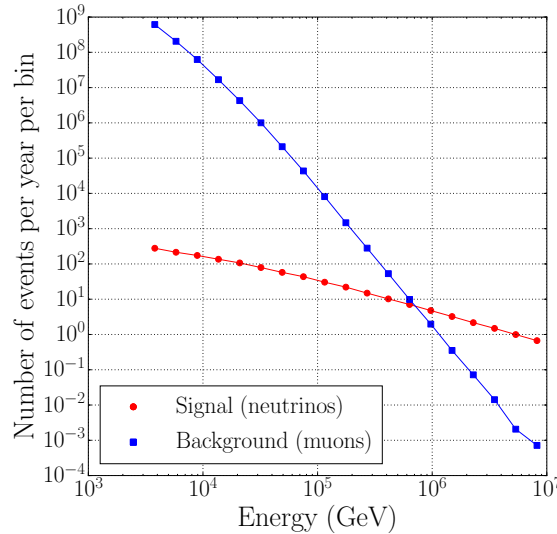


Figure 6: Predicted rates of signal and background events (single muons) in the sunflower 240 geometry as a function of the true energy before the muon enters the detector volume. The signal corresponds to the astrophysical neutrino flux of Equation 5.1. The plot shows the rates before the application of a veto.

111 To improve the background reduction for IceCube-Gen2, a new filter technique was developed
 112 as described in the following. As in the HESE procedure, balloon DOMs are removed from the
 113 events. Then a time window of 1 μs is shifted until it contains more than 10% of the total charge.
 114 The last hit of this time window is defined as a reference hit. If the number of causally connected

115 hits that occur in the veto region before the reference hit exceeds a certain number N , the event will
 116 be identified as incoming particle and removed. A hit is considered to be causally connected to the
 117 reference hit if the condition $|\Delta x/c - \Delta t| < \Delta t_{\max}$ is fulfilled, where Δx is the distance between the
 118 DOMs, Δt the time difference, and Δt_{\max} an adjustable parameter.

119 In this algorithm, several parameters can be optimized to achieve a sufficient background
 120 rejection. One set of parameters concerns the selection of the reference hit: the size of the time
 121 window can be tuned as well as the fraction of the total charge that is required to be collected in this
 122 time window. Another set refers to the selection of hits in the veto layer: the maximal number of
 123 hits N_{\max} and the causal constraint $(\Delta t)_{\max}$. Finally, also the configuration of the veto layer itself,
 124 specifically the number of DOMs in top layer, can be optimized.

125 In Figure 7, the fraction of passing background events is plotted against the signal efficiency
 126 for different veto hits and time constraints. With a low number of allowed veto hits N_{\min} and a
 127 high causal constraint $(\Delta t)_{\max}$, the background can be reduced by 3 orders of magnitude while
 128 keeping more than 60% of the signal for energies larger than 200 TeV. Additionally, the expected
 129 number of signal events per year is shown for different geometries. This plot demonstrates that the
 130 performance of the edge-weighted layout is inferior to the sunflower geometries for every energy
 131 region.

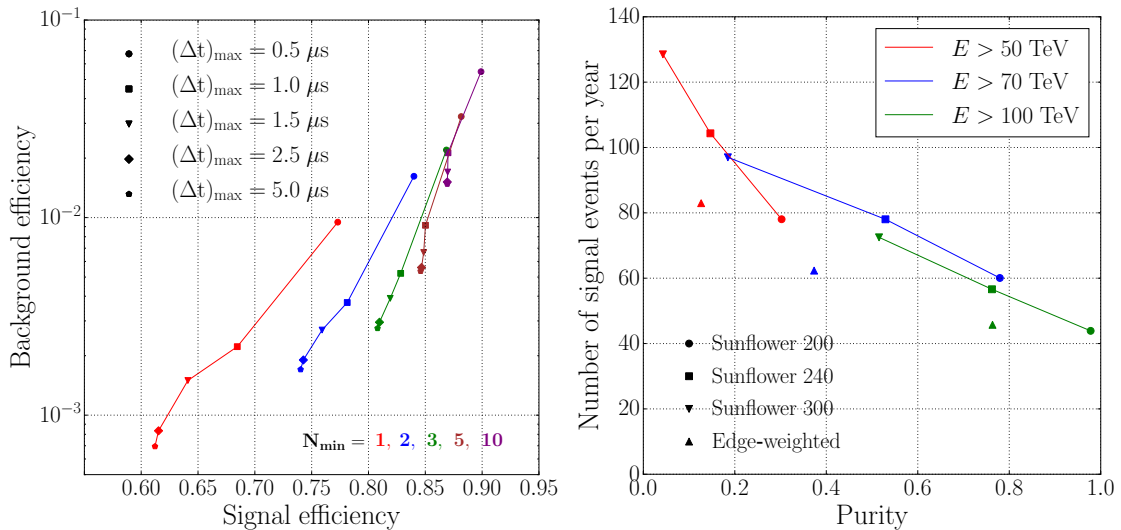


Figure 7: Left: Background vs. signal efficiency for different maximal hits in the veto layer N_{\max} and different causal constraints Δt_{\max} . The geometry configuration is sunflower 240 and a lower energy cut at $E > 200$ TeV is applied. Right: Expected signal events per year against the expected purity of the event sample for different detector geometries with lower energy cuts at 50 TeV, 70 TeV and 100 TeV. For each point, the parameters that maximize the purity are used for the veto. For both plots, the reference hit was chosen using a 1 μs time window that contains 10% of the total charge. The veto configuration includes the top 12 DOMs of GEN2 and the top 6 DOMs of IceCube.

132 6. Summary

133 Self-veto algorithms are a powerful technique for neutrino telescopes to filter the background

134 of incoming atmospheric particles. They played a key role in the discovery of the flux of astrophys-
135 ical neutrinos. We have shown that the application of the current IceCube filter to a detector with
136 larger string spacing would increase the energy threshold by a factor of three. Therefore new filters
137 have to be developed and optimized for a new detector geometry. These studies imply that the sun-
138 flower geometries will show a better performance with a in-ice self-veto than the edge-weighted
139 layout.

140 References

- 141 [1] **IceCube-Gen2** Collaboration, [PoS \(ICRC2017\) 991](#) (these proceedings).
142 [2] **IceCube** Collaboration, M. G. Aartsen et al., *JINST* **12** (2017) P03012.
143 [3] **IceCube** Collaboration, M. G. Aartsen et al., *Phys. Rev. Lett.* **113** (2014) 101101.
144 [4] **IceCube** Collaboration, M. G. Aartsen et al., *Phys. Rev.* **D91** (2014) 072004.
145 [5] **IceCube** Collaboration, M. G. Aartsen et al., *Astrophys. J.* **826** (2016) 220.
146 [6] **IceCube** Collaboration, M. G. Aartsen et al., *Eur. Phys. J.* **C77** (2017) 146.
147 [7] **IceCube** Collaboration, M. Ackermann et al., *J. Geophys. Res. Atmos.* **111(D13)** (2006) D13203.
148 [8] T. K. Gaisser, T. Stanev, and S. Tilav. *Frontiers of Physics* **8** (2013) 748.

A camera system for IceCube-Gen2

The IceCube-Gen2 Collaboration[†]

[†] http://icecube.wisc.edu/collaboration/authors/icrc17_gen2

E-mail: mjeong@icecube.wisc.edu, wkang@icecube.wisc.edu

The recent discovery of high-energy astrophysical neutrinos and competitive measurements of neutrino oscillation parameters by IceCube motivate a next generation Antarctic neutrino observatory. IceCube-Gen2 is a proposed extension to the current IceCube detector, which uses the extremely clean Antarctic ice as detector medium. While intense calibration efforts with LED flashers have resulted in a good understanding of the ice, ice properties still dominate systematic uncertainties in most analyses. To improve our knowledge of the ice, we propose a novel camera system integrated within the optical sensor modules. The camera system can be installed on all new optical sensor modules to determine their location and orientation and study ice properties. We describe how this system will help us to improve our understanding of the ice. We present a prototype system and simulation that demonstrates its merit.

Corresponding authors: M. Jeong^{*1}, W. Kang¹

¹ *Department of Physics, Sungkyunkwan University, Seobu 16419, Suwon, South Korea*

*35th International Cosmic Ray Conference -ICRC217-
10-20 July, 2017
Bexco, Busan, Korea*

*Speaker.

1. Introduction

The recent discovery of high-energy astrophysical neutrinos by IceCube [1, 2] as well as other results like the competitive measurement of neutrino oscillation parameters [3] have led to studies on possible extensions to the IceCube detector. IceCube-Gen2 [4] is a planned extension to IceCube with an increased detector volume of several cubic-kilometers and a new in-fill array in the current IceCube/DeepCore volume. The upgrade is based on the well proven design concept of IceCube and re-uses its fundamental components.

In IceCube a multitude of calibration devices including two bright calibration light sources called the Standard Candles, retrievable laser systems in the drill holes [5], and LED flashers have resulted in a detailed understanding of the optical properties of the Antarctic ice [6, 7]. The LED flashers, which are twelve radially outward pointing 405 nm LEDs located on each Digital Optical Module (DOM), are indispensable for the most advanced models of ice properties, as they provide calibration points throughout the detector [6]. Despite successful calibration efforts, the understanding of our detector medium can still be refined. In particular a detailed measurement of the refrozen ice in the drill hole promises improvements [8].

In 2010, two special devices, known as Swedish cameras, were deployed below the deepest DOM of IceCube string 80. They are housed in separate glass spheres 5.8 m apart at a depth of ~ 2455 m [7]. The cameras locally monitored the freeze-in process of the string and observed the formation of the refrozen hole ice. The system found unexpected dust deposits and that the refrozen drill hole contains a central, small region of short scattering length, referred to as bubble column. Motivated by the success of the Swedish camera system, we propose a similar but low-cost system to be directly integrated with future optical sensor modules. The main goal of the new system is to add survey capabilities to our sensor modules and to perform ice property measurements. There is good reason to expect that the environments around each DOM could differ significantly, for example resulting in a non-uniform azimuthal acceptance. With our proposed system the local ice environment can be determined. We introduce the objectives for our camera system in section 2 and then describe simulations to determine camera specifications in section 3. In section 4 we discuss design criteria and prototypes before concluding in section 5.

2. Camera System Objectives

The camera system is expected to conduct quantitative measurements of the ice properties and to deliver qualitative survey information that can be critical to interpret other calibration measurements. It is expected to have a large variety of applications, their relative importance is set by maximizing complementarity to other calibration methods with the overall goal to improve event reconstruction and to reduce ice related systematic uncertainties in analyses. Figure 1 provides an overview of potential measurements and their relative importance. As cameras and LEDs will not be absolutely calibrated the measurements need to rely on relative quantities.

2.1 Measurement of optical properties of the ice

The properties of the bulk ice, the undisturbed Antarctic ice, can be determined by observing the shape of the scattering halo of LEDs on adjacent strings. Absorption length and anisotropy

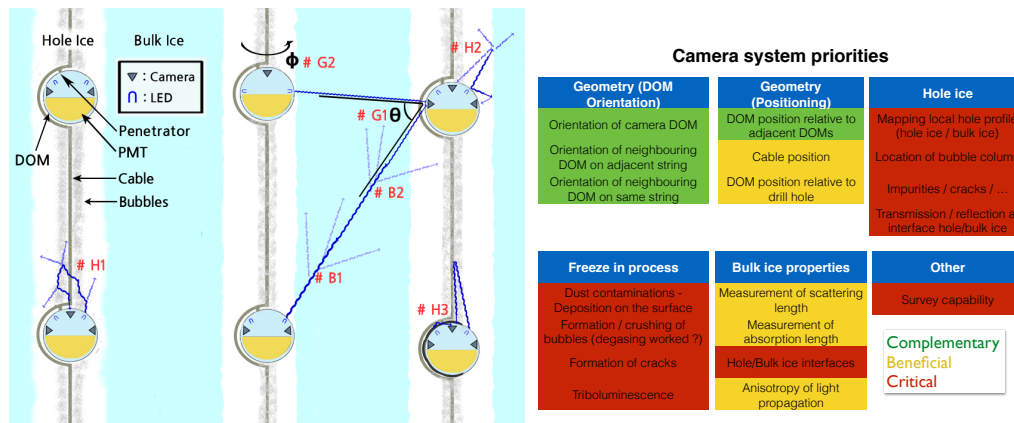


Figure 1: Schematic drawing to illustrate potential camera measurements including geometry (#G), hole ice (#H), and bulk ice (#B) are shown on the left. Relative priorities based on uniqueness of the measurement and complementarity to standard calibration measurements are shown on the right.

might be measurable by comparing the collective image from multiple cameras and LEDs. The hole and bulk ice interface could be observed in reflected light from LEDs and cameras on the same sensor. The measurement might be aided by comparing in-ice with in-water data.

2.2 Geometry Calibration

Deployment records are combined with LED flasher measurements in ice [7] to determine the position and orientation of the IceCube DOMs with high precision. Cameras could complement these well established geometry calibration methods and improve them or reduce calibration time. The main benefit of the cameras is expected to come from determining the positioning of the sensors within the drill hole.

2.3 In-water operation and Freeze-in process

The cameras can monitor the formation of ice and detect impurities. The system can provide fast feedback if degassing and filtering of drill water, which has been proposed for future drill operations, is effective. In-water data could be critical to understand hole ice formation and provide reference data to in-ice measurements at later times. While 98% of IceCube DOMs are working well, past failures have almost exclusively occurred during the freeze-in and deployment phase, hence camera operations in water would have to proceed with extreme caution.

2.4 Hole ice measurements

Cameras are expected to map the hole ice shape and to determine DOM positions relative to the hole ice walls. The position and extent of the bubble column can be determined and impurities can be located. The hole and bulk ice interface is expected to be visible from reflected light of LEDs within the same hole. However, images from the Swedish Camera suggest that this interface is not very prominent.

3. Camera simulations

To determine the camera hardware requirements and the optimal positioning of the LEDs and cameras, we run simulations and conduct image data analyses. Modeling realistic glacial ice, we determine camera requirements on angular resolution, sensitivity, and LED brightness and wavelength requirements to conduct the proposed measurements. We first introduce the basic simulation and image reconstruction before focusing on one example camera measurement, which was studied in great detail with our simulations. Additional simulations are on-going.

3.1 Photon propagation simulation and expected camera images

The photon propagating Monte Carlo simulation is designed to emit photons from LEDs and propagate them in the ice using IceCube's SPICE ice model [6, 10], derived from previous calibration studies. Cameras are simulated using the arrival direction of the photons received on a predefined surface area of the sensor modules. Oversizing of the light sensitive area is used to increase statistics. Camera and LED geometries are adjusted for the simulation measurements.

We inject photons following an LED emission profile and record the light received on the surface area of adjacent DOMs. In our simulation DOMs are spaced 17 m apart on the same string. The distance to adjacent strings is set to 20 m. Figure 2 shows the geometry setup and the received photons on the DOMs surfaces.

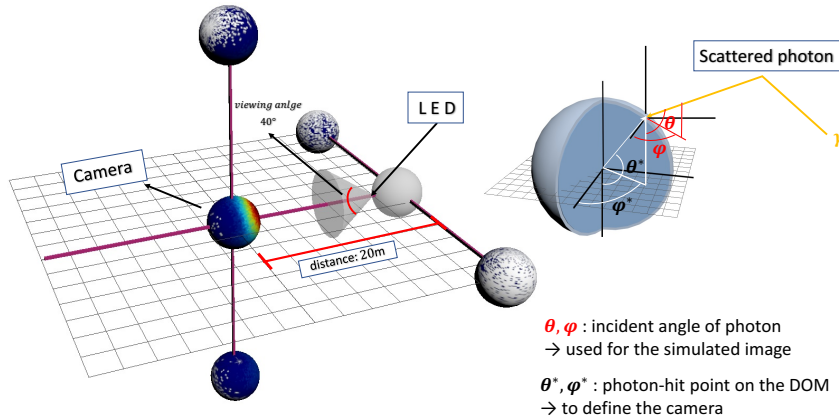


Figure 2: Left: Schematic view of simulation geometry. The DOM on the center right is emitting photons with a specific emission profile, visualized as a white cone. The DOM surfaces display the number of received photons on the point of the surface, varying from blue (small) to red (large). White indicates no counts. Right: θ' and ϕ' define positions on the DOM surface and are used to specify the camera area; θ and ϕ define the photon arrival direction of a photon γ . A camera image is given by the recorded θ and ϕ of all photons detected within a small camera area θ' and ϕ' . In yellow a scattered photon γ is shown.

In our simulation the entire DOM surface is photo sensitive with 100% efficiency. Incident angles of arriving photons are recorded and allow us to construct an expected camera image by defining a small surface area on the DOM. Our expected camera image consists just of the arrival azimuth and zenith directions of the photons over a small surface area of the DOM. The surface

area is kept small to avoid image distortion. We refrain from modeling a camera lens and sensor as it just represents a transformation of the photon arrival directions. A representative image from our simulation is shown in Figure 3. For the simulated camera image we use photon counts, in reality these would correspond to pixel amplitude values, neglecting noise.

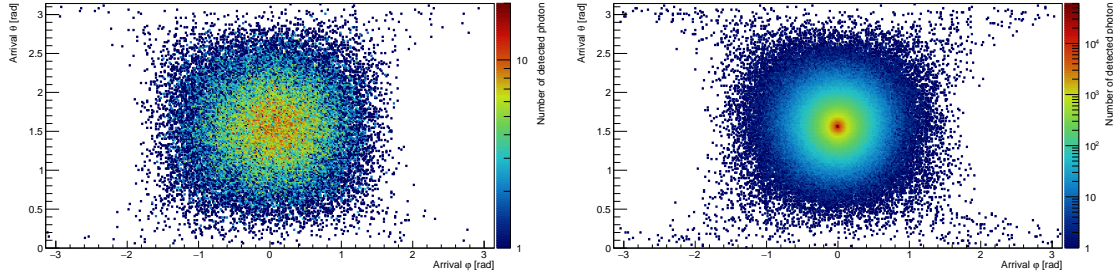


Figure 3: Simulated camera images for a camera observing an LED with 40° half-opening angle 20 m away. The left figure is for a short effective scattering length ($\lambda_e = 5.0$ m), which shows high-diffusion of photons. In contrast the right figure with a long effective scattering length ($\lambda_e = 77.6$ m) shows a more 'point source'-like result.

One relatively straight forward analysis to demonstrate how our simulations inform the design of the camera system is described in the following where idealized conditions to isolate individual ice property effects were used. A real data analysis with multiple ice effects present in an image could prove more complex.

3.2 Measurement of the scattering length in bulk ice

We perform an analysis to determine the sensitivity for measuring the scattering length in bulk ice. Two sensor modules are located 20 m apart at the same depth and a camera is directly looking at an LED that emits light following an emission profile with a 40° half cone opening angle. For each simulation 2.25×10^{10} photons are injected at a monochromatic wavelength of 405 nm. The effective scattering lengths, λ_e , are varied between 5 m and 77 m. Figure 3 shows the difference between the observed image for a short scattering length (left) and a long one (right). For the short scattering length a well-diffused circular shaped distribution is seen, while the long scattering length results in a 'point source'-like image with a small halo.

While images in Figure 3 qualitatively look very different we develop an image analysis that will be able to quantify the sensitivity for different scattering lengths in the bulk ice. As cameras and LEDs will not be absolutely calibrated we do not use absolute photon counts but only focus on the shape of the scattering halo. The cumulative distribution of the number of photons within a certain radius from the image center (location of the LED) is plotted and normalized (see Figure 4).

Figure 4 further shows that most of the image information is contained within a half-cone opening angle of 40° , which can be interpreted as minimum required FOV. Given that LEDs and cameras will not be aligned in the ice, multiple LEDs and wide field of view cameras are preferred.

4. System Design and Prototypes

After summarizing the basic design requirements we introduce our camera prototype system. We have to satisfy engineering requirements, while aiming for an optimal camera design based on

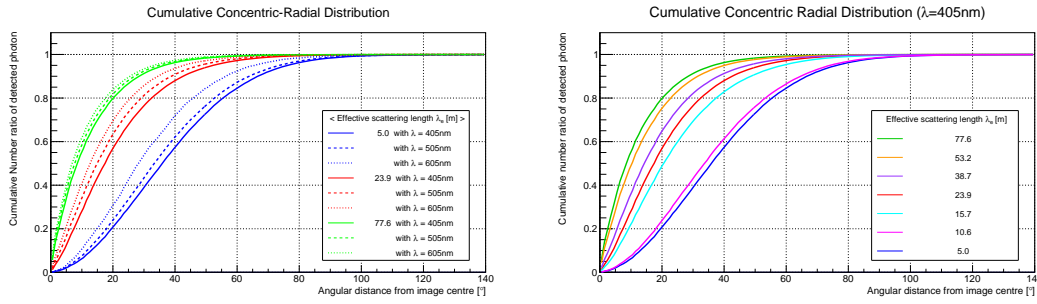


Figure 4: The cumulative photon hits as function of the angular distance from the light source centre for different scattering lengths and wavelengths. The ratio is with respect to all photons detected.

simulations, expected performance, and stability.

For maximal flexibility we propose a system of multiple cameras connected to a controller board (9.0 cm×9.0 cm), which then interfaces to the DOM. Camera boards are 3.5 cm×3.5 cm in size. In the ice the camera system is expected to operate at temperatures between -40°C and -20°C. Cameras will be tested down to -50°C. The maximum power consumption of the camera system needs to be kept below 2 W. The system will have no moving parts (fixed focus cameras) for maximal reliability and the number of parts is kept minimal for easy assembly. The system could be complemented with some manual cameras to allow for focus pulling.

To conduct ice property studies, cameras need to be in particular sensitive to observe not only the light coming directly from LEDs, but also scattered light. A large field of view (FOV) is preferred for the cameras to observe multiple neighboring strings. Note that the FOV needs to be adjusted for refraction in the ice. High camera resolution is not required, but could be beneficial for hole ice surveys or the identification of contaminants.

The camera system is designed to be an add-on to the DOM mainboard, as shown in Figure 5. A controller board with processor, RAM and flash memory will control up to three camera modules and communicate with the DOM mainboard. Cameras are connected via flat-flexible cables, which makes their positioning easier.

Prototypes of the camera system have been manufactured using CMOS and CCD image sensors, respectively. The prototypes are functional and are currently undergoing detailed lab testing.

The prototype of the CMOS camera uses the IMX225LQR-C image sensor from Sony. The sensor has 1.3 million pixels. Its pixels are able to measure the incoming light intensity with a 12 bit dynamic range. The sensor generates output image data through either a CMOS parallel interface, a LVDS or a MIPI interface, which makes it easy for the sensor to be controlled with a wide range of processors. The IMX225LQR-C image sensor is one of the most sensitive image

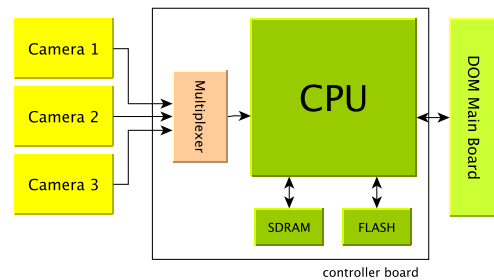


Figure 5: Structure of the camera system.

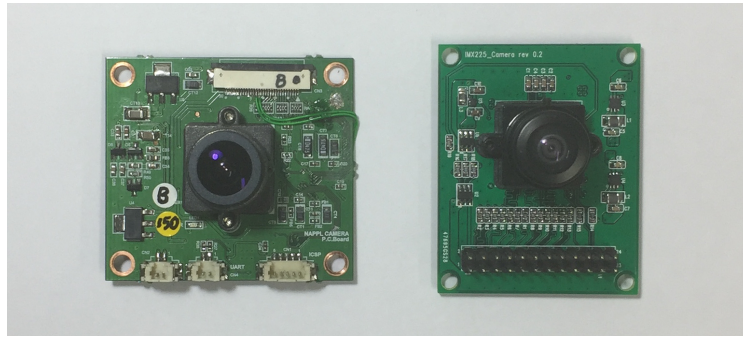


Figure 6: **Left:** A prototype of the CCD camera module built with the RJ33J3CA0DT image sensor from Sharp. The module is compatible with standard M12-mount lenses and can be connected to a controller board via the CSI connector. **Right:** A prototype of the CMOS camera module. It contains the IMX225LQR-C image sensor from Sony and is compatible with the M12-mount lenses. In the next version its 2×24 pin header will be replaced with a CSI connector.

sensors produced by Sony. From laboratory measurements we found that its sensitivity is superior to CMOS image sensors from other manufacturers.

The prototypes of the CCD camera module are built with the RJ33J3CA0DT and RJ33J4CA0DT image sensors from Sharp. They have the same specifications except that the former has color filters but the latter does not. They have the same number of pixels, pixel size, and diagonal length as the IMX225LQR-C sensor. The selection of the image sensors and the design of the camera prototype are made in order to compare the performance of the CMOS image sensor to CCD image sensors with similar specifications. Figure 6 shows the prototypes.

The prototype of the controller is built with a I.MX6Solo Microprocessor Unit (MPU) with an ARM Cortex-A9 CPU. The board contains 512MB of RAM and 8GB of flash memory. This

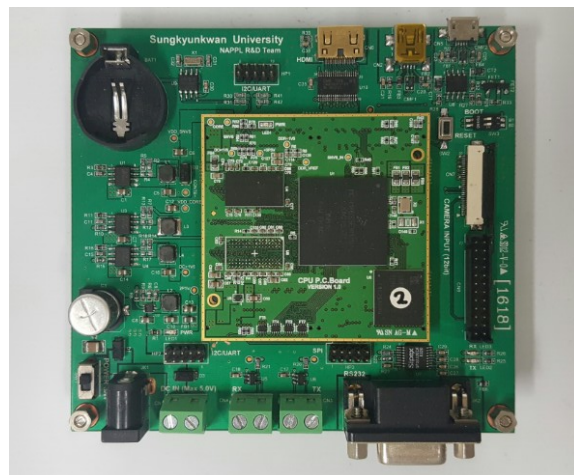


Figure 7: Prototype of camera controller board (rev 1). The rev 1 board is designed to evaluate functionalities of various camera modules. The board contains I.MX6Solo MPU, 512MB DDR3 RAM and 8GB eMMC. For evaluation purpose it includes a HDMI connector, a real time clock and a battery connector as well which will be removed in the next reversion.

board has enough performance to host both the CMOS camera and the CCD camera prototypes. The prototype of the controller board is shown in Figure 7. It includes additional connections for diagnostics and does not yet have a multiplexer. Therefore, for now only one camera module can be connected. After board evaluation a miniaturized revision will be prepared.

In the ice cameras will only be operated during camera calibration runs. In IceCube, four neighboring DOMs on a string share a common power allocation. To reduce the total power consumption of the camera systems only one camera system on each quad of DOMs would be operated at a time.

5. Conclusion

The proposed camera system allows for quantitative measurements of the optical properties of the hole ice, bulk ice and their interface, as well as the detector geometry. The qualitative informations from those measurements can be beneficial to interpret other calibration measurements. Furthermore, the system can be useful to monitor the freeze-in process of the drill holes.

The baseline design of the camera system consists of one controller board and three cameras. In order to achieve optimal performance, both CMOS cameras and CCD cameras are under study. Prototypes of the cameras with the two different image sensor types and the controller board have been produced and are being tested. In the near future their design will be revised to reduce power consumption and enable multiplexing.

In our simulations we have demonstrated that cameras can be used to measure ice properties, such as the effective scattering length, and introduced other potential camera measurements. While only qualitative results are shown in these proceedings, we are also focusing on the quantitative analysis to derive numerical results for the ice properties. Analysis to determine the sensitivity requirements, resolution, and field of view of various ice property measurements are in progress.

References

- [1] **IceCube** Collaboration, M. G. Aartsen et al., *Phys. Rev. Lett.* **113** (2014) 101101.
- [2] **IceCube** Collaboration, M. G. Aartsen et al., *Science* **342** (2013) 1242856.
- [3] **IceCube** Collaboration, M. G. Aartsen et al., *Phys. Rev. Lett.* **111** (2013) 081801.
- [4] **IceCube-Gen2** Collaboration, [PoS \(ICRC2017\) 991](#) (these proceedings).
- [5] N. E. Bramall et al., *Geophys. Res. Lett.* **32** (2005) L21815.
- [6] **IceCube** Collaboration, M. G. Aartsen et al., *Nucl Instrum. & Meth.* **A711** (2013) 73.
- [7] **IceCube** Collaboration, M. G. Aartsen et al., *JINST* **12** (2017) P03012.
- [8] M. Rongen, *EPJ Web of Conferences* **116** (2016) 06011.
- [9] **IceCube-Gen2** Collaboration, [PoS \(ICRC2017\) 1047](#) (these proceedings).
- [10] **IceCube** Collaboration, [PoS \(ICRC2013\) 508](#) (2014).
- [11] **IceCube-Gen2** Collaboration, [POS \(ICRC2015\) 1145](#) (2016).

The mDOM – A multi-PMT Digital Optical Module for the IceCube-Gen2 neutrino telescope

The IceCube-Gen2 Collaboration[†], M. Kossatz[‡], A. Kretzschmann[‡], S. Lindner[§], and D. Shuklin[§]

[†] http://icecube.wisc.edu/collaboration/authors/icrc17_gen2

[‡] DESY, Platanenallee 6, D-15738 Zeuthen, Germany

[§] FAU, Cauerstraße 9, D-91058 Erlangen, Germany

E-mail: lew.classen@icecube.wisc.edu

Following the first observation of an astrophysical high-energy neutrino flux with the IceCube observatory in 2013, planning for a next-generation neutrino telescope at the South Pole, IceCube-Gen2, is under way, which will significantly expand the sensitivity both towards high and low neutrino energies. The detector is envisioned to instrument 5 – 10 km³ of the deep clear ice with up to 10 000 optical modules to detect the Cherenkov light from charged secondaries created in the interaction of neutrinos in the ice. Apart from the larger volume, a significant increase in the sensitivity is expected to originate from advanced optical modules with several concepts currently being under development. One such concept is the multi-PMT Digital Optical Module (mDOM) which, in contrast to the “conventional” layout with a single ten-inch photomultiplier tube (PMT), features 24 three-inch PMTs inside a pressure vessel pointing isotropically in all directions. This layout provides an almost uniform angular acceptance and an increased effective area by more than a factor two. Additionally, directional information on the detected photons is obtained and background can be suppressed using local coincidences while at the same time the dynamic range of the module is increased.

The contribution provides an introduction to the design as well as an overview of the current status of mDOM development and prototype construction. It also highlights further optimization potential and remaining challenges en route to a fully functional multi-PMT optical module for IceCube-Gen2.

Corresponding author: L. Classen^{*1}

¹ WWU Münster, Wilhelm-Klemm-Straße 9, D-48149 Münster, Germany

35th International Cosmic Ray Conference — ICRC2017
10–20 July, 2017
Bexco, Busan, Korea

*Speaker.

1. Multi-PMT optical module concept

In contrast to the optical modules of all currently operative large volume neutrino telescopes, featuring a single large-area PMT inside a spherical pressure vessel, a multi-PMT optical module contains an array of smaller-sized PMTs. The effective segmentation of the sensitive area into individually read-out channels, first utilized in the Nevod detector [1] and introduced to the field of neutrino astronomy by the KM3NeT project [2], comes with several attractive advantages compared to the conventional single-PMT concept:

- **Increase of sensitive area:** The area of e.g. ten three-inch PMTs roughly equals one ten-inch tube. A multi-PMT module containing several ten such PMTs thus features a sensitivity equivalent to several conventional optical modules (for instance those of IceCube). As photons are the only source of information in a neutrino telescope, the collection of more photons means more information and consequently better reconstruction of event signatures assuming similar time resolution.
- **Superior photon counting:** The total number of arrived photons can be more directly derived from the number of hit PMTs compared to the extraction from a multi-photoelectron signal waveform. This feature can be e.g. be useful for a simple definition of cuts on the photon number by requiring a certain number of hit PMTs per module.
- **Extended dynamic range:** Cathode segmentation also benefits the overall dynamic range of the module, as multiple photons arriving at the same time are more likely to hit different PMTs. Assuming comparable dynamic ranges of small and large PMTs, the collective range is extended by a factor given by the number of small PMTs facing one direction.
- **Improved angular acceptance:** With the distribution of the sensitive area across the total solid angle, a near-homogeneous 4π coverage is achieved. This is particularly important as the power of modern analyses is based on 4π sensitivity [3].
- **Intrinsic directional sensitivity:** The orientation of the hit PMT, in combination with its known angular acceptance (see Fig. 2, b), carries additional information on the direction of the incoming photon available for event reconstruction.
- **Local coincidences:** Coincidences between individual PMTs of a module allow the suppression of uncorrelated background as well as the identification of low-energy neutrinos as for example generated in supernova explosions.

The hardware functionality and physics capability of the multi-PMT concept have in the meantime been demonstrated in-situ with the deployment and operation of KM3NeT prototypes in the Mediterranean [4]. Due to the development of suitable three-inch PMTs by several manufacturers these devices are meanwhile available at moderate prices resulting in the “price per photocathode area” for a multi-PMT module being comparable to, or even lower than, the value for the conventional layout.

2. mDOM – a novel optical module for IceCube-Gen2

With a substantially expanded sensitivity range, spanning from GeV to \sim EeV neutrinos, IceCube-Gen2 [5], the next-generation Antarctic neutrino telescope, is designed to identify the

sources of the high-energy cosmic neutrinos discovered in IceCube, including a detailed spectral analysis and flavor measurement. At the lower end of its sensitivity spectrum it will address neutrino physics investigating atmospheric neutrinos. The mDOM (multi-PMT Digital Optical Module) project aims at bringing the advantages of the multi-PMT concept to the South Pole.

The design, originally based on the optical module of KM3NeT, has been under development for several years and is currently entering prototype construction phase. The completion of a first, fully functional module is scheduled for late 2017. In this prototype configuration the mDOM features an isotropically oriented array of 24 reflector-equipped three-inch PMTs harbored by a quasi-spherical 14-inch borosilicate glass pressure vessel. An explosion view of the prototype layout is presented in Fig. 1 highlighting the main components. Most mechanical components have been verified individually in the lab, or currently are in the process of qualification, without the emergence of show-stoppers.

The mDOM **pressure vessel** will slightly deviate from the optimal spherical form factor. The design is driven by the limited diameter of the borehole and the non-reducible length of the PMTs. Based on finite-element simulations by the manufacturer, the pressure vessel is rated for 700 bar. This criterion, which is substantially larger than the hydrostatic pressure at the location of the detector, is based on the measured pressure peaks during re-freezing: up to 550 bar were observed during IceCube construction. The design was optimized for mass production with the final price not significantly deviating from comparable commercially available spherical vessels. Several specimen have been acquired from Nautilus GmbH and are currently used for tests.

Curing two-component **silicone gel**, poured between the PMTs and the pressure vessel, provides optical coupling as well as structural stability. The baseline choice for prototyping is QGel 900 by Quantum Silicones which has been employed in the original IceCube optical module and proven to be usable at low ambient temperatures.

Mounted around the entrance window of the PMTs, light concentrators or **reflectors** increase the PMT's effective area for vertical illumination. The devices are produced from enhanced-reflectivity coated aluminum sheets. Considering the entire solid angle, they merely redistribute the PMT's angular acceptance, resulting in no net gain in sensitivity. In practice however, reflec-

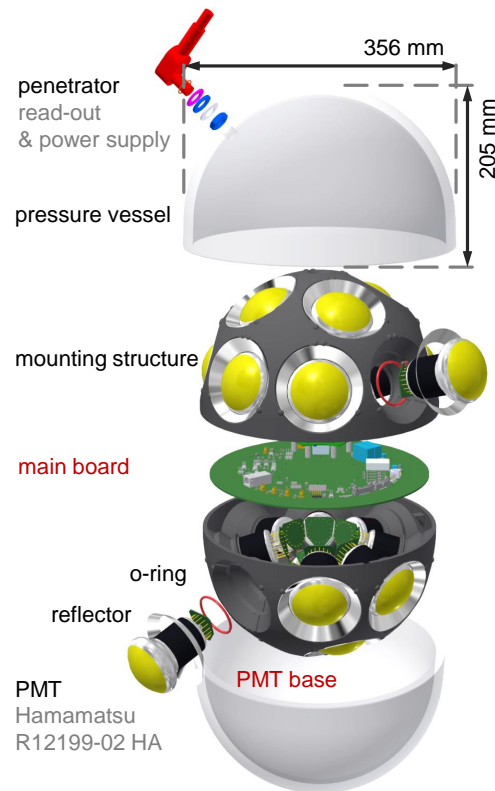


Figure 1: Default configuration of the mDOM, featuring main components. The development of the devices marked *red* needs to be finalized before prototype production.

tors allow to reclaim photons otherwise lost to shadowing and absorption in glass and gel¹. With respect to realistic configurations the utilization of reflectors yields an extra $\sim 20\%$ in overall module sensitivity. The material² was chosen to maximize the average Cherenkov-weighted reflectivity based on lab measurements. In a Monte Carlo study, simulating the incidence of a plane wavefront, the opening angle was optimized to provide maximum sensitivity for vertical photons, narrowing the PMT's field of view. This resulted in a final angle of 51° with respect to the symmetry axis of the PMT. The effective concentration of the photon acceptance at small incidence angles comes at only marginal cost in terms overall PMT sensitivity ($< 1\%$ deviation from the achievable maximum).

The default **PMT** for prototype construction is the R12199-02 HA model by Hamamatsu Photonics, which is based on the main PMT of the KM3NeT project. This model performed best during the mass screenings of quantum efficiency, transit-time spread, dark rate and the probability of spurious pulses conducted by the collaboration [6].

The PMTs low temperature operability was tested down to -60°C . While all other characteristics were not affected significantly, the gain and the dark rate were found to improve with cooling, with the gain increasing by some 10% and the noise rate dropping to $\sim 50\text{s}^{-1}$ measured at a ~ 0.3 photoelectron threshold level. Simplifying read-out circuitry, the PMTs are operated with negative supply voltage (i.e. cathode at negative potential, anode grounded). In order to reduce the noise entailed by this choice, the PMTs will be used in a configuration where its conductively coated outer surface is placed at cathode potential (HA coating). For further noise reduction the (electrically conductive) reflectors will be connected to the photocathode potential, as floating (or even grounded) reflectors were found to promote high and unstable dark rates.

A **mounting structure** is used to position PMTs, reflectors and the main electronics board inside the pressure vessel. This component is produced via selective sintering (aka three-dimensional printing) from (white) polyamide and subsequently painted dull black with a non-conductive acrylic paint. The color was chosen as a white structure only marginally increases the overall module sensitivity while enhancing the amount of undesired photon scattering. In addition to positioning, the design ensures electric insulation of the photocathode with gel pockets, required by the negatively fed PMTs.

Power is supplied via twisted pair copper cables limiting the total power budget of all modules connected to one wire pair to 9.4 W. For the mDOM a consumption of $< 3\text{W}$ is targeted, allowing to mount three modules per pair. The **PMT base** is therefore equipped with low-power Cockcroft-Walton circuitry for in-situ high-voltage generation based on a Nikhef design [7] as well as front-end electronics. As a detailed digitization of the PMT pulse is not feasible within the tight power constraints, in the baseline digitization concept, the analog waveform is split after pre-amplification and passed to four base-borne discriminators with independently adjustable thresholds. The four (analog) time-over-threshold (ToT) step signals from the PMT are routed via single-ended circuit board tracks to an FPGA on the **main board** [8], clocked at 150 MHz, where the leading and trailing edge times for each channel are determined. Parallel processing allows an effective sampling of each channel at a rate of 600 MHz. As two channels are employed in digitizing data from the lowest threshold, the resulting effective sampling is 1.2 GHz at this level.

¹The traversed layer thickness increases significantly for flatly incoming photons.

²Almeco Vega 95-100

The information finally available on each pulse amounts to four time-stamped ToT values. As of now, major aspects of the electronics functionality have been successfully tested in prototype setups. In-situ high-voltage generation was found to work. The base features anode output linearity (on a 10% level) up to ~ 500 photoelectrons deposited in $\lesssim 1$ ns. A problem was found in spiked noise, generated on the base below $\sim 0^\circ\text{C}$, which is currently being investigated. The functionality of the multi-ToT digitization scheme was also assessed and found to work as expected. The demonstration setup included analog ToT generation, signal transport to an FPGA, as well as the digitization of the leading and trailing edge times. The signal-transit time is shown as an example of the performance in Fig. 2, d.

This output signal will be transferred to a stand-alone **test bench** computer for storing and analysis. Upon completion, the prototype will undergo an extensive scrutinizing program in the lab to verify its functionality and readout. In addition, in-situ qualification and calibration studies will be performed placing the mDOM inside the Nevod detector in Moscow. Simultaneous read-out of the Nevod modules will e.g. enable mDOM calibration using atmospheric muons as a source of Cherenkov light.

The expected **mDOM performance** was studied in Geant4 simulations³, in particular in comparison to the properties of an alternatively proposed enhanced high quantum efficiency IceCube DOM (PDOM), providing a reference for the planned qualification tests. If not stated otherwise the properties were derived for the region of maximum ice transparency, i.e. between 200 nm and 600 nm. Maximum **sensitivity inhomogeneity**⁴ across the total solid angle was found to be $\sim 10\%$ (see also Fig. 2, a). Depending on whether a Cherenkov style $1/\lambda^2$ photon spectrum or a flat one is assumed⁵, the mean mDOM sensitivity, in the prototype configuration discussed here, surpasses that of the considered single-PMT module by a factor of ~ 2.25 to ~ 2.15 . This figure of merit was derived averaging the simulated effective areas, with respect to an incident plane wave, for both optical modules over the solid angle and the ice transparency window, including known respective quantum efficiencies (Fig. 2, c).

To illustrate the potential of intrinsic **directionality**, the capability of a single mDOM to reconstruct the direction to an isotropic photon point source was assessed. The direction to the source was determined fitting the maximum of the cumulative fields of view of all 24 mDOM PMTs, weighted by the respective number of detected photons. In an idealized scenario⁶ this simple approach allows to reconstruct the direction of the source at a distance up to 100 m with a precision of $\lesssim 1^\circ$, based on a total of $4 \cdot 10^{12}$ emitted photons. A more sophisticated version of the algorithm, will allow to determine in-situ the orientation of the mDOM in the ice using the POCAM [9] calibration module⁷.

³The detailed simulation model features realistic geometries as well as optical material properties of the respective modules and was validated against lab measurements.

⁴Given in terms of the relative deviation from maximum acceptance.

⁵As UV photons experience stronger scattering in the ice the original Cherenkov spectrum becomes flatter with distance.

⁶Assuming homogeneous ice without dust layers featuring the properties of the relatively clean environment at a depth of ~ 2278 m.

⁷The Precision Optical CALibration Module will produce isotropic light pulses of up to 10^{10} photons each. Thus, the number of photons needed to achieve the discussed precision corresponds to 400 pulses only.

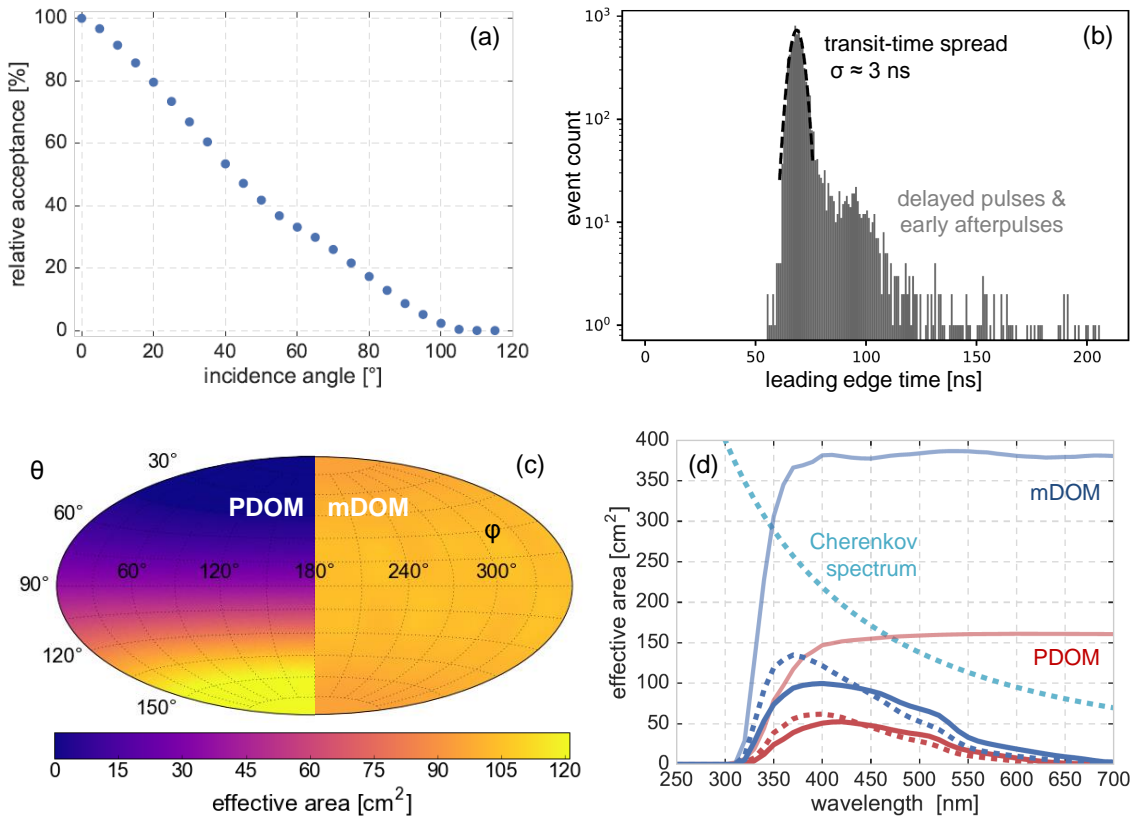


Figure 2: Module sensitivity simulated for the prototype mDOM configuration: (a) Effective area comparison between the mDOM and an high quantum efficiency single-PMT module (PDOM). (b) Angular acceptance profile of a Hamamatsu R12199-02 PMT inside the mDOM. (c) Solid-angle averaged effective areas of mDOM and PDOM. Spectra are shown including (*solid line*) and excluding (*light solid line*) the quantum efficiencies of the respective PMTs. *Dashed lines* mark the Cherenkov spectrum and respective Cherenkov-weighted effective areas in arbitrary units. (d) Readout functionality demonstration: Single photoelectron signal transit-time distribution determined with the prototype readout consisting of PMT, four-comparator base and digitizing FPGA.

3. Challenges and perspectives

Although the design of the module is quite mature, some components require work before deployment in the deep ice while others have the potential to be further optimized. Together with corresponding improvement strategies they will be discussed in this section, as will additional devices not included in the prototype. Further enhancement perspectives are expected to be revealed in the course of the qualification phase.

The Vitrovex glass of the default **pressure vessel** surpasses the Benthos glass of the original IceCube module in terms of UV transparency and is in turn outperformed by the custom glass mixture employed in the D-Egg [10]. The gain from using these glasses was simulated to be $\sim 15\%$ and $\sim 20\%$, respectively. During noise investigation Vitrovex glass was found to contribute

significantly to the background rate. In fact, due to the purity of the polar ice, glass-induced noise will be the main signal acquired by the PMTs, defining the data rate, and therefore the amount of required compression given the limited bandwidth of the copper cables foreseen in IceCube-Gen2. Background from the Benthos glass was found to be considerable lower⁸. In the current state of the investigations, the noise was traced back to scintillation induced by charged secondaries of the decay of trace elements with an additional smaller contribution from Cherenkov radiation. Being vital for the understanding and prediction of the final rate, the photon yield, spectrum, as well as the decay time of this scintillation are now subject to detailed investigation. While the Vitrovex glass will be used for prototype construction, alternative low-background glasses, favorable not at the cost of UV sensitivity loss, are under consideration for the final module. In addition negotiations with Nautilus GmbH concerning possibilities for reducing the radioactive contamination are under way. The structural stability of the component, as well as pressure-induced shrinking, will be assessed in a hyperbaric chamber.

As the current⁹ default **optical gel**, QGel 900 by Quantum Silicones, slightly reduces the module sensitivity at short wavelengths due to its transmission properties, alternative brands are under consideration. One possible choice is the custom gel developed for the D-Egg, featuring superior transmission properties, including better UV transparency, once it becomes commercially available. At the moment the default gel is investigated for chemical compatibility¹⁰ with other mDOM components, as well as for its scintillation properties, which are crucial for the estimation of its background noise contribution.

Based on the efforts of several manufactures for the KM3NeT project, fast, enhanced-area three-inch **PMTs** are now available from several companies at moderate cost. While the Hamamatsu PMT is currently considered the baseline, alternative models by ET Enterprises, HZC and MELZ, feature comparable performance while surpassing its photocathode area by up to $\sim 25\%$. Their employment in the mDOM allows for an easily accessible sensitivity increase of the final module by this factor. Early 2017 saw the availability of a so-called “super-bialkali”, enhanced quantum efficiency version of the Hamamatsu R12199-02 PMT featuring an average sensitivity gain of 35% to 40% with respect to the default PMT. A shortened version of the tube is now also offered, allowing to loosen the tight space constraints on module electronics. Specimen of both models have been acquired and their properties are subject to detailed study at the moment.

As introduced above, the mDOM prototype will feature a four-level pulse digitization. In a more ambitious approach the analog PMT output will be fed into a custom base-borne ASIC, comprising 63 comparators in its final version thus allowing for a detailed sampling of complex waveforms. The individual comparator levels, featuring level precision of $200 \mu\text{V}$ and a maximum amplitude of $\sim 1.8 \text{V}$, can be defined by combining the 255 equidistant steps resulting from an 8-bit equal resistor chain. An optimization study concerning level location is under way. The ASIC also contains a $2^N - 1$ to N encoder which reduces the data to a 6-bit output word. As in the baseline design the output is time stamped in a central FPGA. The higher level of integration will also reduce power consumption. The layout of a first reduced-performance version of the ASIC (featuring 31

⁸A factor of ~ 2.5 was found between the rates generated by Vitrovex and Benthos glass, respectively

⁹The originally envisaged Wacker 612 gel, used in KM3NeT, was found undergo undesired crystallization, turning hard and opaque, at low temperatures.

¹⁰A variety of materials can inhibit gel curing so that great care has to be taken here.

thresholds) has been recently completed.

The space available between the individual PMTs of the mDOM is foreseen to harbor **calibration devices**, such as fast LED pulsers and potentially also cameras [11], which will enhance the mDOMs potential for self- as well as inter-DOM calibration.

In the final in-ice configuration the optical modules will be attached to the vertical electro-mechanical cable by means of metal cables and a so-called harness produced from stainless steel. It is foreseen to modify the proven IceCube “waist-band” [8] with the goal of minimum PMT shadowing. A reduction of cable mounting points from three to two is also under consideration.

Simulations of the entire future detector comparing the performance of all considered **optical module alternatives**, namely PDOM [8], D-Egg [10], WOM [12], and mDOM, in terms of horizontal muon reconstruction precision are under way in the collaboration [13]. As of now, the mDOM performance is consistent with its increased sensitive area throughout the considered muon energy range, while at the low end, corresponding to few GeV, it is further enhanced by the segmentation of the cathode area.

4. Summary

The adaptation of the multi-PMT concept for the South Pole has resulted in the development of the mDOM for IceCube-Gen2. The project is currently entering prototype production phase expecting a fully functional prototype by the end of the year.

References

- [1] V. M. Aynutdinov et al., *Ap&SS* **258** (1), (1997) 105 – 116
- [2] **KM3NeT** Coll., S. Adrián-Martínez et al., *J. Phys.* **G43** (8), (2016) 084001 [[arXiv:1601.07459](https://arxiv.org/abs/1601.07459)]
- [3] **IceCube** Coll., M. G. Aartsen et al., *Phys. Rev. Lett.* **113**, (2014) 101101 [[arXiv:1405.5303](https://arxiv.org/abs/1405.5303)]
- [4] **KM3NeT** Coll., S. Adrián-Martínez et al., *Eur. Phys. J.* **C76** (2), (2016) 54 [[arXiv:1510.01561](https://arxiv.org/abs/1510.01561)]
- [5] **IceCube** Coll., M. G. Aartsen et al., (2014) [[arXiv:1412.5106](https://arxiv.org/abs/1412.5106)]
- [6] C. M. Mollo et al., *JINST* **11** (08), T08002 (2016) [[arXiv:1604.03922](https://arxiv.org/abs/1604.03922)]
- [7] P. Timmer, E. Heine and H. Peek, *JINST* **5** (12), (2010) C12049
- [8] **IceCube-PINGU** Coll., P. Sandstrom et al., *AIP Conf. Proc.* **1630**, (2014) 180–183
- [9] **IceCube-Gen2** Coll., PoS (ICRC2017) 934 (these proceedings)
- [10] **IceCube-Gen2** Coll., PoS (ICRC2017) 1051 (these proceedings)
- [11] **IceCube-Gen2** Coll., PoS (ICRC2017) 1040 (these proceedings)
- [12] **IceCube-Gen2** Coll., PoS (ICRC2017) 1052 (these proceedings)
- [13] **IceCube-Gen2** Coll., PoS (ICRC2017) 991 (these proceedings)

1 The IceTop Scintillator Upgrade

The IceCube-Gen2 Collaboration[†]

[†] http://icecube.wisc.edu/collaboration/authors/icrc17_gen2

E-mail: samridha.kunwar@desy.de

The IceCube Neutrino Observatory at the South Pole probes the high-energy cosmic-ray sky by investigating the muonic and electromagnetic component of air showers measured with IceTop and the in-ice detector. However, more detailed measurements are needed to understand the astrophysics of the high-energy cosmic-ray sky. This, along with the need to mitigate the impact of snow accumulation on IceTop tanks, has given us impetus for further upgrades including scintillator and SiPM-readout-based stations. Prototype stations showcasing technological advances for the next generation in cosmic ray detection are currently under construction for deployment at South Pole in December 2017. We describe the physics and the current status of the project.

Corresponding authors: Thomas Huber^{1,3}, John Kelley², Samridha Kunwar^{*3}, Delia Tosi²

¹ *Institut für Kernphysik, Karlsruhe Institute of Technology, D-76021 Karlsruhe, Germany*

² *Dept. of Physics and Wisconsin IceCube Particle Astrophysics Center, University of Wisconsin, Madison, WI 53706, USA*

³ *DESY, D-15738 Zeuthen, Germany*

*35th International Cosmic Ray Conference — ICRC2017
10–20 July, 2017
Bexco, Busan, Korea*

*Speaker.

1. Introduction

IceCube is a cubic-kilometer neutrino detector installed in the ice at the geographic South Pole [1] between depths of 1450 m and 2450 m, which was completed in 2010. Reconstruction of the direction, energy, and flavor of the neutrinos relies on the optical detection of Cherenkov radiation emitted by charged particles produced in the interactions of neutrinos in the surrounding ice or the nearby bedrock. Additionally, an array of surface detectors, IceTop, has also been deployed for cosmic ray studies in the PeV energy range [2] and to provide a partial veto of the down-going background of penetrating muons.

Accumulating snow cover of the IceTop tanks is continuously increasing the energy threshold for the detection of cosmic ray air showers [3]. The complex attenuation effects of the snow add systematic uncertainties to air shower measurements, particularly in the mass composition analysis. We have designed and proposed an upgrade to IceTop consisting of an homogeneously-spaced scintillator array with an areal coverage similar to IceTop. Currently we plan on deploying up to 37 scintillator stations over several years as shown in Fig 1. Each scintillator station comprises of seven scintillator panels communicating with a central hub as shown in Fig 2.

This upgrade is planned for two phases of deployment. Phase 1, marked in red in Fig. 1, will enable us to study the effect of attenuation on high-energy air showers. As stations are added during phase 2, marked in green in Fig. 1, the coverage will improve and the energy sensitivity will expand to include low-energy air showers.

2. System Overview

We are exploring different detector designs as prototype solutions for the upgrade. The system (Fig. 2) features the following building blocks:

- The scintillator panel subsystem. Extruded plastic scintillators are used in combination with wavelength-shifting fibers to collect and guide the light produced by an energetic particle crossing the scintillator. The fibers are read out by one light sensor. The detector is enclosed in a mechanical structure, designed to be light-tight and provide protection from harsh environmental conditions.

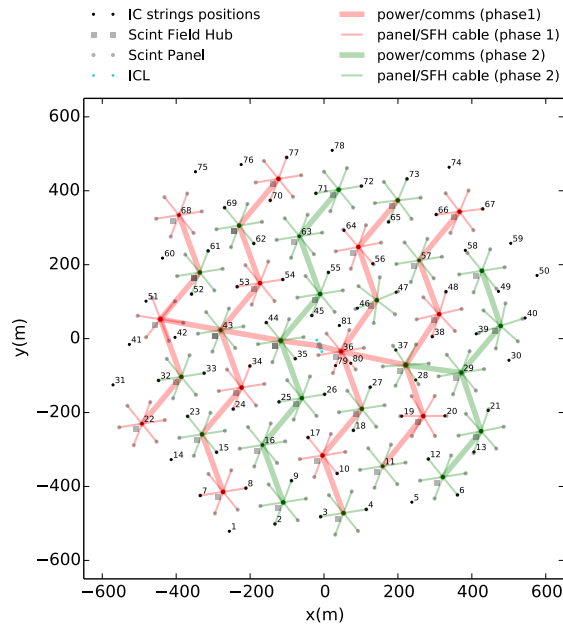


Figure 1: Map of the scintillator array as designed for the IceTop upgrade, in IceCube coordinates. Each number denotes the location of an existing IceTop station.

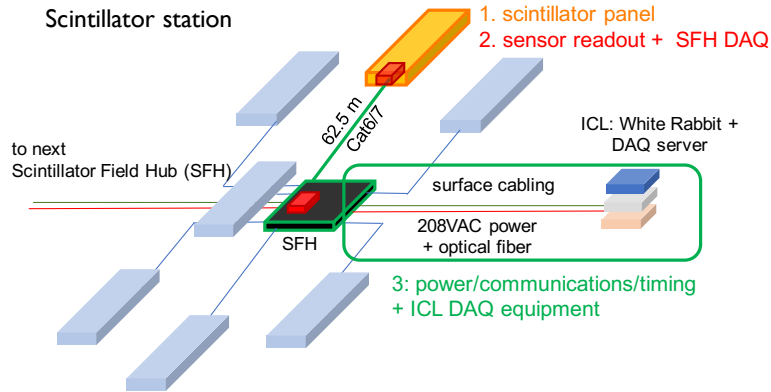


Figure 2: Scintillator station with 7 scintillator panels connected to a Field Hub DAQ featuring White Rabbit timing. The three building blocks as described in the text are highlighted.

- 40 • The DAQ subsystem: the light sensor is read out and data are processed by a custom-designed
- 41 data acquisition system.
- 42 • The Scintillator Field Hub (SFH) subsystem includes data handling, power, and timing dis-
- 43 tribution between the IceCube Laboratory (ICL) and each scintillator station. It also includes
- 44 equipment in the ICL.

45 We have developed multiple realizations for each of the building blocks to explore different

46 solutions in terms of costs and complexity. In the following sections we describe each subsystem

47 in more detail.

48 **3. The scintillator panel subsystem**

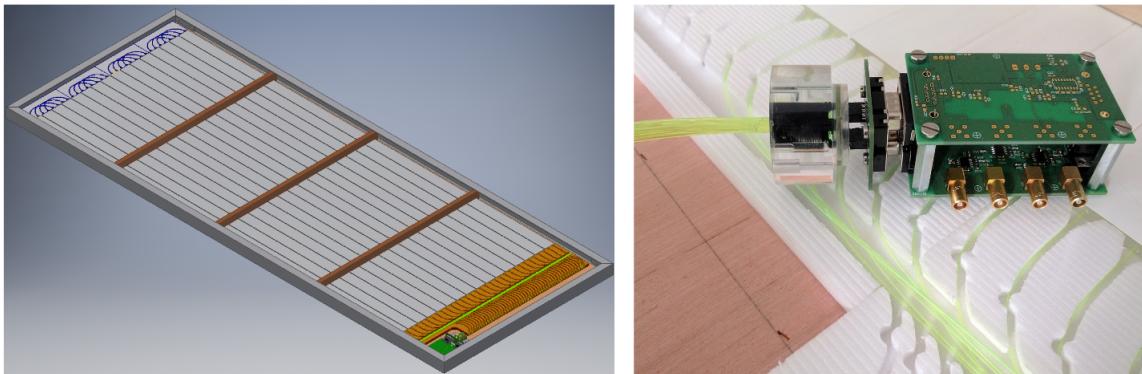


Figure 3: Left: Layout of the detector without top plate. The detector is placed in an aluminum frame to provide support. Right: optical fiber routing, plastic scintillator bars and a prototype of the Analog Readout Module for the IceTAXI Design (sec. 4.1), fully attached to the optical coupling of the detector. The SiPM is inside the cookie coupler which connects the optical fibers with the cookie board.

49 The detector design utilizes the low-cost customizable geometry of extruded scintillators sim-

50 ilar to those adopted by many other particle physics experiments in recent decades, such as SciBar

51 at K2K [4], the T2K near detector [5], MINERvA [6], and Auger Prime [7].

52 The unit detector is designed to have a total sensitive area of 1.5 m² and a total weight of less
53 than 50 kg, to be easily transportable by two people. Each panel comprises 16 extruded plastic
54 scintillator bars (produced on the FNAL/NICADD¹ Extrusion Line), made of polystyrene with
55 doping of 1% PPO and 0.03% POPOP and coated with a 0.25 mm±0.13 mm thick layer of TiO₂
56 reflector. Each bar is 1 cm thick, 5 cm wide and 1.875 m long and has two holes with a diameter of
57 2.5±0.2 mm. Two Y-11(300) wavelength shifter fibers (produced by Kuraray²) are routed into the
58 two holes of two bars, resulting in a bundle of 32 fiber ends which is then readout by a 6×6 mm²
59 Silicon PhotoMultiplier (SiPM).

60 We are currently exploring the use of either 0.7 mm or 1 mm fiber, which offer different ad-
61 vantages in terms of cost and light yield. The light yield has been studied with a detailed GEANT4
62 [8] simulation of the apparatus, resulting in 82.3 ± 23.9 and 137.1 ± 36.7 photons absorbed in the
63 SiPM for the 0.7 mm and 1 mm fiber respectively.

64 The fiber routing inherits features that were intensively studied for the AugerPrime upgrade of
65 the Pierre Auger Observatory with the goal of optimizing sensitivity and uniformity. The bars are
66 wrapped in opaque Velostat (ESD) material to ensure light-tightness. An outer aluminum shell and
67 an aluminum frame provide support. A prototype panel is shown in Fig. 3.

68 Two types of coupling are being explored. In the first type, the bundled fibers are cast into
69 a solid cookie with the fiber ends being cut and heated on a hot glass plate ensuring robustness
70 and long term stability. The cookie is then glued into a PMMA (Polymethyl methacrylate) coupler
71 along with the SiPM on a PCB — the cookie board. A 1 mm gap between the SiPM and the
72 fiber ends is filled with optical glue (EJ-500³) suited for low temperatures. This gap allows the
73 illumination of every pixel on the SiPM and thereby increases the dynamic range. The second
74 coupling makes use of a custom designed printed circuit board (PCB) that features holes of the
75 same diameter as the fiber and are homogeneously spaced to guarantee illumination of the whole
76 sensor active area. The fibers are threaded into the PCB and glued with a cold-rated epoxy. The
77 bundle is then cut and polished with a slant cabochon lapidary polisher. The fiber bundle is then
78 pressed against the SiPM surface with a spring loaded mechanism, with or without coupling gel.

79 4. The DAQ subsystem

80 4.1 IceTAXI

81 In this design, the SiPM is first connected to an analog readout module that comprises: the
82 cookie board with analog and digital temperature sensors; an adapter board designed for mechani-
83 cal stability that allows the cookie board and SiPM to be mounted inside the cookie; a readout board
84 that houses the power supply for the SiPM and three different pre-amplifiers (×1, ×5, ×10); and
85 finally, a general purpose board that contains line drivers to transmit the analog signal from the
86 scintillator panel to the SFH and a micro-controller for slow control (temperature, current, and
87 voltage monitoring and control) via an RS485 connection.

¹<http://www.fnal.gov/facilities>

²<http://kuraraypsf.jp>

³<http://www.ggg-tech.co.jp/maker/eljen/ej-500.html>

88 The IceTAXI DAQ is an
 89 FPGA + ARM embedded Linux
 90 system as shown in Fig. 4.1
 91 that was developed for the TAXI
 92 board supports 24 analog input
 93 channels in three blocks of eight
 94 channels each. A slightly modi-
 95 fied version of the board, IceTAXI,
 96 with one block of eight channels
 97 was produced for the IceTop scin-
 98 tillator array. Each channel is discriminated and the leading and trailing edges of the discriminator
 99 output are timestamped in a Spartan 6 FPGA with nanosecond precision. To achieve this, the output
 100 from the individual discriminators are interfaced with Serial-Input Parallel-Output (SIPO) Serial-
 101 izer Deserializer (SerDes) blocks in the FPGA with a 8:1 ratio at 950MHz. The subsequent 8-bit
 102 parallel output is then recorded at 118.75 MHz. In addition, input waveforms are recorded with a
 103 switched capacitor array and the integrated charge is determined online in the FPGA. The pulse
 104 time information and the charge-integrated or full waveform are then transferred to an ARM mi-
 105 crocontroller unit running Linux that handles the data formatting and transmission to the IceCube
 106 Laboratory via a 1 Gb fiber link under a White Rabbit layer.
 107

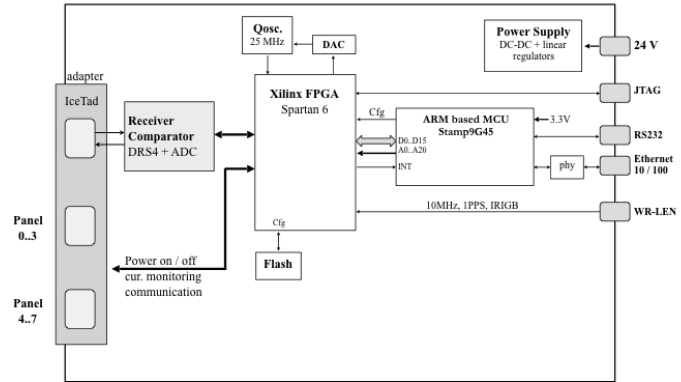


Figure 4: Layout of the IceTAXI Board.

4.2 μ DAQ

108
 109 The μ DAQ is a small microprocessor-
 110 based DAQ board (Fig. 4.2) ded-
 111 icated to a single sensor (SiPM
 112 connected to a scintillator panel)
 113 that includes power, timing and
 114 communications hub and spokes
 115 for medium remote connection
 116 (~ 60 m). The microprocessor,
 117 along with inexpensive logic, cap-
 118 tures sensor pulse start and stop
 119 with ~ 1 ns resolution. To achieve
 120 this, eight delayed inputs are used
 121 such that each input sees the same
 122 edge delayed by successive ~ 1 ns increments before being recorded into “counter capture” regis-
 123 ters that increment every 5.5 ns (180 MHz). Averaging multiple delayed inputs results in higher
 124 time resolution. The board also features amplifiers, with multiple gains for a wide dynamic range,
 125 after which the pulse is shaped for sample-and-hold ADCs from which charge is obtained versus
 126 time.

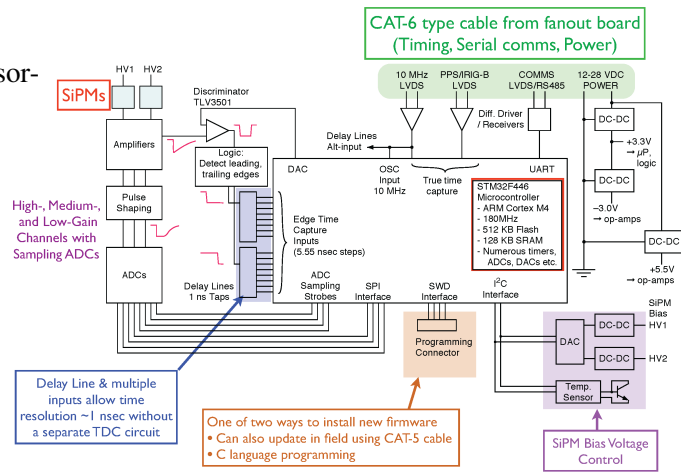


Figure 5: Layout of the μ DAQ Board

127 The μ DAQ design enables digitizing the signal at the output of the SiPM before transmission
 128 to the SFH. At the SFH, a Linux single-board computer (Beagle Bone Black) polls the seven panels,
 129 each with their own μ DAQ, and then forwards data to the IceCube Laboratory over optical fiber.

130 5. The Scintillator Field Hub subsystem

131 Communications, power, and timing for the scintillator array is accomplished via a network
 132 of Scintillator Field Hubs connected to backbone surface cabling to the IceCube Laboratory (ICL).
 133 Each SFH is the central DAQ node for a scintillator station (Fig. 2). The SFHs are synchronized
 134 to better than nanosecond precision by a White Rabbit (WR) Ethernet network [10], where the
 135 timing reference is a GPS receiver, and each SFH contains a WR node connected via single-mode
 136 optical fiber to a WR switch in the ICL. This link also provides gigabit Ethernet connectivity to
 137 each Scintillator Field Hub. The WR node in the SFH (WR-LEN⁴) provides timing and Ethernet
 138 connectivity to the DAQ via a copper Ethernet connection and two timing outputs: a reference 10
 139 MHz clock, and a 1-PPS IRIG-B timestring. A separate copper cable supplies the power to each
 140 SFH.

141 6. Prototype detector efficiency in a Muon Tower

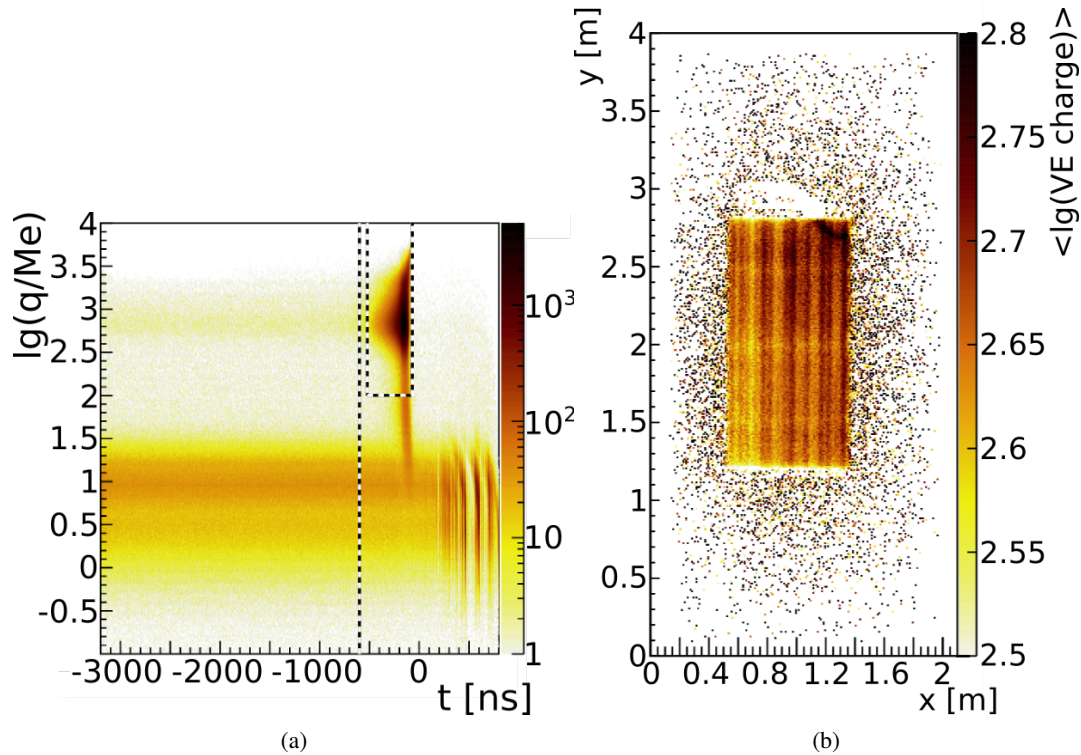


Figure 6: Left: Charge and time distribution of pulses detected with the prototype detector. The top region shows the high-charge band. The lower region the low-charge band and hence the SPE and the baseline. The dashed rectangle shows the quality cut for the MIPs. The distance between the high and low charge band shows the high light yield of a MIP compared to the base line. Right: Average pulse charge depending on the particle detection position. Single fibers are visible. Broken fibers or scintillators can be located and replaced. The higher average pulse charge located at $x=1.2$ m $y=2.8$ m arises because the fiber bundle coupled to the analog readout module, was for prototyping purposes just placed at the surface of the scintillator bars.

⁴<http://sevensols.com/index.php/products/wr-len/>

142 The Karlsruhe Institute of Technology (KIT) Muon Tower is a muon tracking detector with
143 limited streamer tubes (LST) originally from the KASCADE experiment and presently used for
144 calibration and efficiency measurements of scintillation detectors. The muon tower is capable of
145 tracking muons with an angular resolution of better than 1° and providing accurate position of
146 muons for the test detectors. This enables obtaining single photoelectrons (SPEs) and the amount
147 of SPEs per minimum ionizing particles (MIPs) in the test detector via a charge spectrum. Ad-
148 ditionally, muon tomography is also possible. Due to the LST, the Muon Tower has an in-plane
149 resolution of 1 cm^2 that allows for correction of the zenith angle when calculating the average
150 charge for vertical MIPs. It is also possible to investigate the efficiency and uniformity of the
151 inner detector system (scintillator bars, routing of optical fibers, optical connection). The charge
152 spectrum for through-going muons is shown in Fig. 6, left.

153 The plot in Fig. 6 (right) shows the average pulse charge depending on the particle position in
154 a logarithmic scale. Due to the optimal positioning of the fibers to the photosensitive surface of the
155 SiPM, the routing of the single fibers is visible. Due to this tomography-like feature of the muon
156 tower, broken scintillators or fibers can be located and replaced.

157 7. Summary & Outlook

158 We are currently developing a scintillator-based prototype detector as an upgrade to IceTop.
159 Each detector comprises 7 panels based on scintillator bars read out with wavelength shifting fibers
160 coupled to the photosensitive area of the SiPMs. We are investigating different options for fiber
161 diameter and fiber-to-sensor coupling.

162 Currently, two versions of DAQs are being explored; one featuring an embedded system ca-
163 pable of capturing full waveforms and the other comprising a small microprocessor with timing
164 and waveform capture with digital transmission of the data to the Beagle Bone Black based Field
165 Hub. White Rabbit provides timing and communications to the individual detectors. We anticipate
166 deploying a pair of prototype detectors in the 2017/18 Antarctic summer with an eventual phased
167 deployment of an array of up to 37 stations planned in the future.

168 References

- 169 [1] IceCube Collaboration, M. G. Aartsen et al., *J. Inst.* **12** (2017) P03012.
170 [2] IceCube Collaboration, R. Abbasi et al., *Nucl. Instr. Meth. A* **700** (2013) 188 – 220.
171 [3] IceCube Collaboration, M. .G. Aartsen et al., *POS (ICRC2015)* **628** (2015).
172 [4] K. Nitta et al., *Nucl. Instr. Meth. A* **535** (2004) 147.
173 [5] F. Retière et al. (T2K Collaboration), TIPP 2011 proceedings, *Phys. Proc.* **37** (2012) 1231 – 1240.
174 [6] MINERvA Collaboration, K. S. McFarland et al., *Nucl. Phys. Proc. Suppl.* **159** (2006) 107 .
175 [7] Pierre Auger Collaboration, A. Aab et al., arXiv:1604.03637 (2016).
176 [8] E. Dietz-Laursonn et al., *J. Inst.* **12** (2017) 4P04026.
177 [9] T. Karg, A. Haungs, M. Kleifges et al., arXiv:1410.4685 (2014).
178 [10] P.P.M. Jansweijer, H.Z. Peek, and E. de Wolf, *Nucl. Instr. Meth. A* **725** (2013) 187 – 190.

Overview and Performance of the Wavelength-shifting Optical Module (WOM)

The IceCube-Gen2 collaboration[†]

[†]http://icecube.wisc.edu/collaboration/authors/icrc17_gen2

E-mail: peter.peiffer@uni-mainz.de

The Wavelength-shifting Optical Module (WOM) is a novel photosensor concept developed in the context of the IceCube-Gen2 neutrino telescope, a next generation multi-km³ neutrino telescope at the South Pole. It provides a large photosensitive area with low detector noise and improved UV sensitivity. This is achieved by combining a wavelength-shifter (WLS) coated tube with two small, low-noise PMTs. Incident UV photons are absorbed by the WLS and re-emitted isotropically. A large fraction of the light is captured in the tube by total internal reflection and guided to the small PMTs. Through its cylindrical geometry, which is well matched to the drill holes, this concept results not only in an overall improved detection efficiency, but at the same time saves production and drilling cost. In this contribution we discuss the performance characteristics of the WOM and present the current status of the prototype development.

Corresponding authors: Peter Peiffer^{*1}, Dustin Hebecker²

¹*University of Mainz, Germany,*

²*DESY Zeuthen, Germany*

*35th International Cosmic Ray Conference - ICRC 2017
12.-20. July 2017
Bexco, Busan, South-Korea*

*Speaker.

1. Introduction

IceCube [1] is currently the world's largest neutrino detector, with an instrumented volume of 1 km^3 . Installation was completed in 2010 and the detector has been running successfully in its current configuration since 2011. IceCube-Gen2 is a planned extension to IceCube, both in high- and low-energy detection capabilities. It encompasses an increased instrumented volume for high energy neutrinos [2] and an increased instrumentation density in the core (PINGU) [3] combined with improved photo-sensors. The Wavelength-shifting Optical Module (WOM) is one of the sensors under consideration for IceCube-Gen2. It aims especially at increasing the total number of detected photons by shifting UV photons into the optical range. This makes the module sensitive in the UV range, where the Cherenkov spectrum peaks in the ice. This results in an increased effective photosensitive area compared to the upgraded Digital Optical Module (pDOM)¹ [4], another option for Gen2, see Fig. 1). At the same time, the WOM will have an order of magnitude lower noise than the currently used DOMs [1], which makes the WOM an ideal candidate for the low energy extension.

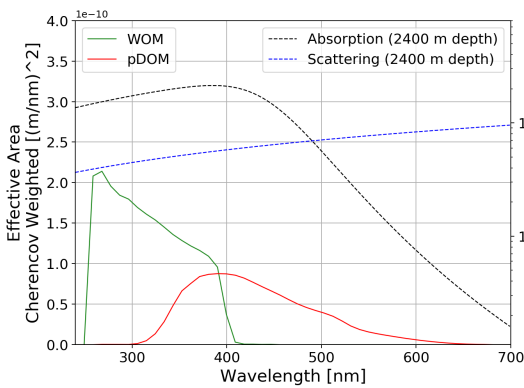


Figure 1: The wavelength-dependent absorption- and effective scattering length for photons in the ice (dashed lines) and the Cherenkov-weighted effective area of the pDOM (red line) and the estimated, Cherenkov-weighted effective area of the WOM for 50% detection efficiency (green line).

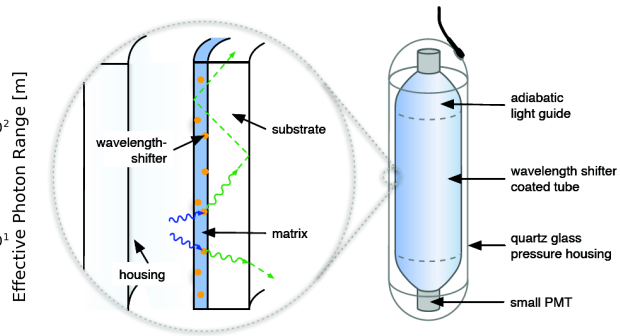


Figure 2: A schematic of the WOM: UV photons are absorbed in the WLS paint layer and are re-emitted as optical photons. If the incident angle of the emitted photons to the surface of the tube is smaller than the critical angle, they are trapped by total internal reflection and are guided along the tube to small, low-noise PMTs at the ends of the WOM tube.

The WOM, shown in Fig. 2, consists of a WLS-paint coated PMMA tube with an adiabatic light guide (ALG, [5]) at each end. These are connected to 3" PMTs and the entire assembly, including the read-out electronics, is housed in a quartz pressure vessel. UV photons are absorbed in the paint layer and are re-emitted as optical photons. This emission is isotropic and if the angle of the photon with respect to the tube surface is below the critical angle for total internal reflection, the photon is trapped and guided to the end of the tube: $\Theta_c = \arcsin \frac{n_{air}}{n_{PMMA}} \approx 41.8^\circ$ for $n_{PMMA} \approx 1.5$. The theoretical maximum trapping efficiency is 74.5%. At the end of the tube the light is concentrated by the ALG, which reduces the diameter of the tube while preserving the total cross section area. In theory, this allows a lossless concentration of the light. The paint is selected

¹in this paper, DOM refers to the modules mounted in IceCube and pDOM to the upgraded version for Gen2

for maximum overlap with the sensitivity of the PMT. The current prototype uses a Hamamatsu R12199-02 3" PMT, but other options are under investigation, including new super-bialkali PMTs. The advantages of this module are:

- **Higher number of detected photons:** The ice is transparent down to $\lambda=200$ nm and the number of Cherenkov photons follows a $1/\lambda^2$ distribution. The sensitive area is given by the tube surface A_0 , which exceeds the sensitive area of the pDOM and can even be scaled up by lengthening the tube, at the cost of deteriorating timing resolution (≈ 10 ns for a 1 m tube). The effective area (Fig.1) is given by $A_{eff} = A_0 \cdot N_{ph}(\lambda) \cdot \epsilon_{capt} \cdot \epsilon_{loss}$ with N_{ph} the integrated available spectrum, ϵ_{capt} the capture efficiency and ϵ_{loss} the loss factor due to attenuation.
- **Lower noise:** PMT noise scales with the photo-cathode area. The PMTs currently used in the WOM prototype have a dark noise of ≈ 30 Hz with a single-photoelectron-threshold at ice temperatures ($-10^\circ\text{C} - -40^\circ\text{C}$), compared to ≈ 500 Hz for the DOM-PMT.
- **Lower energy threshold:** the energy threshold of a Cherenkov detector is proportional to the effective sensitive area per unit volume and is limited by dark noise. Since the noise of the WOM is an order of magnitude lower and the effective sensitive area is larger than that of the (p)DOM, this module will allow the detection of lower energy events compared to IceCube with the same density of modules.
- **Lower drilling cost:** the cylindrical shape of the WOM matches the hole geometry better and has a much smaller diameter than the pDOM. This allows for smaller holes and saves on drilling time, energy and cost.

2. Prototype development

2.1 Materials

The WOM consists of the pressure vessel, the WLS coated tube plus light guides, the WLS paint and the PMTs. The pressure vessel has to be UV transparent and pressure resistant up to 700 bar. A commercial quartz tube with hemispherical end caps that fulfills these requirements has been selected. For the material of the WLS tube refractive index, compatibility with different WLS coatings and price were considered. In the end PMMA was chosen. The WLS needs to have a broad absorption spectrum in the UV range and minimal overlap between absorption and emission, so that it is transparent to its own emitted light. The WLS optimization has been described in [5]. Fig.3 shows the relative absorption and emission spectrum of the current WLS. However, research into other WLS paints is ongoing.

2.2 Adiabatic light guide

The development of the adiabatic light guide (ALG) has been reported in [5]. Different methods of attaching the ALG to the WOM tube have been investigated ranging from various glues to solvent welding. Fig.4 shows the result of using UV curing glue. By visual inspection, most of the light reaches the ends of the ALGs. However, the gluing lines are visible due to scattered light, signifying a small light loss there. Investigations are ongoing, whether the connection can be improved by solvent welding or a monolithic production of a WOM-tube with adiabatic ends.

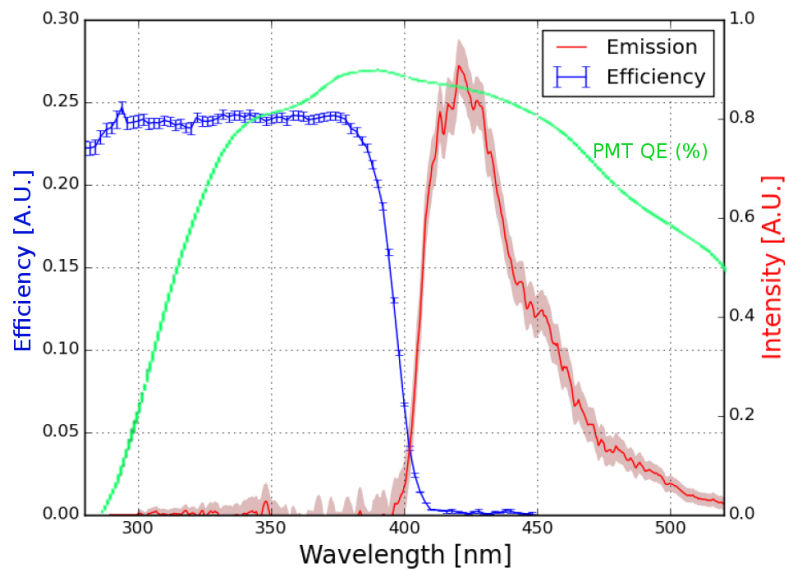


Figure 3: The relative shifting-efficiency and emission spectra of the WLS paint currently used in the WOM.

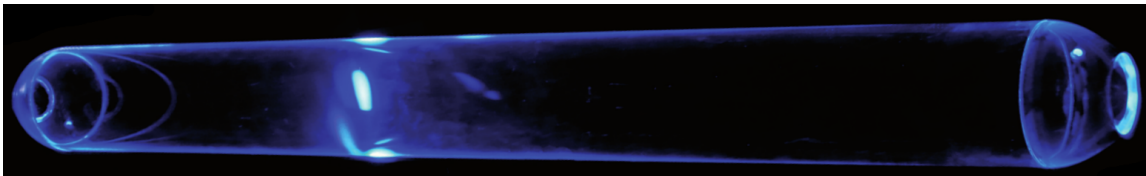


Figure 4: A WOM tube under UV light with two adiabatic light guides glued to it using UV-curing glue.

2.3 Mounting

To mount the WLS tube and the PMTs inside the pressure vessel, a holding structure has been developed. The end of the ALG is machined to match the curvature of the PMT, to which it is optically connected with a thin layer of optical gel. Around the ALG and the PMT is an aluminum jacket glued to the end of the WLS tube. Springs are attached to the jacket and to the base of the PMT, pulling the PMT against the ALG. In this way constant optical contact is ensured even during thermal contraction. The entire tube + ALG + PMT construction is inserted into the pressure vessel, which is closed with a hemispherical end cap, containing the feed-through for signal and power. The cable to the lower PMT is threaded through a small hole in the ALG and runs inside the WLS tube, so that both PMTs can be supplied through one feed-through without shadowing from the cable. Fig. 5 shows a schematic drawing of the holding structure and photos of the assembled WOM prototype.

2.4 PMT and noise

Currently, the WOM uses the same PMT type that is also used in KM3NeT [6] (Hamamatsu R12199-02) with a passive base. In this configuration the dark noise of the PMTs has been measured to range from (22 ± 5) Hz at -10°C to (31 ± 6) Hz at -50°C , more than an order of magnitude

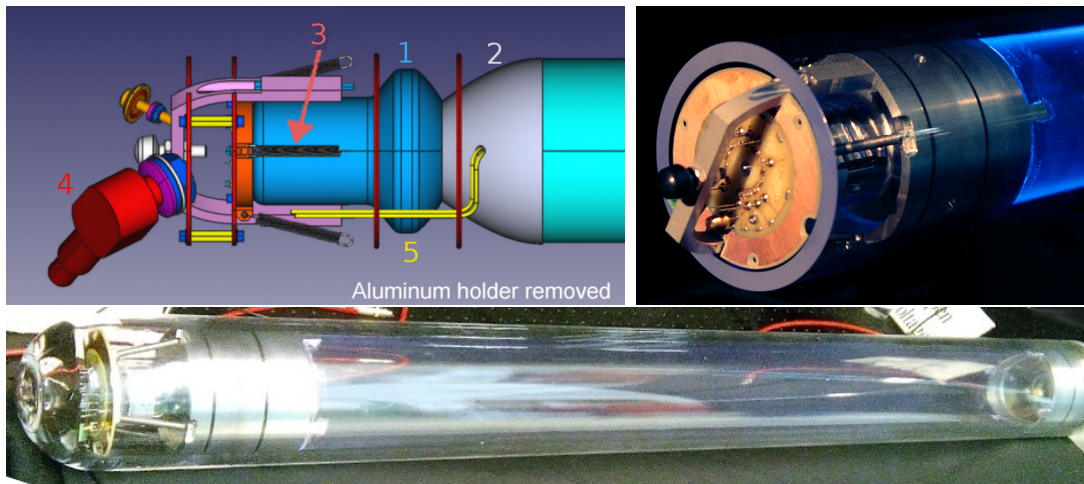


Figure 5: Upper left: A drawing of the holding structure. 1=PMT, 2=ALG, 3=springs, 4=pressure-vessel feed-through, 5=internal connecting cable (aluminum jacket not shown). Upper right: complete holding structure inside the quartz tube without end-cap. Bottom: an assembled prototype.

lower than the ≈ 500 Hz of the DOM. Research into improved PMTs and the radiogenic noise contributions of the quartz vessel, the WLS tube and the ALG is ongoing.

3. WOM testing setup

To fully characterize the WOM, we have constructed an optical setup, that will allow 2D scans of the entire tube surface. It is used to check the coating uniformity and investigate the light propagation inside the tubes. Fig. 6 shows a schematic of the setup, consisting of a Xenon lamp with a monochromator and a beam splitter using of fused silica optics for optimal UV transparency. The light beam is interrupted by a chopper wheel connected to a lock-in amplifier setup for noise suppression. A major source of PMT noise is the activation of the photo-cathode due to ambient light when exchanging a tube. This noise takes hours to subside, but with this setup it can be suppressed to a level, where measurements can be taken without any dead-time after re-mounting a tube. The photo-diode (PD) is used as reference, while a part of the light is guided to the WOM tube by the liquid light guide (LLG). Its end is mounted on an orbital wheel around the tube, so the tube can be illuminated from any angle. The orbital wheel is mounted on a linear stage, which can be driven along the entire length of the tube. At both ends the shifted light trapped in the tube is read out by calibrated PMTs. The tube is optically coupled to the PMTs using special optical gel pads, to ensure re-mounting stability. The distance between the PMTs can be altered to allow for different tube lengths with or without adiabatic light guides.

Automated scans with arbitrary step sizes in position, rotation and wavelength can be made. For each illumination spot the efficiency of the photon detection is measured, which takes about 4 sec per spot, including sled motion. The efficiency is the convolution of the shifting efficiency ϵ_{WLS} of the WLS (close to one), the trapping ratio ϵ_{TR} (close to 0.75), the light guiding efficiency ϵ_{LG} (unknown, depends on absorption and scattering in the tube) and the efficiency of the PMTs ϵ_{PMT} (collection- and quantum efficiency. Known, depends on λ). It is defined as:

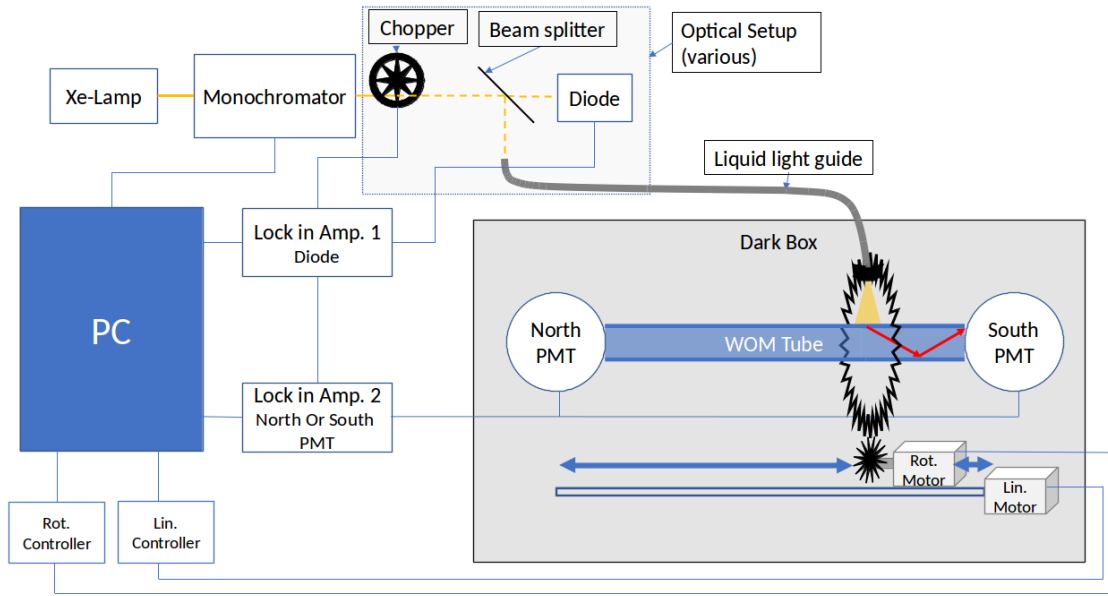


Figure 6: A schematic drawing of the tube scanner, using fused silica optics and a liquid light guide.

$$\epsilon_{tot}(\lambda_{in}) = \epsilon_{WLS} \cdot \epsilon_{TR}(\lambda_{out}) \cdot \epsilon_{LG} \int \epsilon_{PMT}(\lambda_{out}) = \frac{\# \text{ of detected photons}}{\# \text{ of injected photons}}$$

The number of injected photons is known from the calibrated reference PD and the fixed branching ratio between the reference beam and the light intensity at the exit of the fiber. The number of detected photons is calculated from the PMT signal, its known spectral sensitivity function and the emission spectrum of the WLS. With the photo-diode correction the system is linear over the full wavelength-range of the Xenon lamp and stable in time. Fig. 7 shows a 2D scan of the PMT signal current over illumination position. Close to the PMT the light yield is maximal. It drops off over the length of the tube due to attenuation.

4. Simulation

A simulation of the WOM has been integrated into the IceCube software framework, so that the in-ice performance can be simulated for different detector configurations. Muons in the energy range of 3 TeV to 1 PeV are injected into the ice volume. The resulting Cherenkov light emission is calculated and propagated through the ice. Photons intersecting the OM surface are stored for later processing, which uses the WOM properties. In the first step the angular acceptance, derived from Fresnel equations and Snell's law, with a refractive index of $n_{ice} = 1.33$, $n_{glass} = 1.50$ and $n_{air} = 1.00$, is applied, followed by the measured wavelength acceptance of the WLS tube. This includes the efficiency of the WLS and the propagation efficiency which together give about 50% between $\lambda = 250 - 400$ nm. This is combined with the PMT acceptance convoluted with the emission spectrum. Since the probability of losing a photon that propagates in the tube is lower when it hits close to one of the PMT, a position dependent correction function was introduced based on previous measurements. In a first simulation we look at the total number of photons detected as

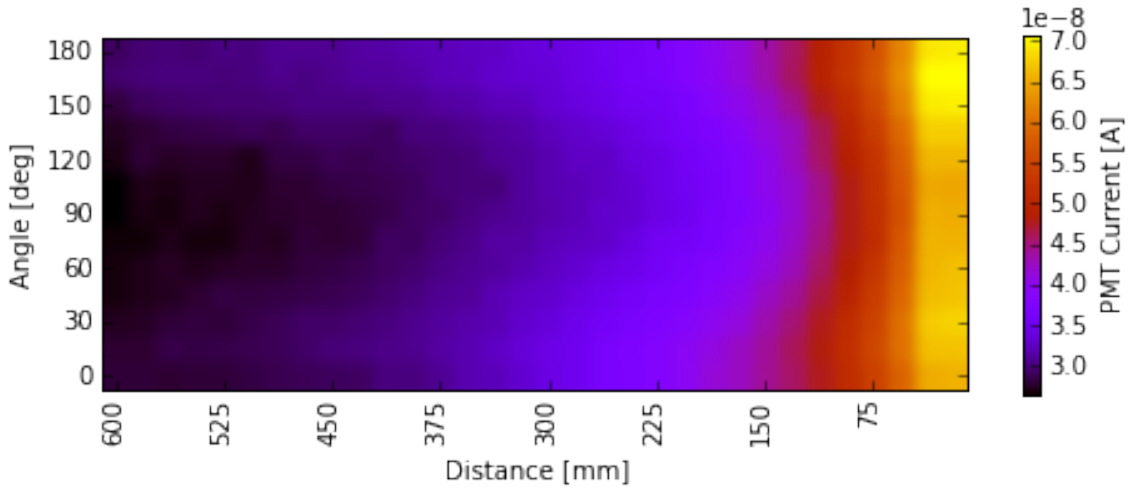


Figure 7: 2D scan of the local efficiency of the WLS tube. Shown is the PMT signal current over longitudinal position in mm and rotational position in degree for an incident wavelength of $\lambda=375$ nm. The PMT is located to the right. The variation over a rotation at fixed distance is $\leq 10\%$

a function of energy and distance from the muon track. We simulate $2 \cdot 10^5$ events with an energy power-law index of -1.4 in the so called sunflower 240 detector geometry² [2]. For comparison the pDOM, an upgraded version of the IceCube-DOM is used with an identical geometry and event set. Fig. 8 shows the number of photons detected per muon event, plotted against the event’s energy. Over the whole range the WOM detects a factor of 1.7 ± 0.1 more photons than the pDOM.

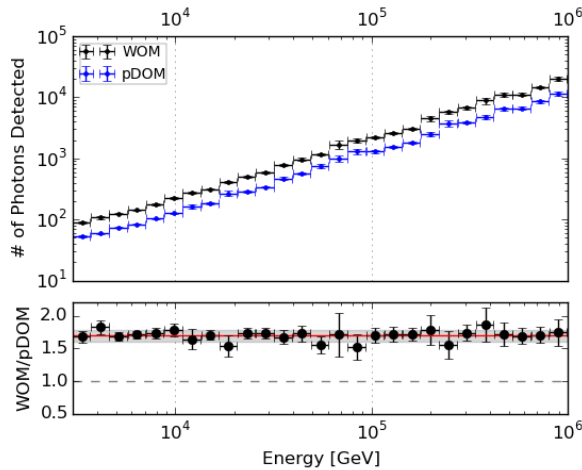


Figure 8: Comparison of the number of photons detected as a function of energy for the WOM and the pDOM in the sunflower 240 geometry. It can be seen, that the WOM detects a factor of 1.7 ± 0.1 more photons than the pDOM for all energies.

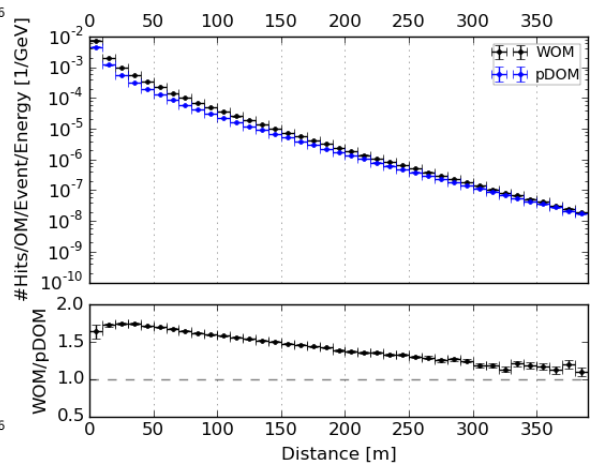


Figure 9: Comparison of the number of photons per energy detected as a function of the closest distance to the muon track for the WOM and the pDOM in the sunflower 240 geometry. The WOM detects more photons than the pDOM for all relevant distances.

²Other geometries perform similar for the parameters shown.

In Fig. 9 the distance between muon track and the individual OMs is investigated. The photon number is plotted per energy, per event and OM against this distance. The WOM performance decreases as a function of distance due to shorter attenuation-length for the UV photons in the ice, but stays better than that of the pDOM for all relevant distances. The plateau at very short distances (i.e. for unscattered photons) is caused by the different angular acceptance of the modules.

Detailed measurements of the WOM time response are ongoing and will be implemented in the simulation for a realistic arrival time modeling. Additionally the use of a super-bialkali version of the PMT might increase the efficiency by up to 45%. Any efficiency values for new WLS paints that are studied can also be directly included in the simulation framework.

5. Summary and Outlook

The WOM has proven to be a very promising low noise, high efficiency and low cost optical module, but further improvements of several components and simulations are ongoing. A reliable mounting structure has been developed and a prototype has been assembled. The WLS developed for the WOM shifts light from the $\lambda \approx 250\text{-}400$ nm to $\lambda > 400$ nm. Measurements of the light capture and transport efficiency showed values up to 50% [8]. However, the efficiency strongly depends on coating quality and uniformity. Further studies into the optimization of the WLS coating are ongoing and a dedicated semi-automated measuring setup has been built to quantify any future coatings. The adiabatic light guides developed for the WOM have been successfully coupled to the WOM tube with an UV-curing glue, but further optimization of the gluing process are ongoing to minimize the light loss. The quartz vessel has been pressure tested and has been proven to be vacuum tight for more than a year. In simulations the WOM has been shown to detect more photons than the pDOM for all energies, types of events and detector geometries for IceCube-Gen2. Beyond IceCube-Gen2, its high efficiency and low noise make this optical module the ideal candidate for the conceptualized MICA supernova detector [9]. The performance of the WOM can be improved even further by using new PMTs with a higher quantum efficiency or newly developed WLS. The WOM was developed for the IceCube-Gen2 experiment. However, it can be conceptually adapted to other experiments that profit from its UV detection capabilities, such as SHiP. [7]

References

- [1] **IceCube** Collaboration, M.G. Aartsen et al., *JINST* **12** (2017) P03012;
- [2] **IceCube-Gen2** Collaboration, arXiv:1412.5106v2 [astro-ph.HE]
- [3] **IceCube-Gen2** Collaboration, *J. Phys. G* **44** (2017) 054006
- [4] **IceCube PINGU** Collaboration, P. Sandstrom et al., *AIP Conf. Proc.* **1630** (2014) 180–183.
- [5] **IceCube** Collaboration, *POS (ICRC2015)* **1134**, 2016
- [6] **KM3NeT** Collaboration, *Letter of Intent for KM3NeT 2.0*, arXiv:1601.07459v2 [astro-ph.IM]
- [7] **SHiP** Collaboration, arXiv:1504.04956, April 2015
- [8] **IceCube-Gen2** Collaboration, D. Hebecker *et al.* *EPJ Web of Conferences* **116**, 01006 (2016)
- [9] Sebastian Böser et al., *Astropart. Phys.* **62**, March 2015, Pages 54–65

The Precision Optical CALibration Module for IceCube-Gen2: First Prototype

The IceCube-Gen2 Collaboration[†]

[†] http://icecube.wisc.edu/collaboration/authors/icrc17_gen2

E-mail: kai.krings@tum.de, elisa.resconi@tum.de,
rongen@physik.rwth-aachen.de

IceCube-Gen2 is under design, including a Phase-1 extension dedicated to the precision study of atmospheric neutrinos and to an improved search for neutrino astrophysical sources. A new level of precision is needed in order to achieve improved performance with respect to IceCube. A complementary calibration system with respect to the one presently installed in IceCube will enable a better understanding of the ice and will therefore significantly reduce systematic effects. We present a novel specialized calibration device named as the Precision Optical Calibration Module (POCAM). The design of the POCAM is based on the principle of an inverted integrating sphere. An appropriately placed matrix of LEDs in combination with a diffusing layer on the inside of the sphere results in a nearly homogeneous light emission. The output of the LEDs is monitored *in-situ* to high precision by photosensors, ensuring control over the light output. A first complete prototype has been recently developed and deployed within the cubic kilometer scale Gigaton Volume Detector (Baikal-GVD).

Corresponding authors: Kai Krings^{*1}, Elisa Resconi¹, Martin Rongen²

¹ *Technische Universität München, Physik-Department, James-Frank-Str. 1, D-85748 Garching bei München, Germany*

¹ *RWTH Aachen University, III. Physikalisches Institut, Otto-Blumenthal-Str., D-52074 Aachen, Germany*

*35th International Cosmic Ray Conference — ICRC2017
10–20 July, 2017
Bexco, Busan, Korea*

*Speaker.

1. The Precision Optical Calibration Module

The Precision Optical CALibration Module (POCAM) is a novel specialized device dedicated to *in-situ* calibration of the IceCube-Gen2 detector. The goal is to address the primary experimental systematic uncertainties caused by a partial understanding of the optical properties of the ice [1] and the efficiency and angular acceptance of the IceCube Digital Optical Modules (DOMs) [2].

Presently, the systematic uncertainty in IceCube coming from the ice properties is at the level of 10%, being the dominant systematic for a number of analysis. The goal of the POCAM is to reduce these uncertainties down to a level of few %. Moreover, the POCAM will be a complementary calibration device with respect to other calibration devices, most notably the LEDs already present in the IceCube DOMs.

The POCAM is based on an isotropic, multi-wavelength, and pulsed light source [3, 4]. The POCAM design is shown in Fig. 1. It consists of two glass hemispheres connected by a cylindrical pressure and temperature-resistant titanium (or alternatively stainless steel) housing. Light from a multi-wavelength array of LEDs is driven by a Kapustinsky-style circuit [5] to obtain light pulses of ~ 10 ns and $10^8 - 10^{10}$ photons. The pulses are diffused by a sphere in each hemisphere to generate an isotropic and homogeneous ice illumination. The goal is for the light from the hemispheres to be isotropic to within 2% and the total light output to be determined to within 2% by *in-situ* photosensors.

A first complete prototype has recently been deployed within the Gigaton Volume Detector (Baikal-GVD), which is under construction in Lake Baikal (Siberia) [6].

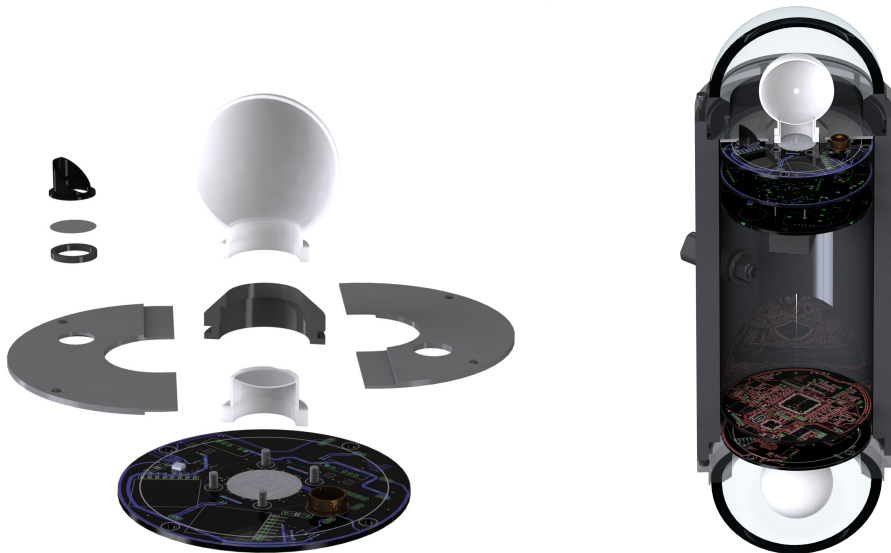


Figure 1: POCAM principle components (left) and complete assembly (right). The POCAM is composed of four sub-systems: the pressure housing, the digital, the analog circuit boards, and the light diffuser elements. Each element is described in more detail in the text.

2. The first POCAM prototype

The POCAM is composed of four sub-systems: the pressure housing, the digital and the analog circuit boards, and the light diffuser elements.

The pressure housing consists of a 15 mm thick titanium cylinder, the two open sides of which are each closed by a flange and a glass hemisphere attached to it. The glass hemispheres made of BK7 glass have a thickness of 7 mm and a diameter of 4.5 inches. The entire housing was manufactured by the Nautilus Marine Service GmbH and specified to a pressure resistance of at least 1500 bar. This corresponds to a 15 km water column and thus the approximately 10-fold pressure at the destinations in Antarctica and in Lake Baikal. In fact, larger pressures may arise during the re-freezing process in the Antarctic ice.

An analogue and a digital circuit board are installed within the pressure housing and secured to the titanium flange. They form a fully functional unit that can communicate, emit and register light. Two of these self-sufficient units are installed within the POCAM sharing a common voltage supply board.

A micro-controller, an FPGA, memory chips, an ADC (analog-to-digital converter) and an FPGA-based LED controller are located on each digital board. The micro-controller is responsible for communication and management of the data to be stored on the memory chips. The FPGA takes over all timing sensitive tasks. This includes control signals for the analog board, reading and buffering of the ADC data and controlling the two separate FPGA LED drivers. The two channel ADC is needed to digitize the signals from the two light sensors. The analog board consists of a light emitting and a light measuring part. The part responsible for the light measurement consists of two different light sensors which are read out via the ADC with the aid of two Cremat charge-sensitive rectifiers¹. Two photosensors are installed in each hemisphere to monitor the emitted light pulse. The one presently installed are a 9 mm² SiPM (PM3325-EB) from KETEK and a 33 mm² PIN-Diode from First Light Sensor (PS33-6b-TO). The PIN-Diode has blue-green enhanced efficiency. The PM3325-EB is optimized for blue light and has a low dark count rate and low cross talk probability. To avoid saturation of the SiPM a special filter foil is added. Furthermore, there are additional sensors for environmental monitoring (e.g. temperature, pressure and humidity) on all boards. The light emitting part consists of four Kapustinskis LED drivers with two different pulse configurations (5-10 ns, 15-25 ns) and two colors (blue 455-470 nm, green 525-527 nm) as well as two additional FPGA driven LEDs with longer pulse durations (20 - 80 ns) and higher intensities for a total of three blue and three green LEDs.

Crucial parts of the POCAM are the two diffusing spheres installed on top of the LED arrays. Their task is to convert the strongly anisotropic light from the LEDs into an isotropic diffuse emission profile. For this purpose a CNC-milled hollow PTFE sphere with a wall thickness of 1 mm and a diameter of 50 mm has been designed and developed at TU Munich. The LEDs are coupled to the sphere via a PTFE “plug” of 0.5 mm thickness. A first isotropy measurement is shown in Fig. 2.

¹CR-110, CR-113 and operational amplifiers (T.I. LM6171A)

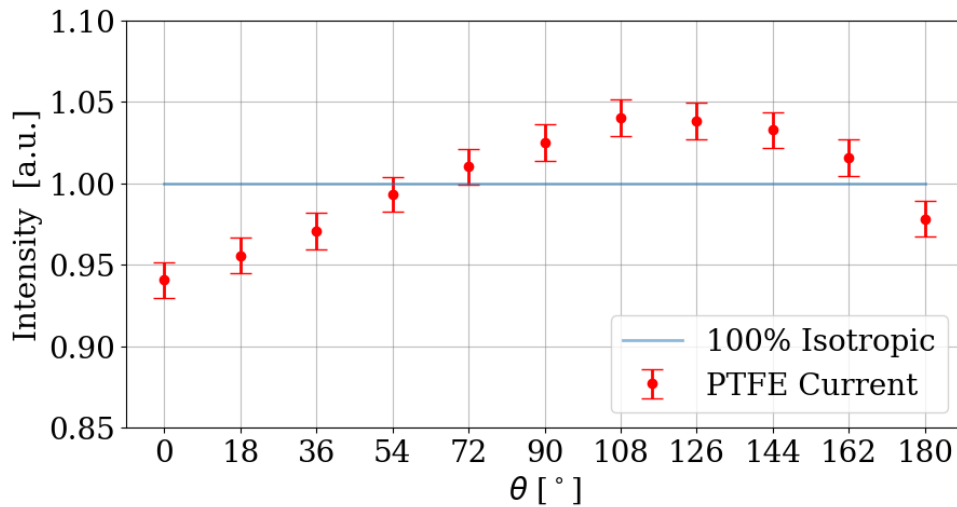


Figure 2: POCAM integrating sphere isotropy measurements. Shown is the angular spectrum with $\theta = 90^\circ$ being the vertical top of the sphere; the intensity is plotted such that the mean of each measurement corresponds to an intensity of 1.0. It is worth noting that the shift in symmetry towards 108° is most likely caused by minor alignment and centering difficulties within the measurement setup. Further possibilities, to improve the isotropy and its measurement, are currently being investigated.

The isotropy measurement itself is carried out with a mechanical two-axis rotation device to measure the field of view intensity for various angles; for now this is limited to the polar angle. The SiPM, used as the light sensor is the same that is mounted on the POCAM PCB. However, with its high sensitivity, the components have to be perfectly aligned to result in a symmetric spectrum. An improved and more precise measurement setup is being realized reducing some systematic uncertainties still present in our current measurement setup.

3. Test Deployment in Baikal-GVD and First Light

In order to validate the POCAM under realistic conditions, a collaboration with Baikal-GVD has been established [7][8]. In winter 2016-2017, the first POCAM prototype was completed and shipped to Siberia. After a few days of laboratory integration and functional testing, the POCAM has been integrated within GVD on one of the outer strings at depth of 1.100 m. Data analysis of the POCAM-GVD is on-going and will be reported elsewhere.

Early May 2017, detector time in GVD was reserved for POCAM tests and several flasher runs have been carried out. A series of flasher runs have been done at various light intensities: for 100.000 flashes at 53 Hz the GVD detector response (i.e. the live detector rate) increased from the usual background of 48-49 Hz to around 100 Hz. Fig. 4 shows exemplary data of *in-situ* SiPM signals. The analysis of the POCAM-GVD data is on-going and will be reported in the future.



Figure 3: The POCAM module mounted to the GVD string before deployment in the Baikal lake.

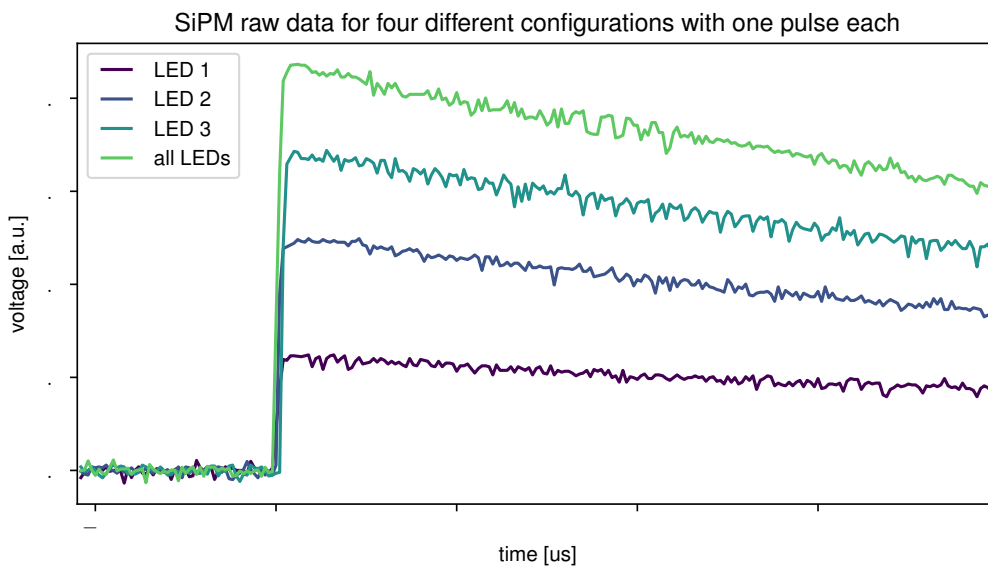


Figure 4: SiPM raw data obtained from POCAM flashes within GVD. LED 1 is the blue, short pulse Kapustinsky, LED 2 is the blue long pulse Kapustinsky, LED 3 is the blue FPGA LED at 40 ns pulse length; all LEDs is the simultaneous flash of a 10 ns blue FPGA pulse together with 1 and 2.

4. Anticipated measurements in IceCube-Gen2

While the POCAM will be a general purpose calibration instrument for IceCube, its isotropic light emissions pattern has clear advantages over the currently used LEDs for a number of specific measurements, which are summarized in the following.

The glacial Antarctic ice shows an anisotropic scattering amplitude [9], which appears to be aligned with the ice flow direction. With an isotropic light source the systematic uncertainty of the measurement of this effect can be improved as no initial light-emission pattern needs to be assumed. With respect to the detector characteristics the isotropic light pattern enables a direct measurement of the individual relative DOM efficiencies. While the average detection efficiency of all DOMs is well constrained, individual DOMs may deviate from this value by roughly 10% due to fluctuations in the PMT quantum efficiencies and local ice effects. Currently this measurement is done using cosmic ray induced muon events. It is limited by systematic uncertainties of the selection efficiency of single minimum-ionizing muons.

The POCAM can mimic the light signature of high energy cascades through its calibrated light output. This allows to test the reconstructed cascade energy scale to the uncertainty at which one knows the total POCAM photon output. In addition, by precisely timing the light flashes, closely separated cascades can be mimicked and the cascade vertex separation power, as required for the identification of tau neutrino interactions, can be tested.

A unique possibility measuring the optical properties of the refrozen drill holes will be outlined in more detail in the following.

After the propagation of Cherenkov photons through the bulk glacial ice, each photon detected by a DOM has to also propagate through the refrozen water of the drill holes, called "hole ice". The optical properties of the hole ice are less well understood compared to the bulk glacial ice and are one of the largest uncertainties to neutrino oscillation measurements in IceCube [10]. The hole ice was directly imaged by a camera installed at the bottom of a drill hole. A clear outer region and a central column of ~ 8 cm diameter with a very small scattering length (see Fig. 5a) are seen.

The impact of the hole ice is currently being modeled as a modification to the DOMs angular acceptance curve (see Fig. 5b). Here the size of the column determines the relative acceptance in the very forward region ($\cos(\theta) = 1$), while the scattering length modifies the shape around the maximum. Measurements are difficult as the forward region can not be directly probed with the installed LEDs or with Cherenkov light from atmospheric muons. Different measurements and models are currently being used and their range reflects the current uncertainty with respect to the angular acceptance.

To investigate the possibility to improve the *in-situ* angular acceptance curve measurement using the POCAM, a photon tracking simulation using standard IceCube tools has been performed. A single POCAM is simulated as a point-like and perfectly isotropic emitter situated in the center of the IceCube infill array, DeepCore [11]. Due to expected improvements in the drilling technology, it is assumed that the hole ice surrounding the POCAM has the same properties as the bulk ice, unlike the older IceCube holes. As an initial simplification the bulk glacial ice is assumed to be free of scattering. The same study can be performed in realistic bulk ice, by applying stringent timing cuts on the photon propagation delay from the POCAM to each receiving DOM, ensuring a straight, unscattered propagation. The light emitted from the POCAM can be detected by any IceCube DOM.

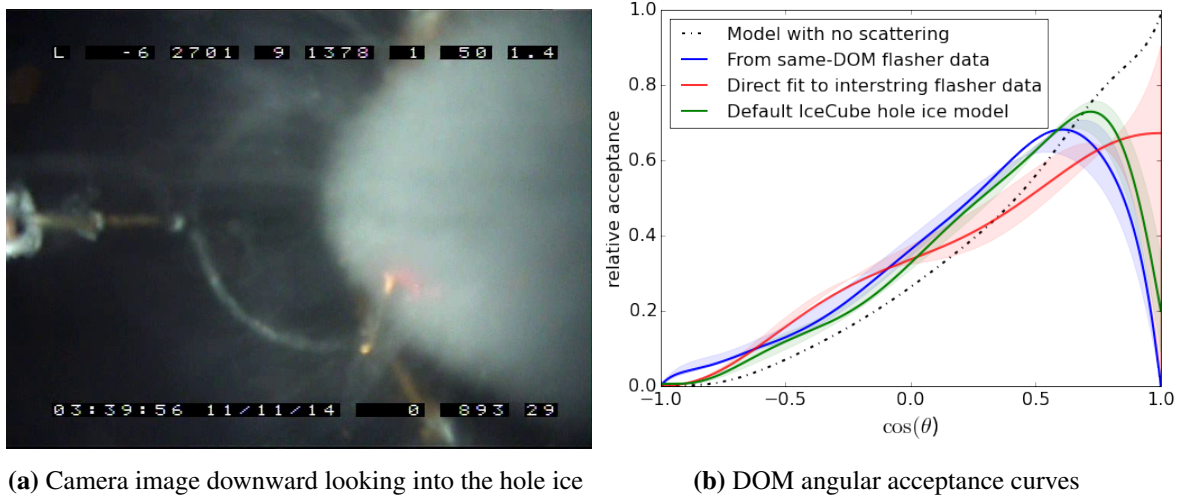


Figure 5: Current understanding of the impact of the refrozen ice within the drilled holes on the DOM's angular acceptance.

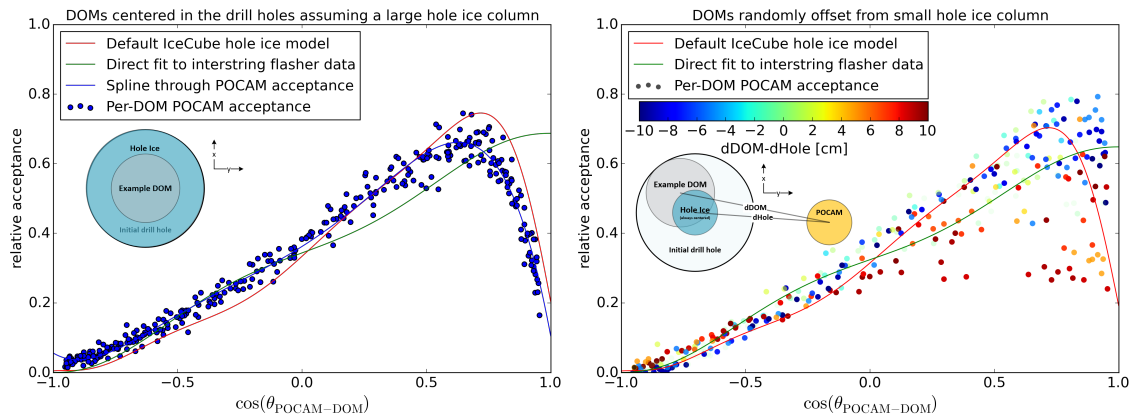
Two kinds of datasets have been simulated. The reference dataset accounts for bulk ice propagation but no propagation through the hole ice and assumes the DOMs to be able to measure photons over their entire spherical surface. All other datasets assume a given realization of the hole ice and only allow photon detection at the PMT surface, representing the data from a potential measurement.

The DOM-wise ratio of detected photons in the data-like set and the reference dataset is equivalent to the DOMs *in-situ* angular acceptance function at the zenith angle of this DOM relative to the POCAM. By plotting the relative acceptance of many DOMs the overall angular acceptance of an average DOM is obtained. Figure 6a shows an example where the entire drill hole is assumed to be filled with a weakly scattering medium and all DOMs are located in the center of their respective hole. The obtained angular acceptance curve agrees well with the "Default IceCube hole ice model" which is based on the same assumptions. Figure 6b shows an example for a small, but strongly scattering central hole ice column. In addition the DOMs are now randomly positioned inside the drill hole. Obviously no consistent average angular acceptance curve can be obtained, as different parts of the DOM surface are being shaded off relative to the emitter. Using Monte Carlo knowledge about the geometry, we can identify causally connected curves which belong to similar relative geometries. In the experiment the geometric ambiguity can be resolved by a multitude of POCAMs illuminating each DOM from different azimuthal angles.

Given a satisfactory measurement in Gen2 Phase-1, the individual angular acceptance curves can also be interpreted in terms of the underlying parameters (size and scattering length of the hole ice and position of the DOM). This allows to treat the hole ice via direct photon propagation instead of the effective description via the angular acceptance curve, which neglects azimuthal effects.

5. Summary and Outlook

We have presented the concept and design of an isotropic, multi-wavelength and pulsed light source



(a) Assuming the entire drill hole to be filled with a weakly scattering medium and the DOMs to be centered inside the holes (IceCube default)

(b) Assuming a central, small and strongly scattering column with the DOMs randomly positioned inside the holes

Figure 6: POCAM capability for measuring the IceCube drill hole properties. The points represent different DOMs measuring light from a single POCAM at different angles.

to be used as a calibration device in IceCube-Gen2. In the baseline plan for IceCube-Gen2 Phase-1, two POCAM modules on each string will enable us to determine *in situ* the relative optical efficiency and hole ice properties of the nearby DOMs. In addition the POCAMs will be used to re-evaluate bulk ice properties within the Gen2 Phase-1 volume, which can also be applied to the rest of the detector. The deployment of the first POCAM prototype in Baikal-GVD during 2017 permits the validation of the POCAM concept within a neutrino telescope and in the same time provides valuable information for GVD.

Acknowledgments

We thank the Baikal collaboration for allowing the deployment of the POCAM prototype in GVD.

References

- [1] **IceCube** Collaboration, M. G. Aartsen et al., *Nucl. Instrum. Meth.* **A711** (2013) 73–89.
- [2] **IceCube** Collaboration, M. G. Aartsen et al., *EPJ Web of Conferences* **116** (2016) 06011.
- [3] **IceCube-Gen2** Collaboration, K. Krings, *Pos (ICRC2015)* 1133 (2016).
- [4] **IceCube Gen2** Collaboration, M. Jurkovic et al., *EPJ Web of Conferences* **116** (2016) 06001.
- [5] J. Kapustinsky et al., *Nucl. Instr. Meth. Phys. Res. Sec.A* **241** (1985) 612 – 613.
- [6] A. D. Avrorin et al., *Pos (EPS-HEP2015)* 418 (2015).
- [7] I. Belolaptikov et al., *International Cosmic Ray Conference* **1** (1995) 1043.
- [8] V. A. Balkanov et al., *Appl. Opt.* **33** (1999) 6818.
- [9] **IceCube** Collaboration, D. Chirkin, [arXiv:1309.7010](https://arxiv.org/abs/1309.7010).
- [10] **IceCube Collaboration** Collaboration, M. G. Aartsen et al., *Phys. Rev. D* **91** (Apr, 2015) 072004.
- [11] **IceCube** Collaboration, R. Abbasi et al., *Astropart. Phys.* **35** (2012) 615–624.